The Population of Small Near-Earth Objects: Composition, Source Regions, and Rotational Properties

Juan A. Sanchez[1,7] ⓘ, Vishnu Reddy[2,7] ⓘ, Audrey Thirouin[3] ⓘ, William F. Bottke[4] ⓘ, Theodore Kareta[3,7] ⓘ, Mario De Florio[5] ⓘ,
Benjamin N. L. Sharkey[6,7] ⓘ, Adam Battle[2,7] ⓘ, David C. Cantillo[2,7] ⓘ, and Neil Pearson[1] ⓘ

[1] Planetary Science Institute, 1700 East Fort Lowell Road, Tucson, AZ 85719, USA; jsanchez@psi.edu
[2] Lunar and Planetary Laboratory, University of Arizona, 1629 East University Boulevard, Tucson, AZ 85721-0092, USA
[3] Lowell Observatory, 1400 West Mars Hill Road, Flagstaff, AZ 86004, USA
[4] Department of Space Studies, Southwest Research Institute, 1050 Walnut Street, Suite 300, Boulder, CO 80302, USA
[5] Division of Applied Mathematics, Brown University, 170 Hope Street, Providence, RI 02906, USA
[6] Department of Astronomy, University of Maryland, 4296 Stadium Drive PSC (Building 415), Room 1113, College Park, MD 20742-2421, USA

Abstract

The study of small (<300 m) near-Earth objects (NEOs) is important because they are more closely related than larger objects to the precursors of meteorites that fall on Earth. Collisions of these bodies with Earth are also more frequent. Although such collisions cannot produce massive extinction events, they can still produce significant local damage. Here we present the results of a photometric and spectroscopic survey of small NEOs that include near-infrared spectra of 84 objects with a mean diameter of 126 m and photometric data of 59 objects with a mean diameter of 87 m. We found that S-complex asteroids are the most abundant among the NEOs, comprising ∼66% of the sample. Most asteroids in the S-complex were found to have compositions consistent with LL-chondrites. Our study revealed the existence of NEOs with spectral characteristics similar to those in the S-complex but that could be hidden within the C- or X-complex due to their weak absorption bands. We suggest that the presence of metal or shock darkening could be responsible for the attenuation of the absorption bands. These objects have been grouped into a new subclass within the S-complex called Sx-types. The dynamical modeling showed that 83% of the NEOs escaped from the ν_6 resonance, 16% from the 3:1, and just 1% from the 5:2 resonance. Lightcurves and rotational periods were derived from the photometric data. No clear trend between the axis ratio and the absolute magnitude or rotational period of the NEOs was found.

Unified Astronomy Thesaurus concepts: Asteroids (72); Near-Earth objects (1092); Spectroscopy (1558); Photometry (1234)

1. Introduction

The population of small near-Earth objects (NEOs) constitutes the main reservoir of meteorites that fall on Earth. Because of this, their study is important to understanding how and where they formed, as well as identifying the regions in the solar system that contribute most to their delivery to the near-Earth space. It is widely accepted that a collision with a 10 km object over 66 million yr ago was responsible for the extinction of ∼75% of animal and plant species on Earth (e.g., Alvarez et al. 1980; Hildebrand et al. 1991; Dressler et al. 1994; Steuber et al. 2002). However, smaller objects, of tens of meters, can also pose a risk for civilization and result in significant local damage. The Tunguska event that occurred in 1908 and devastated an area of over $2200 \, km^2$ in Central Siberia is thought to have been caused by an ∼60 m diameter object that exploded in the atmosphere (e.g., Chyba et al. 1993; Jenniskens et al. 2019). More recently, the explosion of an ∼20 m meteor in Chelyabinsk, Russia, injured hundreds of people and caused extensive damage to the city. Events like these have

demonstrated the importance of finding and characterizing small NEOs, since collisions with these objects are more frequent than with larger bodies.

NEO surveys have been very successful at finding new objects, with over 34,600 NEOs discovered as of 2024 April (IAU Minor Planet Center Page). However, the physical characterization of these objects has lagged behind, with only a few studies dedicated to determining their rotation periods, taxonomy, and composition (e.g., Thomas et al. 2014; Thirouin et al. 2016, 2018; Binzel et al. 2019; Devogèle et al. 2019; Hromakina et al. 2023). Currently, taxonomic classifications are available for ∼15% of the known NEO population, but actual compositional analysis and/or established meteorite affinities are only available for a smaller fraction of NEOs.

Most near-infrared (NIR) spectroscopic surveys of NEOs carried out so far studied objects with a very broad size range, with samples often dominated by kilometer-sized asteroids, as these are the most accessible for ground-based telescopes (e.g., Vernazza et al. 2008; de León et al. 2010; Dunn et al. 2013; Thomas et al. 2014; Binzel et al. 2019). The present work seeks to complement previous efforts by focusing on the study of small NEOs (absolute magnitudes $H > 20$) while also addressing the U.S. Congress mandate, which in 2005 directed NASA to find and characterize at least 90% of potentially hazardous NEOs sized 140 m or larger. At the same time, we also investigate if the trends observed among larger NEOs in terms of taxonomic distribution, composition, and source regions remain the same for smaller objects.

Our study combines both spectroscopic and photometric data of small NEOs obtained over the course of ∼7 yr. In the spectroscopic study (Section 2), we analyze the NEO spectra employing different techniques, including thermal modeling, spectral band parameters, curve matching, and machine learning. We carry out the compositional analysis of the NEOs and look for possible meteorite analogs. Laboratory spectra of meteorite samples prepared by us are also used to help in the interpretation of the telescopic data. In addition, dynamical modeling is preformed to identify the source regions of the NEOs. In the photometric study (Section 3), we derive the lightcurves of a fraction of the NEOs and obtain rotational periods and lightcurve amplitudes. Moreover, we investigate possible relationships between axis ratios and absolute magnitudes and rotational periods. A summary of our main results is presented in Section 4.

2. Spectroscopic Study

2.1. Observations and Data Reduction

All NEOs presented in this study were observed with the SpeX instrument (Rayner et al. 2003) on the NASA Infrared Telescope Facility (IRTF) between 2013 October and 2021 January. In 2014, SpeX was upgraded, and the Raytheon Aladdin 3 1024×1024 InSb array in the spectrograph was replaced by a Teledyne 2048×2048 Hawaii-2RG array. NIR spectra (0.7–2.5 μm) were obtained in low-resolution ($R \sim 150$) prism mode with a 0.″8 slit width. During the observations, the slit was oriented along the parallactic angle in order to minimize the effects of differential atmospheric refraction. Spectra were obtained in two different slit positions (A-B) following the sequence ABBA. Depending on the magnitude of the asteroid, the integration time varied between 120 and 200 s. In order to correct the telluric bands from the asteroid spectra, a G-type local extinction star was observed before and after the asteroid. NIR spectra of a solar analog were also obtained to correct for possible spectral slope variations that could be introduced by the use of a nonsolar local extinction star. For asteroids fainter than V.mag ∼ 16.5, guiding was done using the MIT Optical Rapid Imaging System (MORIS) instrument, a high-speed visible-wavelength camera mounted on SpeX. Using nonsidereal tracking rates, MORIS can image fast-moving fainter targets ($>10'' \text{s}^{-1}$) with no trailing. This instrument has a pixel scale of 0.″11 pixel^{-1} for a field of view of $1' \times 1'$. MORIS images were saved and used to obtain the lightcurves of the asteroids (Section 3). For observations carried out prior to 2017, a 0.8 μm cut-on dichroic was used with MORIS; this dichroic was later replaced with a 0.7 μm dichroic during semester 2017A. For each night, calibration images including flat fields and argon arc-lamp spectra were also acquired. Observational circumstances for the 84 NEOs included in the spectroscopic study are presented in Table 1. The distribution of absolute magnitudes for these NEOs is shown in Figure 1.

Spectroscopic data were reduced using the IDL-based software Spextool (Cushing et al. 2004) and several Python scripts following the same procedure described in Sanchez et al. (2013). The data reduction procedure includes the following steps: (1) sky background removal by subtracting the A-B image pairs, (2) flat-fielding, (3) cosmic-ray and spurious-hit removals, (4) wavelength calibration, (5) division of asteroid spectra by the spectra of the local extinction star and

solar analog star, and (6) coadding of individual spectra. NIR spectra of the observed NEOs are shown in the Appendix (Figures 23–27).

2.2. Thermal Modeling

Seven objects in our sample show a thermal excess at wavelengths >2 μm. The location and magnitude of the thermal contribution in the NIR is an indicator of the surface temperature of the body. Thus, the amount of thermal flux emitted by an asteroid can be used to constrain its albedo (e.g., Reddy et al. 2009, 2012a; Kareta et al. 2022; Le Corre et al. 2023). The thermal flux of the asteroids was modeled following the same method described in Reddy et al. (2009, 2012a), which is a modified version of the standard thermal model (Lebofsky & Spencer 1989). Thermal models were generated for a given solar distance and phase angle for albedos ranging from 1% to 10%. An emissivity $\epsilon = 0.90$ and a beaming parameter $\eta = 0.75$ were used for all the models. The spectra along with the modeled albedo curves that can be fit to encompass the observed thermal fluxes are shown in Figure 2. The quality of the fit is largely dependent on the signal-to-noise ratio (S/N) of the spectra at long wavelengths. Spectra with a high point-to-point scatter at wavelengths >2 μm generally produce a poor fit (e.g., 2015 TF). This was one of the reasons why we choose to use a fixed value for η instead of leaving it as a free parameter, because we noticed that it produced a better fit for data with a low S/N. Geometric albedos obtained from the thermal modeling were used along with the absolute magnitudes of the NEOs to estimate their diameter using the following equation (Fowler & Chillemi 1992; Pravec & Harris 2007):

$$D = \left[\frac{1329}{\sqrt{P_V}} \right] \times 10^{-H/5}, \qquad (1)$$

where P_V is the geometric albedo and H is the absolute magnitude of the asteroid. Derived albedos and diameters are presented in Table 2. The final step was to use the models to remove the thermal excess from each spectrum, so the taxonomic classification can be applied.

2.3. Taxonomic Classification

The taxonomic classification of the NEOs was done using the Bus–DeMeo taxonomy classification web tool.[8] This online tool is an implementation of the Bus–DeMeo taxonomy (DeMeo et al. 2009), which uses principal component analysis to classify asteroids among 25 different classes. The Bus–DeMeo taxonomy requires visible and NIR spectra (0.45–2.45 μm) for the classification; however, most of our spectra cover the wavelength range of ∼0.7–2.45 μm. For objects whose NIR spectra show an absorption band at ∼1 μm, such as those in the S-complex, V-types, etc., and do not show features in the visible, we extrapolated the data to 0.45 μm. For objects whose spectra are featureless in the NIR, like most taxonomic types in the C- and X-complexes, we cannot use this procedure because in the visible, the spectra of these objects can have very different shapes that cannot be reproduced with a simple extrapolation. For this reason, for those objects, the taxonomic classification was done using only data from 0.8 to 2.45 μm. The main drawback of not having visible data is not

---

[8] http://smass.mit.edu/busdemeoclass.html

Table 1
Observational Circumstances

Number	Designation	Date (UT)	H (mag)	V (mag)	α (deg)	r (au)	Air Mass	Solar Analog
85990	1999 JV6	2015 Jan 11	20.2	16.7	44.5	1.04	1.14	SAO 120107
163348	2002 NN4	2020 Jul 1	20.1	18.0	32.5	1.16	1.21	SAO 83469
363599	2004 FG11	2016 Apr 9	21.0	17.1	62.1	1.03	1.29	SAO 120107
412995	1999 LP28	2018 Dec 12	20.1	17.1	15.3	1.14	1.27	SAO 93936
436724	2011 UW158	2015 Aug 8	19.9	16.7	71.4	1.03	1.11	SAO 31899
437844	1999 MN	2015 Jun 21	21.2	17.9	20.9	1.12	1.39	SAO 120107
438908	2009 XO	2020 May 12	20.7	14.9	19.0	1.05	1.29	SAO 120107
459872	2014 EK24[a]	2015 Feb 20	23.4	17.9	35.9	1.02	1.11	SAO 120107
467336	2002 LT38	2016 Jun 10	20.5	15.5	7.1	1.43	1.11	SAO 120107
469737	2005 NW44[a]	2016 Jul 13	20.4	18.1	29.2	1.16	1.25	SAO 120107
471240	2011 BT15	2014 Jan 8	21.7	17.3	60.2	1.01	1.04	SAO 120107
496816	1989 UP	2017 Oct 14	20.6	17.0	21.7	1.10	1.13	SAO 93936
501647	2014 SD224	2020 Dec 17	22.4	17.4	32.1	1.03	1.26	SAO 93936
515742	2015 CU[b]	2015 Feb 20	20.8	18.0	14.5	1.15	1.55	SAO 120107
515767	2015 JA2	2019 Feb 1	21.2	17.3	13.6	1.09	1.27	SAO 93936
528159	2008 HS3	2019 May 9	21.6	15.2	12.2	1.05	1.10	SAO 120107
	2000 TU28	2020 Oct 19	21.1	16.7	27.1	1.06	1.22	SAO 93936
	2001 YV3	2020 Dec 17	20.6	17.2	48.7	1.04	1.10	SAO 93936
	2002 LY1[a]	2016 Jun 10	22.3	17.8	55.3	1.04	1.08	SAO 120107
	2005 NE21	2019 Jul 11	21.3	17.8	11.2	1.15	1.38	SAO 120107
	2005 TF	2016 Nov 3	20.3	16.5	7.9	1.11	1.05	SAO 93936
	2006 XY	2017 Dec 16	24.2	15.8	47.2	0.99	1.45	SAO 93936
	2007 EC	2015 Jan 19	22.2	16.6	55.0	1.00	1.28	SAO 120107
	2012 ER14	2013 Oct 14	20.5	17.1	40.4	1.07	1.05	SAO 147208
	2013 CW32	2019 Feb 1	22.1	15.9	10.0	1.03	1.06	SAO 93936
	2013 RS43[b]	2013 Sep 13	27.0	18.2	49.6	1.01	1.28	SAO 147208
	2013 XA22	2020 May 31	22.9	17.1	31.4	1.05	1.21	SAO 120107
	2014 PL51	2014 Aug 25	20.4	16.9	35.3	1.09	1.29	SAO 93936
	2014 PR62	2014 Aug 22	20.6	17.4	13.6	1.15	1.26	SAO 93936
	2014 QH33[b]	2014 Aug 25	24.3	18.3	8.7	1.05	1.22	SAO 93936
	2014 QL32[b]	2014 Aug 26	22.8	18.7	26.5	1.08	1.14	SAO 93936
	2014 QZ265[b]	2014 Aug 26	25.3	19.2	35.5	1.04	1.12	SAO 93936
	2014 SF304[b]	2014 Oct 3	27.3	17.7	17.5	1.01	1.03	SAO 93936
	2014 SS1	2014 Sep 24	21.7	17.2	37.0	1.05	1.09	SAO 93936
	2014 UV210[b]	2014 Dec 16	26.9	18.7	5.4	1.00	1.06	SAO 120107
	2014 VH2[a]	2014 Nov 25	21.6	18.3	6.6	1.14	1.01	SAO 93936
	2014 VQ	2014 Nov 18	20.4	16.2	14.6	1.08	1.18	SAO 93936
	2014 WC201	2014 Dec 1	26.2	16.7	38.7	0.99	1.26	SAO 93936
	2014 WN4[a]	2014 Nov 18	23.3	18.0	17.0	1.04	1.15	SAO 93936
	2014 WO4[b]	2014 Nov 18	24.4	17.9	17.0	1.02	1.14	SAO 93936
	2014 WO7[b]	2014 Nov 25	20.5	18.9	10.7	1.26	1.27	SAO 93936
	2014 WP4[b]	2014 Nov 18	24.3	18.8	22.1	1.03	1.27	SAO 93936
	2014 WY119[a]	2014 Nov 25	26.3	18.1	37.0	0.99	1.22	SAO 93936
	2014 WZ120	2014 Nov 25	20.5	16.7	26.3	1.07	1.08	SAO 93936
	2014 XB6[b]	2014 Dec 16	26.5	20.3	63.8	0.99	1.31	SAO 120107
	2015 AK45[a]	2015 Jan 26	26.4	17.9	22.0	0.99	1.07	SAO 120107
	2015 AP43	2019 Jun 9	20.0	17.2	33.0	1.12	1.42	SAO 120107
	2015 BC	2015 Jan 19	24.0	15.3	40.0	0.99	1.13	SAO 120107
	2015 BK509	2020 Feb 24	22.4	18.0	44.0	1.03	1.03	SAO 93936
	2015 CA40[b]	2015 Feb 20	24.6	18.2	47.0	1.00	1.66	SAO 120107
	2015 CN13[b]	2015 Feb 20	23.3	18.4	23.7	1.04	1.35	SAO 120107
	2015 FL	2015 Apr 10	20.8	16.7	64.0	1.02	1.31	SAO 120107
	2015 GY[b]	2015 Apr 25	21.7	19.1	45.6	1.09	1.08	SAO 120107
	2015 HA1	2015 May 21	21.2	17.3	36.2	1.07	1.17	SAO 120107
	2015 HE10[b]	2015 Apr 25	26.1	19.1	39.2	1.02	1.77	SAO 120107
	2015 HW11[b]	2015 Apr 26	23.3	18.7	37.6	1.05	1.32	SAO 120107
	2015 JW[b]	2015 May 21	25.8	19.5	2.7	1.06	1.37	SAO 120107
	2015 KA[b]	2015 May 21	26.2	19.4	27.1	1.03	1.10	SAO 120107
	2015 LK24	2015 Jun 22	21.6	16.9	35.6	1.06	1.59	SAO 120107
	2015 MC[b]	2015 Jun 22	24.1	18.8	19.2	1.07	1.39	SAO 120107
	2015 NA14	2015 Jul 21	22.0	17.7	31.2	1.08	1.27	SAO 120107
	2015 SA[b]	2015 Sep 19	25.3	18.7	42.7	1.02	1.08	SAO 31899
	2015 SE[b]	2015 Sep 19	26.4	18.8	44.7	1.01	1.88	SAO 31899

Table 1
(Continued)

Number	Designation	Date (UT)	H (mag)	V (mag)	α (deg)	r (au)	Air Mass	Solar Analog
	2015 SZ[b]	2015 Oct 12	23.5	18.6	43.0	1.03	1.09	SAO 31899
	2015 TB25[a]	2015 Oct 12	24.5	17.8	28.5	1.02	1.02	SAO 31899
	2015 TC25	2015 Oct 12	29.3	17.5	32.0	1.00	1.58	SAO 31899
	2015 TE[b]	2015 Oct 12	22.5	18.6	37.5	1.06	1.54	SAO 31899
	2015 TF[a]	2015 Oct 12	22.2	18.7	3.6	1.15	1.50	SAO 31899
	2015 VE66	2015 Nov 22	24.1	16.3	13.8	1.01	1.22	SAO 93936
	2015 WF13[a]	2015 Dec 8	23.2	17.1	42.6	1.01	1.54	SAO 93936
	2015 XC[a]	2015 Dec 8	25.2	17.4	74.1	0.99	1.54	SAO 93936
	2016 BC14[a]	2016 Mar 7	20.9	17.8	64.6	1.03	1.10	SAO 120107
	2016 CM194	2016 Feb 13	27.7	13.7	59.6	0.99	1.13	SAO 93936
	2016 CO247	2021 Jan 15	20.6	16.6	15.3	1.08	1.07	SAO 93936
	2016 EB1[a]	2016 Mar 7	25.3	18.3	10.4	1.02	1.19	SAO 93936
	2016 EF28[a]	2016 Mar 7	21.7	17.9	21.9	1.08	1.02	SAO 120107
	2016 EV27[a]	2016 Apr 3	23.4	17.8	21.0	1.04	1.05	SAO 120107
	2016 FV13[a]	2016 Apr 9	25.8	17.9	47.3	1.01	1.24	SAO 120107
	2016 GU	2016 Apr 9	25.7	17.1	9.0	1.02	1.20	SAO 120107
	2016 JD18[b]	2016 May 13	24.6	18.4	32.0	1.04	1.20	SAO 120107
	2016 LG[a]	2016 Jun 10	25.3	18.5	57.8	1.02	1.05	SAO 120107
	2017 BS5	2017 Jul 23	24.2	15.2	33.7	1.02	1.50	SAO 53622
	2017 BW	2017 Feb 6	23.5	17.0	18.5	1.02	1.13	SAO 93936
	2017 BY93	2017 Feb 22	23.1	15.6	31.0	1.00	1.21	SAO 120107
	2017 CR32	2017 Mar 20	22.2	17.4	10.3	1.07	1.06	SAO 120107
	2017 DR34[a]	2017 Feb 24	29.2	18.2	8.3	0.99	1.08	SAO 120107
	2017 FU64[a]	2017 Apr 3	23.8	18.0	26.3	1.04	1.21	SAO 93936
	2017 OL1	2017 Aug 1	21.7	17.0	11.2	1.09	1.31	SAO 53622
	2017 OP68	2017 Sep 13	21.0	15.8	16.0	1.06	1.28	SAO 93936
	2017 RR15	2017 Oct 14	20.7	17.5	19.5	1.12	1.03	SAO 93936
	2017 WX12	2017 Dec 16	22.1	16.3	21.0	1.02	1.14	SAO 93936
	2018 XG5	2019 May 9	20.3	16.8	49.0	1.06	1.10	SAO 120107
	2018 XS4	2018 Dec 17	25.2	16.6	42.4	0.99	1.03	SAO 93936
	2019 AN5	2020 Aug 17	21.1	17.1	57.1	1.04	1.37	SAO 109542
	2019 GT3	2019 Sep 10	21.0	16.5	42.0	1.05	1.31	SAO 93936
	2019 JL3	2019 May 18	25.0	17.2	50.0	1.02	1.05	SAO 120107
	2019 JX7	2019 Jun 9	21.5	17.9	41.3	1.08	1.02	SAO 120107
	2019 RC	2019 Sep 10	21.8	18.0	49.2	1.05	1.28	SAO 93936
	2019 SH6	2020 Jan 4	20.0	17.3	53.0	1.05	1.13	SAO 93936
	2019 UO13	2019 Nov 3	23.8	16.7	24.8	1.01	1.52	SAO 93936
	2019 YM3	2020 Jan 2	23.3	17.9	17.6	1.03	1.02	SAO 93936
	2020 DZ1	2020 Feb 24	24.0	17.6	14.5	1.02	1.35	SAO 93936
	2020 HS6	2020 May 12	22.2	17.6	44.8	1.05	1.12	SAO 120107
	2020 KC5	2020 May 29	27.4	17.6	67.1	1.02	1.23	SAO 120107
	2020 RO6	2021 Jan 15	22.4	17.6	35.8	1.03	1.12	SAO 93936
	2020 SN	2020 Sep 22	24.8	17.2	5.8	1.03	1.09	SAO 93936
	2020 ST1	2020 Nov 17	22.0	16.4	12.8	1.04	1.22	SAO 93936
	2020 YQ3	2021 Jan 15	20.0	17.9	21.1	1.17	1.3	SAO 93936

Notes. The columns in this table are: object number and designation, date, absolute magnitude (H), V magnitude (V), phase angle (α), heliocentric distance (r), air mass, and solar analog used.

[a] Asteroid observed with the 0.8 μm dichroic.

[b] The S/N of the spectrum was deemed too low to be published. Only photometric data could be used.

being able to distinguish between most of the types that comprise the C- and X-complexes, with the exception of the Xe-, Xk-, and Xn-types that exhibit a weak absorption band at ∼0.9 μm. Due to this limitation, in the present work, we have combined the C- and X-complexes into the same group (C/X).

The other instance where only data from 0.8 to 2.45 μm were used for taxonomic classification was when the spectra were obtained using the 0.8 μm dichroic. In those cases, more data are missing, and it is not possible to extrapolate the data. This, however, does not represent a major problem for the classification of asteroids whose spectra show prominent absorption bands, such as those belonging to the S-complex or V-types.

The taxonomic type assigned to each NEO is presented in Table 3. If during the classification process more than one taxonomic type was assigned to an asteroid, a visual inspection was performed to determine the class that best represents the spectral characteristics of the asteroid. We also compared the average absolute residuals between the NEO and the reference spectra obtained from the Bus–DeMeo taxonomy classification
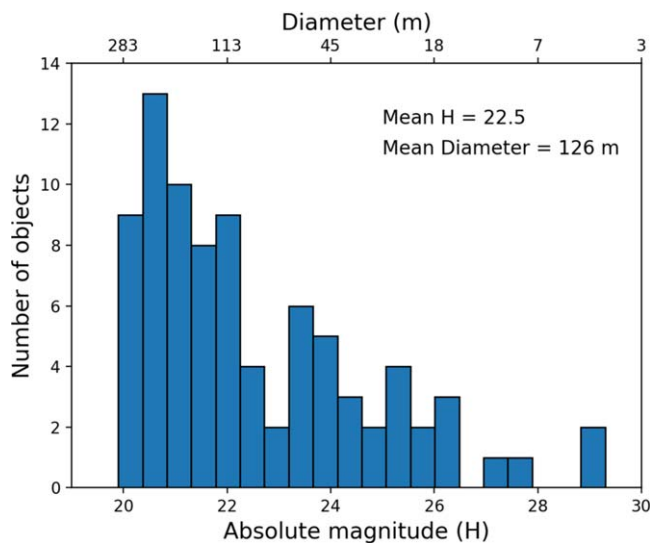
Figure 1. Distribution of absolute magnitudes (*H*) and diameters for the NEOs included in the spectroscopic study. Diameters were calculated from the absolute magnitudes and the mean geometric albedo of the sample ($P_V = 0.22$).

web tool. There was one case where the classification was indeterminate, and it has been indicated in Table 3.

The classification of NEOs 2013 CW32, 2016 CM194, 2017 WX12, and 2019 SH6 yielded very ambiguous results, with all of them being assigned multiple taxonomies including C-, X-, and S-complex, as well as K- and L-types. This happened because, even though the spectra of these objects are similar to those in the S-complex, their absorption bands are much weaker. For this reason, and in order to highlight these unusual characteristics, in the present study we refer to these objects as Sx-types. Thus, we define Sx-types as objects whose NIR spectra are similar to those in the S-complex but that, due to their weak absorption bands, could fall in the region of the PC2′ versus PC1′ diagram, where the C- and X-complexes normally fall. The composition of these objects and the possible causes for their weak absorption bands are discussed in Sections 2.4.2 and 2.6, respectively.

Figure 3 shows the distribution of taxonomic types. We found that the most common taxonomic type in our sample is the Sq-type, followed by the S-, Q-, and Sr-types. The fraction of the main taxonomic types is shown in Figure 4. NEOs classified as S-complex represent ∼66% of the entire sample, objects in the C/X-complex represent ∼17%, and the other ∼17% are less common taxonomic types. Our results are consistent with the work done by Binzel et al. (2019), who found a fractional distribution of 60% S, 20% C, and 20% other types for NEOs in the size range of 100 m to 10 km. It is worth noting that in the original Bus–DeMeo classification (DeMeo et al. 2009), Q-types are not considered part of the S-complex, but they are in DeMeo et al. (2022). Binzel et al. (2019) followed the same definition as DeMeo et al. (2009), whereas in the present work, we use that of DeMeo et al. (2022). The new subclass of Sx-types is also included within the S-complex in Figure 4.

For the majority of the NEOs in this study, the albedo is unknown; however, having information about their taxonomic type and the mean albedo for those types, it is possible to do an estimation of their size using Equation (1). Thus, the diameters shown in Figure 1 were calculated from the absolute magnitudes of the NEOs and the mean albedos of their

taxonomic types found by Marsset et al. (2022). The mean geometric albedo of the spectroscopic sample was found to be $P_V = 0.22$.

### 2.4. Compositional Analysis and Meteorite Analogs

2.4.1. S-complex Asteroids

Asteroids in the S-complex include those that were classified as S-, Sq-, Sr-, Sx-, and Q-types. The spectra of all these objects show absorption bands at ∼1 and 2 μm due to the minerals olivine and pyroxene. Olivine has three overlapping bands centered near 1.04–1.1 μm, and pyroxene has two absorption bands centered near 0.9–1 μm and 1.9–2 μm (Adams 1974; Burns 1993). These absorption bands are caused by the presence of Fe^{2+} cations. Diagnostic spectral band parameters including the Band I and II centers and band area ratio (BAR) were measured using a Python code following the procedure described in Sanchez et al. (2020). Band centers were measured after dividing out the linear continuum by fitting third- and fourth-order polynomials over the bottom of the absorption bands. Band areas are defined as the area between the linear continuum and the data curve and are calculated using trapezoidal numerical integration. The BAR was calculated as the ratio of the area of Band II to that of Band I. A temperature correction derived by Sanchez et al. (2012) was applied to the BAR in order to account for differences between the surface temperature of the NEOs and the room temperature at which spectral calibrations used for compositional analysis were obtained. The uncertainties associated with the band parameters are given by the standard deviation of the mean calculated from multiple measurements of each band parameter. Spectral band parameters are shown in Table 4.

Prior to the compositional analysis, it is useful to plot the spectral band parameters in the Band I center versus the BAR diagram from Gaffey et al. (1993) to determine the S-asteroid subtype. The results shown in Figure 5 indicate that most of the NEOs in the S-complex belong to the S(IV) subtype, which also represents the mafic silicate components of ordinary chondrites (Gaffey et al. 1993). These meteorites are the most common type to fall to Earth, representing about 86% of all meteorites. They are divided into three subgroups (H, L, LL) based on the abundance of Fe and the ratio of metallic Fe (Fe^0) to oxidized Fe (FeO) (Weisberg et al. 2006).

NEOs 363599, 2005 NE21, 2005 TF, 2015 HA1, 2019 JL3, and 2020 YQ3 were found to fall into the S(III) subtype. Objects in this subtype can contain a calcic pyroxene component; some ordinary chondrites can fall in this region as well (e.g., Dunn et al. 2010; Sanchez et al. 2020). In the particular case of 2005 NE21, it is worth mentioning that the spectrum shows a low S/N and large scattering in the 2 μm band, which can lead to an overestimation of the BAR moving the object from the S(IV) to the S(III) subtype.

One NEO, 2019 UO13, was found to be an S(V) subtype. This class of asteroids is thought to have experienced intrusion of early partial melts into their crust and upper mantle (Gaffey et al. 1993). A highly metamorphosed H-chondrite or a calcic pyroxene-bearing lodranite are possible meteorite analogs for these objects. The NEO 2014 WZ120 falls slightly below the S(IV) subtype, which is possible for some ordinary chondrites, although we cannot rule out an affinity with primitive achondrites (acapulcoites and lodranites) that are also located in this region (Lucas et al. 2019). NEOs 436724 and 2018 XS4
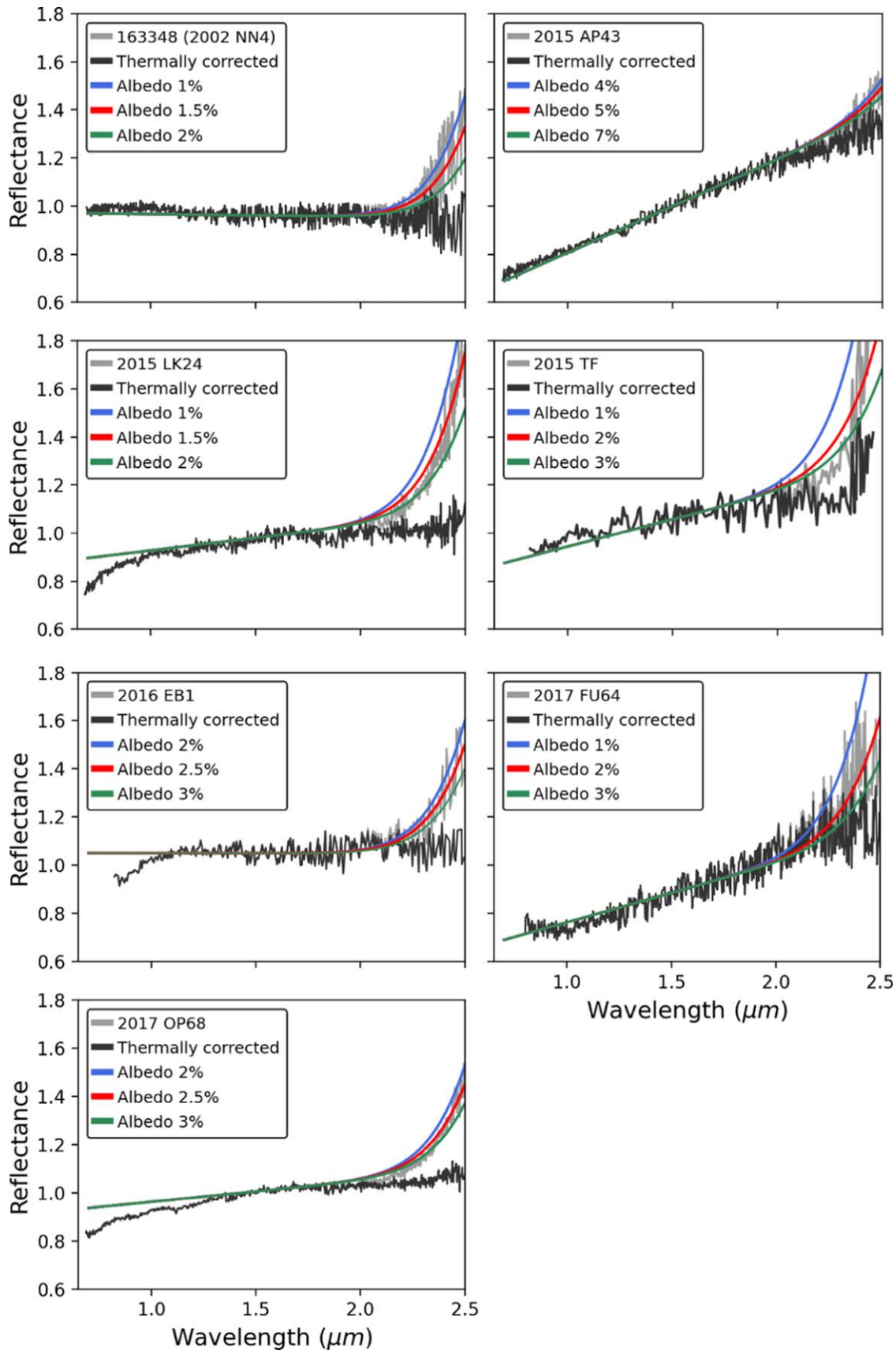
Figure 2. NIR spectra of asteroids 163348 (2002 NN4), 2015 AP43, 2015 LK24, 2015 TF, 2016 EB1, 2017 FU64, and 2017 OP68. Modeled albedo curves that encompass the observed thermal fluxes and thermally corrected spectra are shown.

Table 2
Albedos and Diameters Resulting from the Thermal Modeling

Number	Designation	Albedo	H (mag)	Diameter (m)
163348	2002 NN4	0.015 ± 0.005	20.1 ± 0.5	1036 ± 295
	2015 AP43	0.050 ± 0.020	20.0 ± 0.5	594 ± 181
	2015 LK24	0.015 ± 0.005	21.6 ± 0.5	519 ± 148
	2015 TF	0.020 ± 0.010	22.2 ± 0.5	341 ± 116
	2016 EB1	0.025 ± 0.005	25.3 ± 0.5	73 ± 18
	2017 FU64	0.020 ± 0.010	23.8 ± 0.5	163 ± 56
	2017 OP68	0.025 ± 0.005	21.0 ± 0.5	530 ± 133

are both classified as S(VI) subtype. Objects in this subtype contain low-Ca pyroxene and less olivine than olivine-poor ordinary chondrites (Gaffey et al. 1993). Winonaites and the inclusions present in the IAB iron meteorites have been proposed as possible meteorite analogs for this subtype (Gaffey et al. 1993). Like in the case of 2005 NE21, 436724 also shows a large scattering in the 2 μm band, which could be causing an overestimation of the BAR.

Since the majority of the S-complex NEOs in our sample fall in the S(IV) subtype (or the vicinity), as a first approximation, the composition of these objects can be determined with spectral calibrations developed from ordinary chondrites. For this, we used the Band I center and BAR along with the equations derived by Sanchez et al. (2020). These equations are a modified version of the original spectral calibrations obtained by Dunn et al. (2010) from the analysis of ordinary chondrites. The equations obtained by Sanchez et al. (2020) are more appropriated for low-S/N spectra and can be used with incomplete spectra like the ones obtained with the 0.8 μm dichroic. The Band I center was used to determine the olivine and pyroxene chemistries, which are given by the mol% of fayalite (Fa) and ferrosilite (Fs), respectively. For those objects where the BAR was measured, the olivine-to-pyroxene ratio (ol/(ol+px)) was also calculated. Figure 6 shows the olivine and pyroxene chemistries versus the ol/(ol+px) ratio for the NEOs. These values are also presented in Table 4. As mentioned before, there are at least a couple of cases where the BAR values could have been overestimated. Because this would result in an underestimation of the ol/(ol+px) ratios, these values must be taken as a lower limit.

There are a few NEOs in our sample whose spectra do not show the 2 μm absorption band; in those cases, only the Band I centers were used for the compositional analysis. The molar contents of Fa and Fs of these asteroids are compared with data from Nakamura et al. (2011) in Figure 7.

In order to classify these objects into the three ordinary chondrite subtypes, we built a supervised machine-learning algorithm based on multinomial logistic regression. This method is a generalization of logistic regression, and it is used for multiclass classification (e.g., Bishop 2006). Multinomial logistic regression uses the softmax function to convert a vector of K real numbers into a probability distribution of K possible outcomes. This allow us to predict not only the class of each asteroid (H, L, or LL) but also the probability of the asteroid belonging to that specific class.

Given an input feature $x^{(i)}$ and a class label $y^{(i)} \in \{1, 2, ..., K\}$, where K is the number of classes, we want to estimate the probability that $y^{(i)}$ equals k for each value of $k = 1, 2, ..., K$.

The predicted probability for the kth class is given by

$$P(y^{(i)} = k | x^{(i)}; \theta) = \frac{e^{\theta^{(k)T} x^{(i)}}}{\sum_{j=1}^{K} e^{\theta^{(j)T} x^{(i)}}}, \qquad (2)$$

where $\theta^T x$ is the regression result, i.e., the sum of the variables weighted by the coefficients. The difference between the actual and the predicted values give us the error of our model, which is calculated by the cost function:

$$J(\theta) = -\left[\sum_{i=1}^{m} \sum_{k=1}^{K} 1\{y^{(i)} = k\} \log \frac{e^{\theta^{(k)T} x^{(i)}}}{\sum_{j=1}^{K} e^{\theta^{(j)T} x^{(i)}}} \right]. \qquad (3)$$

Since the cost shows how poorly the model is estimating the labels, the idea is to train our model to minimize this cost.

We started by creating a synthetic multiclass data set to train and test the model. For each ordinary chondrite subtype, 500 data points with three input variables (ol/(ol+px), Fa, Fs) were generated using the boundaries found by Sanchez et al. (2020). The synthetic data are shown in Figure 6. This data set was then split into a training and a testing set. For the testing set, 20% of the whole sample was randomly selected. This provides a more accurate evaluation on out-of-sample accuracy because the testing data set is not part of the data set that has been used to train the data. In order to prevent overfitting, we employed regularization; i.e., we used the L2 (Ridge) penalty, which is a type of regularization that adds a penalty term equal to the sum of the squares of the weights to the cost function. The strength of the penalty is controlled by the hyperparameter C (the inverse of the regularization strength). The model was fit to the training set using the limited-memory Broyden–Fletcher–Goldfarb–Shanno optimization algorithm with a tenfold cross validation. A grid search method was used to find the optimal value of C. Finally, we evaluated the performance of the model on the testing set, and the F1 score and logarithmic loss (log loss) were calculated. The F1 score is the harmonic mean of the precision and recall, and it ranges from 0 to 1, where an F1 score reaches its best value at 1 (perfect precision and recall). The log loss is used to evaluate the performance of the classifier, where the predicted output is a probability value between 0 and 1. The resulting log-loss value quantifies how close the predicted probabilities are to the true class labels; a perfect model would yield a value of 0.

Figure 8 shows the normalized confusion matrix resulting from evaluating the model on the testing set. Approximately 95% of the H-chondrites were correctly classified by the model, and ~5% of them were classified as L-chondrites. A slightly lower number of L-chondrites (~92%) were correctly classified by the model, and the remaining ~8% were classified as H- and LL-chondrites. This comes as no surprise since L-chondrites overlap with both H- and LL-chondrites. Approximately 95% of the LL-chondrites were correctly classified, and ~5% of them were classified as L-chondrites. The F1 score and log loss yielded values of 0.94 and 0.14, respectively.

The model was applied to all the NEOs with an ordinary chondrite-like composition (56 in total). For the few objects whose spectra do not show the 2 μm absorption band and for which only the Fa and Fs were calculated, we modified our model to perform the classification using only these two input variables. The probabilities of the NEOs belonging to the three subtypes (H, L, LL) are shown in Figure 9. The best meteorite analogs for each NEO are included in Table 3. We found that

Table 3
Taxonomic Classification and Meteorite Analogs for the Studied NEOs

Number	Designation	Taxonomy	Meteorite Analog	Designation	Taxonomy	Meteorite Analog
85990	1999 JV6	Xk	NC-Euc, SI, I	2015 TB25	L	CC
163348	2002 NN4	B	CC	2015 TC25	Xn	A
363599	2004 FG11	Q	LL-OC	2015 TF	C/X	CC
412995	1999 LP28	Sqw	LL-OC	2015 VE66	Sr	L-OC
436724	2011 UW158	S	H-OC	2015 WF13	V	NC-Euc
437844	1999 MN	Q	LL-OC	2015 XC	V	C-Euc
438908	2009 XO	Q	LL-OC	2016 BC14	S	L-OC
459872	2014 EK24	Sq	LL-OC	2016 CM194	Sx	L-OC, SD, PA
467336	2002 LT38	Sq	LL-OC	2016 CO247	C/X	A, EC
469737	2005 NW44	Sq	LL-OC	2016 EB1	C/X	CC
471240	2011 BT15	Sr	L-OC	2016 EF28	V	NC-Euc
496816	1989 UP	Sq	LL-OC	2016 EV27	Q	LL-OC
501647	2014 SD224	Sq	LL-OC	2016 FV13	Q	L-OC
515767	2015 JA2	Sq	LL-OC	2016 GU	Xn	A, EC
528159	2008 HS3	Sq	LL-OC	2016 LG	Q	LL-OC
	2000 TU28	Sq	LL-OC	2017 BS5	S	LL-OC
	2001 YV3	Q	LL-OC	2017 BW	L	CC
	2002 LY1	C/X	A, EC, CC	2017 BY93	Sq	L-OC
	2005 NE21	S	LL-OC	2017 CR32	L	CC
	2005 TF	Q	LL-OC	2017 DR34	S	H-OC
	2006 XY	C/X	A, EC, CC	2017 FU64	D	CC
	2007 EC	Sq	LL-OC	2017 OL1	S	L-OC
	2012 ER14	D	CC	2017 OP68	C/X	CC
	2013 CW32	Sx	L-OC, MR-OC	2017 RR15	V	C-Euc
	2013 XA22	Sq	L-OC	2017 WX12	Sx	LL-OC, SD, MR-OC
	2014 PL51	Q	LL-OC	2018 XG5	Sr	L-OC
	2014 PR62	K	LL-OC	2018 XS4	Sr	H-OC
	2014 SS1	S	L-OC	2019 AN5	Sqw	LL-OC
	2014 VH2	L	CC	2019 GT3	Srw	L-OC
	2014 VQ	Sqw	LL-OC	2019 JL3	Sqw	LL-OC
	2014 WC201	Sq	L-OC	2019 JX7	Q	LL-OC
	2014 WN4	C/X	A, EC, CC	2019 RC	D	CC
	2014 WY119	Sq	LL-OC	2019 SH6	Sx	LL-OC, SD, MR-OC
	2014 WZ120	Sr	H-OC, PA	2019 UO13	Sr	L-OC
	2015 AK45	Sr	L-OC	2019 YM3	Qw	LL-OC
	2015 AP43	D	CC	2020 DZ1	S	LL-OC
	2015 BC	Xk	How, SI, I	2020 HS6	Sq	LL-OC
	2015 BK509	Srw	LL-OC	2020 KC5	S	L-OC
	2015 FL	IND	IND	2020 RO6	V	NC-Euc
	2015 HA1	Sq	LL-OC	2020 SN	Xk	A, EC
	2015 LK24	C/X	CC	2020 ST1	Sw	L-OC
	2015 NA14	S	L-OC	2020 YQ3	Sq	LL-OC

Notes. If the classification result is indeterminate, the letters IND are used. Meteorite abbreviations are H-, L-, and LL-ordinary chondrites (H/L/LL-OC); howardite (How); noncumulate eucrite (NC-Euc); cumulate eucrite (C-Euc); carbonaceous chondrite (CC); aubrite (A); enstatite chondrite (EC); primitive achondrite (PA); metal-rich chondrite (MR-OC); stony-iron meteorite (SI); and iron meteorite (I). The possible presence of shock darkening is indicated as SD. If no meteorite analog was identified, the letters IND are used.

8% of the objects in the S-complex were classified as H-, 31% as L-, and 61% as LL-chondrites (Figure 4). These NEOs have diameters ranging from ∼8 to 284 m with a mean value of ∼138 m.

Dunn et al. (2013) analyzed 47 NEOs with ordinary chondrite-like compositions and found a proportion of 15% H-, 10% L-, and 60% LL-chondrites among these bodies. The remaining 15% could not be distinguished between L- and LL-chondrites. Thomas et al. (2014) used a larger sample consisting of 109 NEOs and found a proportion of 22.9% H-, 10.1% L-, and 40.4% LL-ordinary chondrites. The rest of the objects were found to have overlapping (8.3% H/L and 12.8% L/LL) or potentially inconsistent compositions (3.7% H and 1.8% LL). Binzel et al. (2019), on the other hand, spectrally modeled 194

NEOs as ordinary chondrites and found that ∼29% were consistent with H-, ∼20% with L-, and ∼51% with LL-chondrites. Our results agree with previous studies that showed that LL-chondrites are dominant among NEOs with ordinary chondrite-like compositions. The different proportions of each ordinary chondrite subtype are probably the result of several factors, such as the use of a sample with smaller objects, the intrinsic difficulty of classifying ordinary chondrites that can have overlapping compositions, and the use of different procedures for the compositional analysis.

Vernazza et al. (2008) first noticed that LL-chondrites were the most common type among S-complex NEOs. This result was unexpected because LL-chondrites only represent 10% of all ordinary chondrite falls. This discrepancy has been attributed to
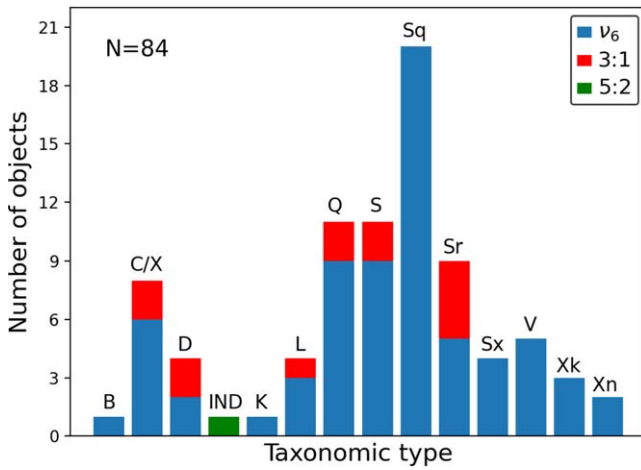
Figure 3. Distribution of taxonomic types found in the present study. The label C/X corresponds to objects with ambiguous C- or X-complex classification. The label IND is assigned to objects whose taxonomic classification is indeterminate. The Sx-types are a new subclass of objects introduced in the present study. The source regions of the NEOs are indicated with different colors.

the size of the NEOs studied (typically tens of meters to kilometers), which might be too large to be the immediate parent bodies of the meteorites that fall on Earth. The Yarkovsky effect is more efficient at delivering meter-sized objects from the asteroid belt to the near-Earth space. Therefore, it is possible that smaller NEOs could have compositions more similar to what we see among ordinary chondrite meteorites (e.g., Vernazza et al. 2008; Binzel et al. 2019). If this is true, then this means that most of the NEOs in our sample with ordinary chondrite-like compositions are too large to be the parent bodies of the ordinary chondrite meteorites.

2.4.2. Sx-type Asteroids

In Section 2.3, we introduced this new subclass of the S-complex to make the distinction that their NIR spectra exhibit absorption bands that are much weaker than the typical objects in the S-complex. The four NEOs that were assigned this class are 2013 CW32, 2016 CM194, 2017 WX12, and 2019 SH6. The composition of these NEOs was determined in the same way as the other objects in the S-complex.

In the Band I center versus BAR plot, 2013 CW32 is located in the region corresponding to the S(IV) subtypes (Figure 5). For this object, we found that L-chondrites are the closest in composition. 2016 CM194 was classified as an S(VI) subtype in the Band I center versus BAR plot. The compositional analysis of this NEO yielded an olivine and pyroxene chemistry similar to L-chondrites. However, given its classification as an S(VI) subtype, it could also have an affinity with primitive achondrites. Both 2017 WX12 and 2019 SH6 fall in the S(III) subtype of the Band I center versus BAR plot. For these two objects, the olivine and pyroxene chemistry as well as the ol/(ol+px) ratio are consistent with LL-chondrites. The possible reasons behind the particular spectral characteristics of these asteroids are investigated in more detail in Section 2.6.

2.4.3. V-type Asteroids

NEOs 2015 WF13, 2015 XC, 2016 EF28, 2017 RR15, and 2020 RO6 were classified as V-types. In the Band I center versus BAR plot, 2017 RR15 and 2020 RO6, which are the only ones

that were observed without the 0.8 μm dichroic, are located in the basaltic achondrites region (Figure 5). V-type asteroids are linked to asteroid 4 Vesta and to howardite, eucrite, and diogenite (HED) meteorites based on their spectral similarities (e.g., McCord et al. 1970; Consolmagno & Drake 1977; Moskovitz et al. 2010). Eucrites are basaltic rocks composed mainly of calcium-rich plagioclase feldspar, augite, and pigeonite. Diogenites are orthopyroxene-rich rocks that formed deeper than the eucrites (lower crust/upper mantle) and cooled slowly. Howardites are physical mixtures of eucrites and diogenites (e.g., Mittlefehldt et al. 1998; Mittlefehldt 2015).

The compositional analysis of the V-type NEOs was done using their band centers. Since these parameters can be affected by temperature variations, we first applied the temperature corrections derived by Reddy et al. (2012b) from the analysis of HED meteorites. For those asteroids whose spectra were obtained without the 0.8 μm dichroic, both band centers were used along with the equations of Burbine et al. (2009). These equations are used to determine the pyroxene chemistry, which is given by the molar contents of ferrosilite (Fs) and wollastonite (Wo). For asteroids whose spectra were obtained with the 0.8 μm dichroic, only the Band II centers were used to determine their composition (Table 4).

Figure 10 shows the molar contents of wollastonite (Wo) versus ferrosilite (Fs) for the V-type NEOs and the regions corresponding to the howardites, noncumulate eucrites, cumulate eucrites, and diogenites. In order to determine the probability of each V-type belonging to a specific class, we built a machine-learning model like the one used with the S-complex asteroids. In this case, the synthetic multiclass data set was generated with two input variables (Wo and Fs) and the boundaries shown in Figure 10.

NEOs 2015 WF13, 2016 EF28, and 2020 RO6 were classified as noncumulate eucrites. These are the most common type of eucrites and represent surface or near-surface basalts (Mittlefehldt 2015). NEOs 2015 XC and 2017 RR15, on the other hand, were classified as cumulate eucrites, which are thought to represent subsurface cumulate layers formed by fractional crystallization (Mittlefehldt 2015). For 2015 XC, Figure 10 shows some overlap between the cumulate eucrite and the howardite regions; however, our model favors cumulate eucrites as the best meteorite analogs with a 66% probability.

2.4.4. C/X-complex and B-type Asteroids

As explained earlier, our spectroscopic data do not cover most of the visible wavelength range. This is particularly problematic for the compositional analysis of those asteroids in the C/X-complex whose spectra show diagnostic features in the visible. NEOs that were classified as C/X-complex include 2002 LY1, 2006 XY, 2014 WN4, 2015 LK24, 2015 TF, 2016 CO247, 2016 EB1, and 2017 OP68. For objects like these, with weak features or featureless spectra, we used the Modeling for Asteroids online tool (Popescu et al. 2012) to look for possible meteorite analogs. If a good spectral match was found, it is shown along with the spectrum of the asteroid in Figure 11. For NEOs 2015 LK24, 2015 TF, and 2016 EB1, no good meteorite analogs were found. However, the thermal excess and low albedos calculated for these asteroids suggest that they might be composed of carbonaceous-chondrite-like material. We also noticed that the albedos of these NEOs, which range from 0.015 to 0.025, are closer to the albedo of P-type asteroids, which have a mean value of 0.03 ± 0.01 (Marsset et al. 2022).

Table 4
Spectral Band Parameters and Composition for the NEOs

Number	Designation	BIC (μm)	BIIC (μm)	BAR	Fa (mol%)	Fs (mol%)	Wo (mol%)	ol/(ol+px)
85990	1999 JV6	0.938 ± 0.006	2.041 ± 0.019	2.12 ± 0.22	⋯	46 ± 3	11 ± 1	⋯
163348	2002 NN4	⋯	⋯	⋯	⋯	⋯	⋯	⋯
363599	2004 FG11	0.997 ± 0.003	2.063 ± 0.011	0.55 ± 0.02	30.2 ± 2.0	25.1 ± 1.4	⋯	0.59 ± 0.04
412995	1999 LP28	1.023 ± 0.005	⋯	⋯	30.6 ± 2.0	25.4 ± 1.4	⋯	⋯
436724	2011 UW158	0.932 ± 0.006	2.024 ± 0.023	1.42 ± 0.07	21.5 ± 2.0	19.1 ± 1.4	⋯	0.38 ± 0.04
437844	1999 MN	0.980 ± 0.003	2.036 ± 0.014	0.51 ± 0.02	28.9 ± 2.0	24.3 ± 1.4	⋯	0.60 ± 0.04
438908	2009 XO	1.016 ± 0.002	2.022 ± 0.012	0.41 ± 0.01	30.7 ± 2.0	25.4 ± 1.4	⋯	0.62 ± 0.04
459872	2014 EK24	0.974 ± 0.004	1.931 ± 0.025	0.92 ± 0.06	27.5 ± 2.0	23.3 ± 1.4	⋯	0.56 ± 0.04
467336	2002 LT38	0.990 ± 0.003	2.004 ± 0.007	0.43 ± 0.02	29.7 ± 2.0	24.8 ± 1.4	⋯	0.61 ± 0.04
469737	2005 NW44	0.982 ± 0.005	1.960 ± 0.010	0.85 ± 0.04	28.4 ± 2.0	23.9 ± 1.4	⋯	0.57 ± 0.04
471240	2011 BT15	0.941 ± 0.003	1.942 ± 0.023	0.49 ± 0.01	23.3 ± 2.0	20.4 ± 1.4	⋯	0.60 ± 0.04
496816	1989 UP	1.010 ± 0.005	1.991 ± 0.012	0.38 ± 0.01	30.6 ± 2.0	25.4 ± 1.4	⋯	0.63 ± 0.04
501647	2014 SD224	0.981 ± 0.006	2.018 ± 0.014	0.48 ± 0.02	29.0 ± 2.0	24.3 ± 1.4	⋯	0.60 ± 0.04
515767	2015 JA2	0.992 ± 0.005	⋯	⋯	29.9 ± 2.0	24.9 ± 1.4	⋯	⋯
528159	2008 HS3	0.996 ± 0.003	1.956 ± 0.012	0.34 ± 0.01	30.1 ± 2.0	25.1 ± 1.4	⋯	0.64 ± 0.04
	2000 TU28	0.990 ± 0.002	2.018 ± 0.006	0.41 ± 0.02	29.7 ± 2.0	24.8 ± 1.4	⋯	0.62 ± 0.04
	2001 YV3	0.995 ± 0.001	2.036 ± 0.011	0.38 ± 0.01	30.1 ± 2.0	25.0 ± 1.4	⋯	0.63 ± 0.04
	2002 LY1	⋯	⋯	⋯	⋯	⋯	⋯	⋯
	2005 NE21	0.976 ± 0.002	1.903 ± 0.024	0.65 ± 0.03	28.5 ± 2.0	24.0 ± 1.4	⋯	0.56 ± 0.04
	2005 TF	1.009 ± 0.007	2.003 ± 0.010	0.52 ± 0.02	30.6 ± 2.0	25.4 ± 1.4	⋯	0.59 ± 0.04
	2006 XY	⋯	⋯	⋯	⋯	⋯	⋯	⋯
	2007 EC	1.003 ± 0.002	2.020 ± 0.011	0.42 ± 0.03	30.4 ± 2.0	25.3 ± 1.4	⋯	0.62 ± 0.04
	2012 ER14	⋯	⋯	⋯	⋯	⋯	⋯	⋯
	2013 CW32	0.941 ± 0.006	1.988 ± 0.013	0.98 ± 0.04	23.3 ± 2.0	20.4 ± 1.4	⋯	0.49 ± 0.04
	2013 XA22	0.958 ± 0.002	1.992 ± 0.012	0.77 ± 0.01	26.2 ± 2.0	22.4 ± 1.4	⋯	0.53 ± 0.04
	2014 PL51	1.004 ± 0.003	1.939 ± 0.015	0.46 ± 0.02	30.5 ± 2.0	25.3 ± 1.4	⋯	0.61 ± 0.04
	2014 PR62	1.001 ± 0.009	⋯	⋯	30.3 ± 2.0	25.2 ± 1.4	⋯	⋯
	2014 SS1	0.949 ± 0.001	1.992 ± 0.015	0.55 ± 0.03	24.8 ± 2.0	21.4 ± 1.4	⋯	0.59 ± 0.04
	2014 VH2	⋯	⋯	⋯	⋯	⋯	⋯	⋯
	2014 VQ	1.016 ± 0.001	2.022 ± 0.009	0.40 ± 0.02	30.7 ± 2.0	25.4 ± 1.4	⋯	0.62 ± 0.04
	2014 WC201	0.936 ± 0.003	1.940 ± 0.014	1.01 ± 0.02	22.3 ± 2.0	19.7 ± 1.4	⋯	0.48 ± 0.04
	2014 WN4	⋯	⋯	⋯	⋯	⋯	⋯	⋯
	2014 WY119	0.971 ± 0.010	⋯	⋯	27.2 ± 2.0	23.1 ± 1.4	⋯	⋯
	2014 WZ120	0.915 ± 0.001	1.952 ± 0.024	0.92 ± 0.07	17.4 ± 2.0	16.2 ± 1.4	⋯	0.50 ± 0.04
	2015 AK45	0.974 ± 0.002	1.989 ± 0.016	1.17 ± 0.13	27.5 ± 2.0	23.3 ± 1.4	⋯	0.52 ± 0.04
	2015 AP43	⋯	⋯	⋯	⋯	⋯	⋯	⋯
	2015 BC	0.925 ± 0.009	2.001 ± 0.026	1.58 ± 0.14	⋯	32 ± 3	5 ± 1	⋯
	2015 BK509	0.962 ± 0.003	1.947 ± 0.036	0.60 ± 0.07	26.8 ± 2.0	22.8 ± 1.4	⋯	0.58 ± 0.04
	2015 FL	⋯	⋯	⋯	⋯	⋯	⋯	⋯
	2015 HA1	1.010 ± 0.001	1.994 ± 0.010	0.53 ± 0.05	30.6 ± 2.0	25.4 ± 1.4	⋯	0.59 ± 0.04
	2015 LK24	⋯	⋯	⋯	⋯	⋯	⋯	⋯
	2015 NA14	0.942 ± 0.004	1.994 ± 0.018	0.94 ± 0.05	23.5 ± 2.0	20.5 ± 1.4	⋯	0.49 ± 0.04
	2015 TB25	⋯	⋯	⋯	⋯	⋯	⋯	⋯
	2015 TC25	0.905 ± 0.003	⋯	⋯	⋯	⋯	⋯	⋯
	2015 TF	⋯	⋯	⋯	⋯	⋯	⋯	⋯
	2015 VE66	0.937 ± 0.002	1.927 ± 0.014	1.13 ± 0.08	22.5 ± 2.0	19.8 ± 1.4	⋯	0.45 ± 0.04
	2015 WF13	0.943 ± 0.001	1.984 ± 0.008	3.64 ± 0.13	⋯	44 ± 3	10 ± 1	⋯
	2015 XC	0.947 ± 0.006	1.947 ± 0.007	3.29 ± 0.10	⋯	36 ± 3	7 ± 1	⋯
	2016 BC14	0.942 ± 0.002	1.926 ± 0.026	1.40 ± 0.08	22.9 ± 2.0	20.1 ± 1.4	⋯	0.49 ± 0.04
	2016 CM194	0.937 ± 0.001	1.992 ± 0.008	1.30 ± 0.05	22.5 ± 2.0	19.8 ± 1.4	⋯	0.41 ± 0.04
	2016 CO247	⋯	⋯	⋯	⋯	⋯	⋯	⋯
	2016 EB1	⋯	⋯	⋯	⋯	⋯	⋯	⋯
	2016 EF28	0.949 ± 0.004	1.989 ± 0.008	3.54 ± 0.10	⋯	45 ± 3	10 ± 1	⋯
	2016 EV27	1.011 ± 0.003	1.940 ± 0.015	0.74 ± 0.05	30.4 ± 2.0	25.3 ± 1.4	⋯	0.58 ± 0.04
	2016 FV13	0.936 ± 0.005	1.970 ± 0.010	0.94 ± 0.07	21.8 ± 2.0	19.3 ± 1.4	⋯	0.55 ± 0.04
	2016 GU	0.910 ± 0.004	⋯	⋯	⋯	⋯	⋯	⋯
	2016 LG	0.989 ± 0.004	2.057 ± 0.011	0.41 ± 0.02	29.0 ± 2.0	24.4 ± 1.4	⋯	0.63 ± 0.04
	2017 BS5	0.992 ± 0.002	⋯	⋯	29.9 ± 2.0	24.9 ± 1.4	⋯	⋯
	2017 BW	⋯	⋯	⋯	⋯	⋯	⋯	⋯
	2017 BY93	0.951 ± 0.002	1.967 ± 0.011	0.58 ± 0.02	25.1 ± 2.0	21.6 ± 1.4	⋯	0.58 ± 0.04
	2017 CR32	⋯	⋯	⋯	⋯	⋯	⋯	⋯
	2017 DR34	0.930 ± 0.002	1.920 ± 0.018	0.81 ± 0.06	20.6 ± 2.0	18.5 ± 1.4	⋯	0.57 ± 0.04
	2017 FU64	⋯	⋯	⋯	⋯	⋯	⋯	⋯

Table 4
(Continued)

Number	Designation	BIC (μm)	BIIC (μm)	BAR	Fa (mol%)	Fs (mol%)	Wo (mol%)	ol/(ol+px)
	2017 OL1	0.953 ± 0.006	1.987 ± 0.007	0.63 ± 0.05	25.5 ± 2.0	21.9 ± 1.4	⋯	0.57 ± 0.04
	2017 OP68	0.932 ± 0.005	1.138 ± 0.010	⋯	⋯	⋯	⋯	⋯
	2017 RR15	0.933 ± 0.003	1.943 ± 0.006	1.73 ± 0.04	⋯	41 ± 3	9 ± 1	⋯
	2017 WX12	0.995 ± 0.010	2.044 ± 0.013	0.70 ± 0.03	30.1 ± 2.0	25.0 ± 1.4	⋯	0.55 ± 0.04
	2018 XG5	0.935 ± 0.004	1.956 ± 0.005	1.15 ± 0.06	22.1 ± 2.0	19.5 ± 1.4	⋯	0.44 ± 0.04
	2018 XS4	0.932 ± 0.001	1.987 ± 0.009	1.28 ± 0.04	21.5 ± 2.0	19.1 ± 1.4	⋯	0.41 ± 0.04
	2019 AN5	1.016 ± 0.008	2.050 ± 0.017	0.47 ± 0.03	30.7 ± 2.0	25.4 ± 1.4	⋯	0.61 ± 0.04
	2019 GT3	0.949 ± 0.002	1.958 ± 0.010	0.68 ± 0.02	24.8 ± 2.0	21.4 ± 1.4	⋯	0.56 ± 0.04
	2019 JL3	0.984 ± 0.006	1.998 ± 0.011	0.69 ± 0.02	29.3 ± 2.0	24.5 ± 1.4	⋯	0.55 ± 0.04
	2019 JX7	0.993 ± 0.002	2.047 ± 0.012	0.51 ± 0.03	29.9 ± 2.0	25.0 ± 1.4	⋯	0.60 ± 0.04
	2019 RC	⋯	⋯	⋯	⋯	⋯	⋯	⋯
	2019 SH6	0.978 ± 0.005	1.979 ± 0.024	0.71 ± 0.07	28.7 ± 2.0	24.1 ± 1.4	⋯	0.55 ± 0.04
	2019 UO13	0.970 ± 0.001	1.991 ± 0.005	0.92 ± 0.03	27.9 ± 2.0	23.5 ± 1.4	⋯	0.50 ± 0.04
	2019 YM3	0.969 ± 0.001	2.008 ± 0.009	0.41 ± 0.03	27.7 ± 2.0	23.4 ± 1.4	⋯	0.62 ± 0.04
	2020 DZ1	0.984 ± 0.004	⋯	⋯	29.3 ± 2.0	24.5 ± 1.4	⋯	⋯
	2020 HS6	0.959 ± 0.002	1.955 ± 0.006	0.48 ± 0.02	26.4 ± 2.0	22.5 ± 1.4	⋯	0.60 ± 0.04
	2020 KC5	0.961 ± 0.003	1.981 ± 0.007	0.64 ± 0.04	26.7 ± 2.0	22.7 ± 1.4	⋯	0.57 ± 0.04
	2020 RO6	0.943 ± 0.003	1.974 ± 0.008	2.18 ± 0.05	⋯	50 ± 3	12 ± 1	⋯
	2020 SN	0.891 ± 0.003	⋯	⋯	⋯	⋯	⋯	⋯
	2020 ST1	0.938 ± 0.001	1.998 ± 0.004	1.12 ± 0.05	22.7 ± 2.0	20.0 ± 1.4	⋯	0.45 ± 0.04
	2020 YQ3	0.993 ± 0.004	1.935 ± 0.012	0.66 ± 0.02	29.9 ± 2.0	25.0 ± 1.4	⋯	0.56 ± 0.04

Notes. The columns in this table are object number and designation; Band I center (BIC); Band II center (BIIC); BAR; molar contents of fayalite (Fa), ferrosilite (Fs), and wollastonite (Wo); and ol/(ol+px) ratio. The uncertainties for Fa, Fs, Wo, and the ol/(ol+px) ratio are from Burbine et al. (2009) and Sanchez et al. (2020).
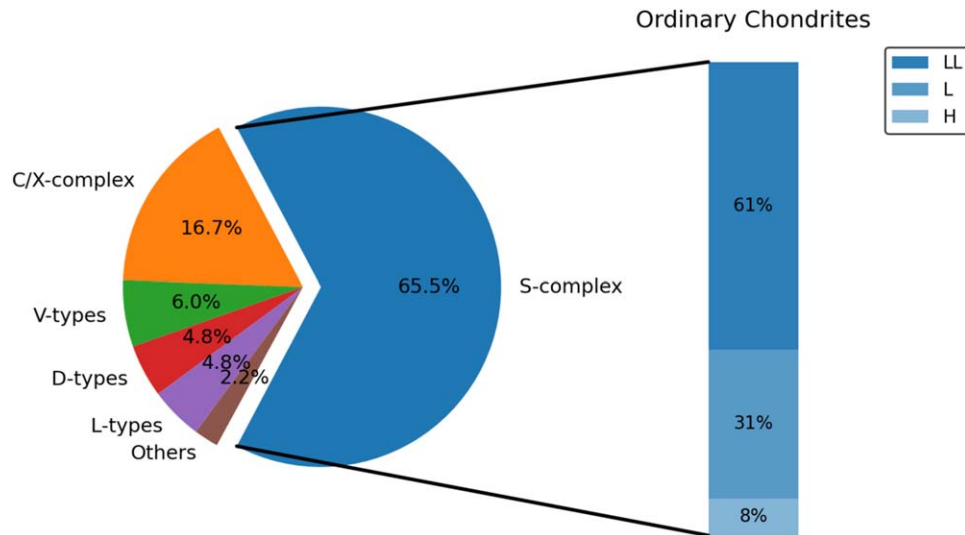
Figure 4. Approximate fractions of the main taxonomic types and ordinary chondrites. In this figure, asteroids in the S-complex include Q-types and a new subclass of objects introduced in the present study called Sx-types. Asteroids in the C/X-complex include those with ambiguous C- or X-complex classification plus asteroids classified as Xk-, Xn-, and B-types. The fraction corresponding to "others" includes K-types and objects whose taxonomic classification is indeterminate.

The spectra of 2002 LY1, 2006 XY, 2014 WN4, and 2016 CO247 are featureless, with relatively neutral spectral slopes, and do not show signs of a thermal excess at wavelengths $>2\,\mu$m. The spectrum of a dark NEO that is close to its perihelion would typically display a thermal tail. However, sometimes, if the object is faint, this thermal tail could be difficult to detect. Thus, for these four NEOs, we cannot rule out a carbonaceous-chondrite-like composition. Another alternative that could explain their spectral characteristics is the presence of iron-free enstatite. The NIR spectra of some enstatite chondrites and achondrites (aubrites), which have a

high content of this mineral, are featureless and can have neutral or negative slopes depending on the grain size (e.g., Vernazza et al. 2009; Reddy et al. 2016). Therefore, a composition dominated by iron-free enstatite could also be compatible with the spectral characteristics of these asteroids. For 2006 XY and 2014 WN4, we found a good spectral match with the CM2 carbonaceous chondrite Murchison and the aubrite Khor Temiki, respectively (Figure 11).

Only one of the NEOs classified as C/X-complex, 2017 OP68, shows weak features in the NIR, with one possible absorption band centered at $0.932 \pm 0.005\,\mu$m and another at
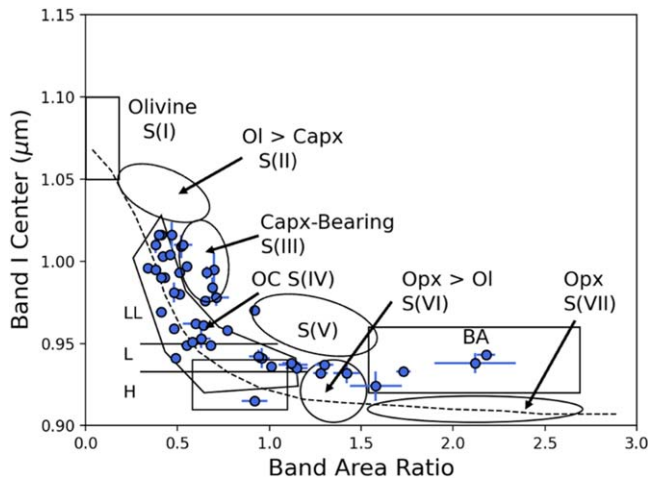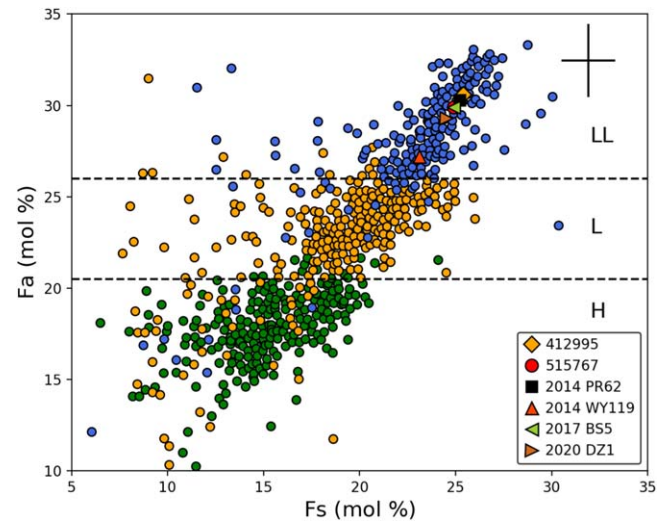
Figure 5. Band I center vs. BAR from Gaffey et al. (1993) for NEOs whose spectra exhibit absorption bands centered at ~1 and 2 μm due to the presence of olivine and pyroxene. The polygonal region corresponds to the S(IV) subtype associated with ordinary chondrites (OC). The horizontal lines represent the approximate boundaries for ordinary chondrites found by Sanchez et al. (2020). The rectangular zone overlapping the S(IV) subtype represents the spectral zone for acapulcoite–lodranite clan meteorites found by Lucas et al. (2019). The rectangular zone (BA) includes the pyroxene-dominated basaltic achondrite assemblages (Gaffey et al. 1993). The dashed curve indicates the location of the olivine–orthopyroxene mixing line (Cloutis et al. 1986).

Figure 7. Molar content of fayalite (Fa) vs. ferrosilite (Fs) for NEOs with an ordinary chondrite-like composition whose spectra do not show the 2 μm band. Measured values for H- (green), L- (orange), and LL- (blue) ordinary chondrites from Nakamura et al. (2011) are also included. The error bars correspond to the uncertainties derived by Sanchez et al. (2020), 2.0 mol% for Fa and 1.4 mol% for Fs. Figure adapted from Nakamura et al. (2011).

Figure 6. Molar contents of fayalite (Fa) and ferrosilite (Fs) and ol/(ol+px) ratio for NEOs with an ordinary chondrite-like composition (red squares). The synthetic data set corresponding to the three ordinary chondrite subtypes (H, L, LL) created to train the machine-learning classifier is also shown. The error bars correspond to the uncertainties derived by Sanchez et al. (2020), 2.0 mol% for Fa, 1.4 mol% for Fs, and 0.04 for the ol/(ol+px) ratio.

Figure 8. Normalized confusion matrix resulting from the multinomial logistic regression model. Labels correspond to the three ordinary chondrite subtypes (H, L, LL).

1.138 ± 0.010 μm. The spectra of carbonaceous chondrites that have undergone aqueous alteration exhibit absorption bands due to the presence of phyllosilicates such as the serpentine and the saponite groups (Cloutis et al. 2012). The serpentine group shows absorption bands at ~0.90–0.94 μm and ~1.1–1.2 μm, whereas the saponite group is at ~0.90 μm and ~1.1–1.2 μm (Cloutis et al. 2011, 2012). These particular absorption bands are caused by an octahedral Fe^{2+} crystal field transition. Given the position of the absorption bands of 2017 OP68, both phyllosilicates could be present, although the serpentine group

might be dominant. Possible meteorite analogs for this NEO include CM and CI carbonaceous chondrites.

The NEO 163348 was the only object classified as a B-type. Asteroids belonging to this taxonomic type have spectra that can exhibit either negative or positive NIR slopes (e.g., de León et al. 2012) and have a mean geometric albedo of $0.09^{+0.05}_{-0.04}$ (Marsset et al. 2022). The NIR spectrum of 163348 is featureless; it has a slightly negative slope and shows a thermal excess at wavelengths >2 μm. These spectral characteristics are similar to some B-types, although the albedo derived for this object (0.015) is more consistent with the mean value estimated for P-type asteroids (Thomas et al. 2011; Marsset et al. 2022). Cantillo et al. (2023) studied grain-size effects on the spectra of carbonaceous chondrites and found
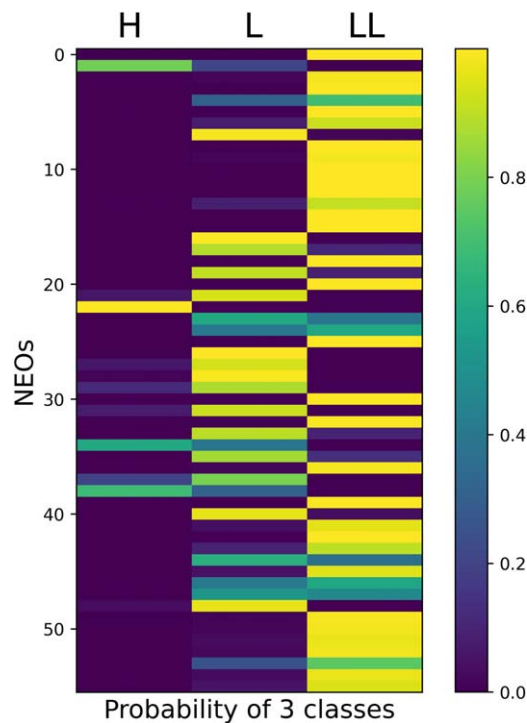
Figure 9. Probability of NEOs belonging to the three ordinary chondrite subtypes (H, L, LL). Each row represents an NEO, and each column represents an ordinary chondrite subtype.

that grains >150 μm could, in some cases, turn a Ch-type object into a B-type. Thus, it is also possible that 163348 is being classified as a B-type due to larger grains on the surface. The spectral match with meteorite Mighei (Figure 11) along with the low albedo suggest that carbonaceous chondrites could be good meteorite analogs for this asteroid.

2.4.5. Xk- and Xn-type Asteroids

The NIR spectra of Xk- and Xn-types show weak absorption bands and no thermal excess, which allows us to separate them from the broader C/X-complex category for the compositional analysis. NEOs classified as Xk-types include 85990, 2015 BC, and 2020 SN. The spectra of 85990 and 2015 BC show red spectral slopes and weak absorption bands at ~0.93 μm and ~2.0 μm due to the presence of pyroxene. Since both NEOs are also located in the basaltic achondrites region (Figure 5), the compositional analysis was done following the same procedure used with the V-types. We found that the pyroxene chemistry of 85990 is consistent with noncumulate eucrites, whereas 2015 BC is more similar to howardites (Figure 10). It is important to note that given the relatively weak absorption bands of these objects, pyroxene is likely not the main mineral present on the surface. For example, some asteroids with similar spectral characteristics have been found to have a high metal content on their surface based on their radar albedos (e.g., Hardersen et al. 2011; Neeley et al. 2014; Sanchez et al. 2021). Thus, possible meteorite analogs could also include silicate-bearing NiFe meteorites, stony-iron meteorites, and metal-rich carbonaceous chondrites.

The NIR spectrum of 2020 SN has a curved downward shape and a weak absorption band centered at ~0.89 μm. The spectra of HEDs typically have Band I centers in the range of
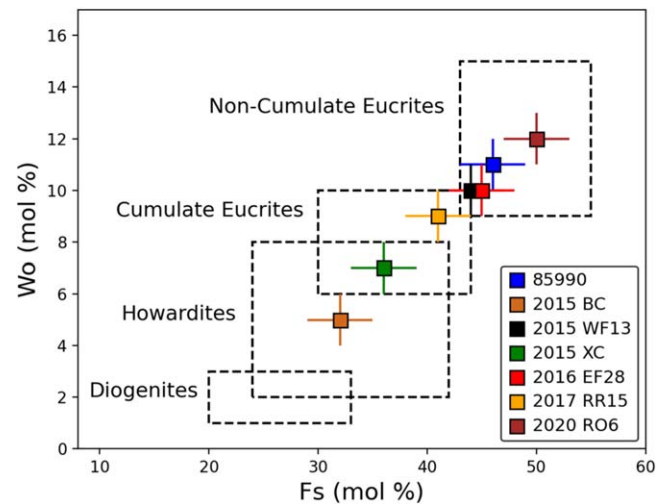
Figure 10. Molar contents of wollastonite (Wo) vs. ferrosilite (Fs) for NEOs 85990, 2015 BC, 2015 WF13, 2015 XC, 2016 EF28, 2017 RR15, and 2020 RO6. The error bars correspond to the values determined by Burbine et al. (2009), 3 mol% for Fs and 1 mol% for Wo. The approximate range of pyroxene chemistries for howardites, noncumulate eucrites, cumulate eucrites, and diogenites from Sanchez et al. (2013) are indicated as dashed boxes.

~0.92–0.95 μm, making the spectral calibrations derived by Burbine et al. (2009) not suitable for the compositional analysis of this asteroid. Nevertheless, the position of the band center suggests the presence of Fe-poor pyroxene on the surface of 2020 SN. Enstatite chondrites or aubrites containing traces of Fe^{2+} are possible meteorite analogs for this asteroid.

The Xn class was not originally included in the Bus–DeMeo taxonomy but was introduced by Binzel et al. (2019) to classify a small number of NEOs whose spectra are relatively flat and show a narrow feature centered at ~0.9 μm. NEOs in our sample that were classified as Xn include 2015 TC25 and 2016 GU.

The physical and compositional properties of 2015 TC25 have already been studied in great detail by Reddy et al. (2016). The NIR spectrum of this object shows a negative slope and a narrow absorption band centered at ~0.91 μm. Based on its high geometric albedo and spectral characteristics, Reddy et al. (2016) determined that 2015 TC25 was a "Nysa-like" E-type asteroid. They also found that the spectrum of this NEO could be reproduced with a mixture of 7% orthopyroxene and 93% aubrite.

The spectrum of 2016 GU has a neutral spectral slope and a weak and narrow absorption band centered at 0.91 μm. Like in the case of 2020 SN, we did not use the equations of Burbine et al. (2009) for the analysis of this asteroid, as its Band I center is below the typical range measured for HEDs. The position of the Band I center, however, suggests the presence of Fe-poor pyroxene on the surface. Because this object does not have a red spectral slope, silicate-bearing NiFe meteorites are probably not good meteorite analogs. Instead, this NEO could be more similar to enstatite chondrites or aubrites containing traces of Fe^{2+}.

2.4.6. D-type Asteroids

NEOs that were classified as D-types include 2012 ER14, 2015 AP43, 2019 RC, and 2017 FU64. All these objects have featureless spectra with very steep slopes. The spectra of 2015 AP43 and 2017 FU64 also show a thermal excess, which allowed us to estimate albedos of 0.05 and 0.02, respectively, for these objects. These values are within the range found for
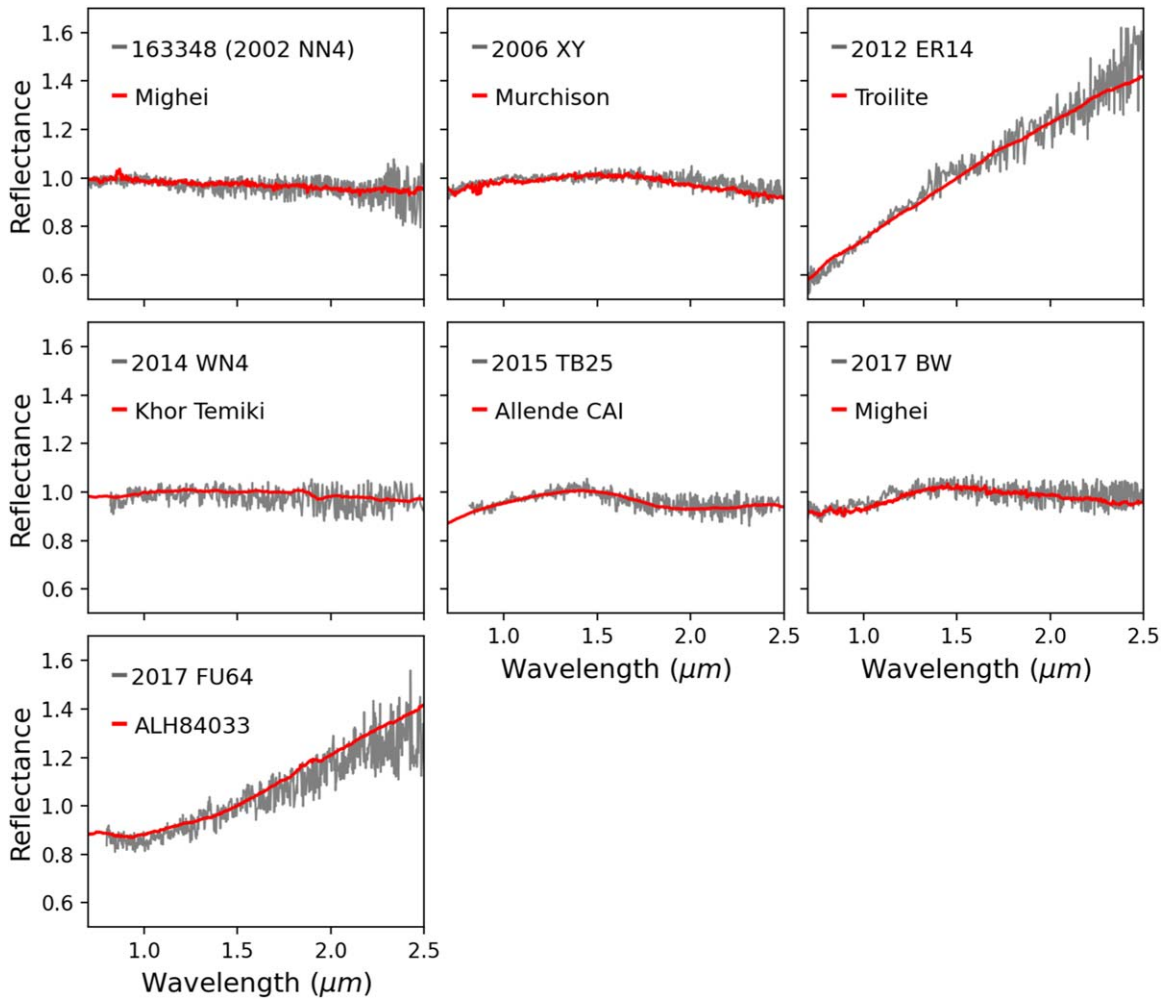
Figure 11. NIR spectra of NEOs 163348, 2006 XY, 2012 ER14, 2014 WN4, 2015 TB25, 2017 BW, and 2017 FU64. Also shown are the spectra of the CM2 carbonaceous chondrite Mighei (RELAB sample IDs cmms01 and ccms01), the CM2 carbonaceous chondrite Murchison (RELAB sample ID cnms02), troilite from the Canyon Diablo iron meteorite (RELAB sample ID cae01), the enstatite achondrite (aubrite) Khor Temiki (RELAB sample ID latb48), CAIs from Allende (RELAB sample ID c1tm05), and the CM2 carbonaceous chondrite ALH84033 (RELAB sample ID c1mp14).

D-type asteroids (∼0.02–0.07) by previous studies (Thomas et al. 2011; Marsset et al. 2022). DeMeo et al. (2022) noticed that a large percentage of D-type asteroids matched the spectra of iron meteorites. We obtained similar results when we looked for meteorite analogs for these NEOs. Figure 11 shows an example of such a spectral match, in this case between 2012 ER14 and troilite from the Canyon Diablo iron meteorite. This is somehow expected, as the spectra of iron meteorites share the main characteristics of D-types, i.e., very steep slopes and a lack of absorption features. Despite the good spectral match between the D-types and the iron meteorites, these asteroids, in general, are considered to be primitive bodies and have been associated with carbonaceous chondrites such as the Tagish Lake meteorite (e.g., Hiroi et al. 2001; Barucci et al. 2018; Gartrelle et al. 2021). In the case of 2015 AP43 and 2017 FU64, their low albedos are consistent with a carbonaceous-chondrite-like composition. For 2017 FU64, we found a good spectral match with the CM2 carbonaceous chondrite ALH84033 (Figure 11). The spectra of 2012 ER14 and 2019 RC did not show a thermal tail, but, as discussed earlier, a thermal tail can be difficult to detect in faint objects. As a result, it is also possible that these two NEOs are primitive bodies.

2.4.7. K-, L-, and Indeterminate Asteroids

The only NEO in our sample that was classified as a K-type is 2014 PR62. The NIR spectrum of this object shows an absorption band centered at ∼1 μm and no signs of a 2 μm band. Given the scattering in the data at wavelengths >1.5 μm, it is not clear if the 2 μm band is really absent or too weak to be detected. The compositional analysis of 2014 PR62 was done using the Band I center and the equations of Sanchez et al. (2020; see Section 2.4.1). The asteroid was found to have olivine and pyroxene chemistries similar to LL-chondrites (Figure 7). Some K-type asteroids in the main belt, e.g., 221 Eos and members of its family, have been linked to CO-, CV-, CK-, and R-chondrites (Doressoundiram et al. 1998; Burbine et al. 2001; Mothé-Diniz et al. 2008). We were not able to find a good meteorite analog for 2014 PR62 based on curve matching; however, considering its spectral characteristics, an affinity with any of those meteorites could be possible.

Four NEOs were classified as L-types, including 2014 VH2, 2015 TB25, 2017 BW, and 2017 CR32. Previous works have found that some carbonaceous chondrites and calcium-aluminum-rich inclusions (CAIs) share similar spectral characteristics with L-type asteroids (Burbine et al. 1992; Sunshine et al. 2008; Devogèle et al. 2018). The spectra of the four

NEOs show an increase in reflectance with increasing wavelengths from ~0.75 to 1.5 μm and then become relatively flat at longer wavelengths. For 2014 VH2, we did not find a good spectral match with meteorite samples, but given its taxonomic classification, possible meteorite analogs could include carbonaceous chondrites. The NIR spectrum of 2015 TB25 shows a slightly negative slope at wavelengths >1.5 μm and the possible presence of a 2 μm band. For this NEO, we found a good spectral match with CAIs from the CV3 carbonaceous chondrite Allende (Figure 11). The spectrum of the CAI exhibits a characteristic absorption band centered at ~2 μm due to the presence of spinel ($MgAl_2O_4$). For asteroid 2017 BW, the best meteorite analog was found to be the CM2 carbonaceous chondrite Mighei. No good meteorite analogs were found for 2017 CR32; however, as in the previous cases, a link with carbonaceous chondrites could be possible.

There was one asteroid (2015 FL) whose NIR spectrum did not match any of the spectra in the Bus–DeMeo taxonomy; therefore, its classification was labeled as "indeterminate." The spectrum of this asteroid shows a very red slope (comparable to a D-type) from ~0.7 to 1.4 μm and then becomes flat at longer wavelengths. No absorption bands are visible, but given the scattering of the data beyond 1.4 μm, we cannot rule out the presence of the 2 μm band. No good meteorite analogs were found for this NEO.

2.5. Space Weathering and Resurfacing Processes

Space weathering refers to any process that modifies the optical properties and physical structure of the surface of airless bodies. It is characterized by producing an increase of the spectral slope and suppression of the absorption bands in the NIR spectra of S-complex objects (e.g., Pieters et al. 2000; Hapke 2001; Clark et al. 2002; Gaffey 2010). For asteroids in the S-complex, S-, Sq-, and Q-types are thought to represent a weathering gradient, with Q-types having relatively fresh surfaces and Sq- and S-types having more space-weathered surfaces (e.g., Binzel et al. 2010, 2019).

Different processes have been proposed to explain the presence of fresh material on the surface of asteroids, including thermal fatigue fragmentation, YORP spin-up, and planetary encounters. Thermal fragmentation caused by diurnal temperature variations can create fresh regolith by breaking down rocks and exposing their unweathered interiors (Delbo et al. 2014). YORP spin-up, on the other hand, can accelerate the rotation of an asteroid enough to displace weathered particles, refreshing with this the surface of the object (e.g., Graves et al. 2018). Similarly, tidal stress caused during close encounters with planets can produce landslides exposing fresh subsurface material (e.g., Binzel et al. 2010, 2019; Nesvorný et al. 2010).

Binzel et al. (2019) investigated the efficiency of the different resurfacing processes as a function of the perihelion distance. For this, they estimated the degree of space weathering experienced by the NEOs by calculating the space-weathering parameter $\Delta\eta$, which uses the principal components PC1′ and PC2′ obtained from the taxonomic classification. This parameter is given by the scalar magnitude of the space-weathering vector defined in the principal component space of the Bus–DeMeo taxonomy (Binzel et al. 2010, 2019):

$$\Delta\eta = \frac{-\frac{1}{3}PC2' + PC1' + 0.5}{1.0541}. \tag{4}$$
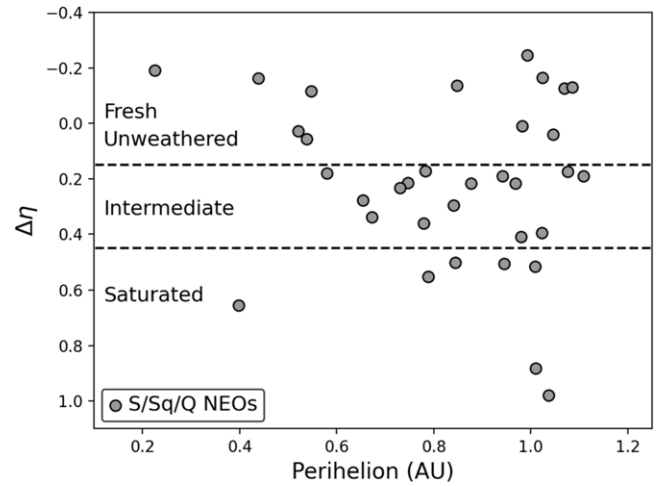
Figure 12. Space-weathering parameter $\Delta\eta$ as a function of the perihelion distance for S-, Sq-, and Q-types. Regions corresponding to the different regimes of space weathering (fresh, intermediate, and saturated) from Binzel et al. (2019) are indicated. Figure adapted from Binzel et al. (2019).

The analysis done by Binzel et al. (2019) showed that the number of NEOs with fresh unweathered surfaces increases as the perihelion distance decreases. This is because at short perihelion distances, there are more resurfacing processes operating simultaneously. At perihelion distances <1.0 au, thermal fragmentation, YORP spin-up and planetary encounters with the Earth and Venus are all acting together, whereas at greater perihelion distances, YORP spin-up, and encounters with Mars are the most dominant.

We performed a similar analysis for the S-, Sq-, and Q-types in our sample. Spectra obtained with the 0.8 μm dichroic were not included. Figure 12 shows $\Delta\eta$ as a function of the perihelion distance for the NEOs. Most objects were found to fall within the fresh or intermediate regimes as defined by Binzel et al. (2019), and only a few fall in the saturated regime. In the context of space weathering, saturation occurs when surface grains become uniformly weathered after multiple rearrangement events followed by extended periods of exposure to the space environment (Binzel et al. 2019).

The trend in Figure 12 is less clear than what was found by Binzel et al. (2019); this is probably because the maximum perihelion distance of the NEOs in our analysis is ~1.1 au, whereas the data used by Binzel et al. (2019) include objects with perihelion distances that extend up to ~1.7 au. Nevertheless, we note that most of the NEOs that fall in the saturated regime have perihelion distances >0.8 au, which is consistent with the results of Binzel et al. (2019).

Hasegawa et al. (2019) found that surface refreshening due to close encounters with planets could explain only ~50% of known Q-types. To account for the other Q-types, they proposed an alternative explanation, where these objects have weathered surfaces like S-types but their spectral characteristics are explained by the presence of large particles (>100 μm). Different mechanisms have been proposed to explain the release of particles smaller than 100 μm, a condition required for this hypothesis to work. These include solar radiation pressure and electrostatic acceleration (Hasegawa et al. 2019).

We tested this hypothesis by comparing $\Delta\eta$ values obtained for different grain sizes of the LL-chondrite Chelyabinsk with the $\Delta\eta$ of asteroid 25143 Itokawa. The $\Delta\eta$ values of
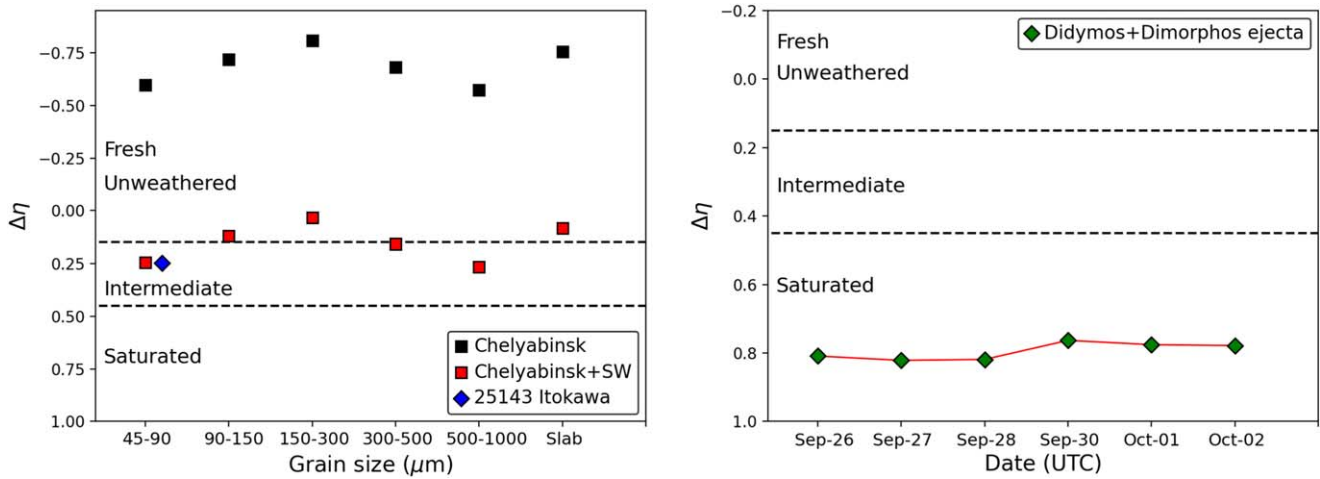
Figure 13. Left: space-weathering parameter $\Delta\eta$ vs. grain size for the LL-chondrite Chelyabinsk. Black squares represent the $\Delta\eta$ values calculated for different grain sizes of Chelyabinsk obtained by Bowen et al. (2023). Red squares represent the $\Delta\eta$ values of Chelyabinsk plus space weathering (SW) after being offset to match the $\Delta\eta$ calculated for asteroid Itokawa (blue diamond) from the spectrum obtained by Binzel et al. (2001). Right: space-weathering parameter $\Delta\eta$ vs. date for the Didymos system. $\Delta\eta$ has been calculated from the PC values reported by Polishook et al. (2023). The location in the x-axis of the Didymos system corresponds to the observation dates carried out before (September 26) and after (September 27–October 2) the impact of the DART mission. For both figures, regions corresponding to the different regimes of space weathering (fresh, intermediate, and saturated) from Binzel et al. (2019) are indicated.

Chelyabinsk were calculated from the spectra of samples with five different grain sizes (45–90, 90–150, 150–300, 300–500, and 500–1000 μm) obtained by Bowen et al. (2023) plus the spectrum of a slab obtained for this study. These values are depicted as black squares in Figure 13 (left). The $\Delta\eta$ for Itokawa was calculated from the spectrum obtained by Binzel et al. (2001). Abe et al. (2006) found that the average reflectance spectra of Itokawa were consistent with grain sizes of <125 μm. Therefore, we matched the location of Itokawa in the x-axis with the 45–90 μm sample, since this grain size is probably the one that best represents the mean grain size of the asteroid. Then, we offset all the $\Delta\eta$ values calculated for Chelyabinsk (red squares in Figure 13), so that the $\Delta\eta$ corresponding to the 45–90 μm sample overlaps with the $\Delta\eta$ of Itokawa. In this way, we can visualize what would happen to the space-weathering parameter of Itokawa if we increase the grain size.

As can be seen in Figure 13 (left), increasing the grain size from 45–90 to 150–300 μm could, in theory, move Itokawa from the intermediate to the fresh (unweathered) regime. A similar result would be obtained if the surface of Itokawa were completely depleted of dust (slab), which is probably the case for very small asteroids of just a few meters in size (e.g., Reddy et al. 2016). Interestingly, if the grain size were in the range of ∼500–1000 μm, no change in $\Delta\eta$ would be seen compared to the 45–90 μm sample.

Our results seem to confirm the findings of Hasegawa et al. (2019) but also impose an upper limit in the grain size for this mechanism to be effective. For the Chelyabinsk sample shown in Figure 13, this upper limit is ∼400 μm; for other meteorites with different compositions, this limit might change. This constraint in grain size for which we see a meaningful increase of $\Delta\eta$ is related to the way light is absorbed within the grains. To illustrate this, it is useful to see how the Chelyabinsk spectra change as the grain size increases. Figure 14 (left) shows the spectra corresponding to five different grain sizes plus a slab. The most noticeable change is an overall decrease in the spectral slope with increasing grain size, being particularly pronounced for the slab. Band depths, which were measured from the continuum to the band center (e.g., Sanchez et al. 2012),

show an increase from the 45–90 μm to the 150–300 μm sample and then a decrease for larger grain sizes (Figure 14, right). The initial increase in band depths happens because as the grain size increases, so does the mean optical path length, resulting in more absorption within the grain and deeper absorption bands (e.g., Pieters 1983). However, after reaching a maximum in band depth at a grain size of ∼225 μm, band saturation starts to occur (i.e., all photons that are not scattered are absorbed within the grains), and the absorption bands become shallower. Because $\Delta\eta$ is calculated from PC1′ and PC2′, which are sensitive to the intensity of the absorption bands, this parameter will closely follow the behavior of the band depths. It is important to note that composition also plays a role and that the pattern that we observe for the ordinary chondrite is probably not going to be the same for a meteorite with a different composition.

The obvious consequence of these results is that there will be some cases where the increase in grain size is too small (or too large) to produce a change in the perceived degree of space weathering of the asteroid. An example of such a case could be the Didymos system, the target of NASA's Double Asteroid Redirection Test (DART) mission. Polishook et al. (2023) obtained NIR spectra of Didymos before and after the impact. They found that the ejecta cloud released from Dimorphos was the main contributor to the light of the system for ∼40 hr after the impact. During those hours, a decrease in spectral slope was observed, and, as the ejecta cloud dispersed, the spectral slope returned to the preimpact level. However, no significant change in the absorption bands that could turn this S-type asteroid into a "fresh" Q-type was detected. This led to the conclusion that a negligible amount of unweathered material was ejected from Dimorphos and that the ejecta cloud was dominated by coarse debris ⩾100 μm (Polishook et al. 2023).

We calculated the $\Delta\eta$ values for the Didymos system from the PC1′ and PC2′ values reported by Polishook et al. (2023). As shown in Figure 13 (right), there is little change in $\Delta\eta$ from September 26 to 28, and only a small decrease occurs for the following nights. This is consistent with the lack of unweathered material reported by Polishook et al. (2023). Moreover, the small variation in $\Delta\eta$ combined with the
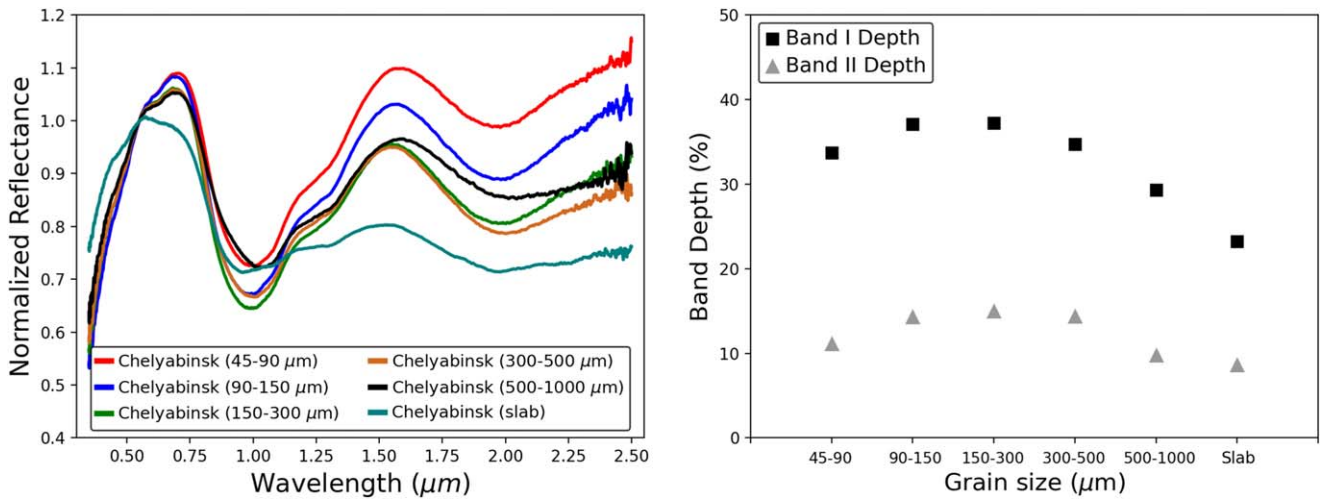
Figure 14. Left: spectra of the LL-chondrite Chelyabinsk corresponding to five different grain sizes plus a slab from Bowen et al. (2023). All spectra are normalized to unity at 0.55 μm. Right: Band I and II depths as a function of grain size measured from the Chelyabinsk spectra. Uncertainties are smaller than the symbols.
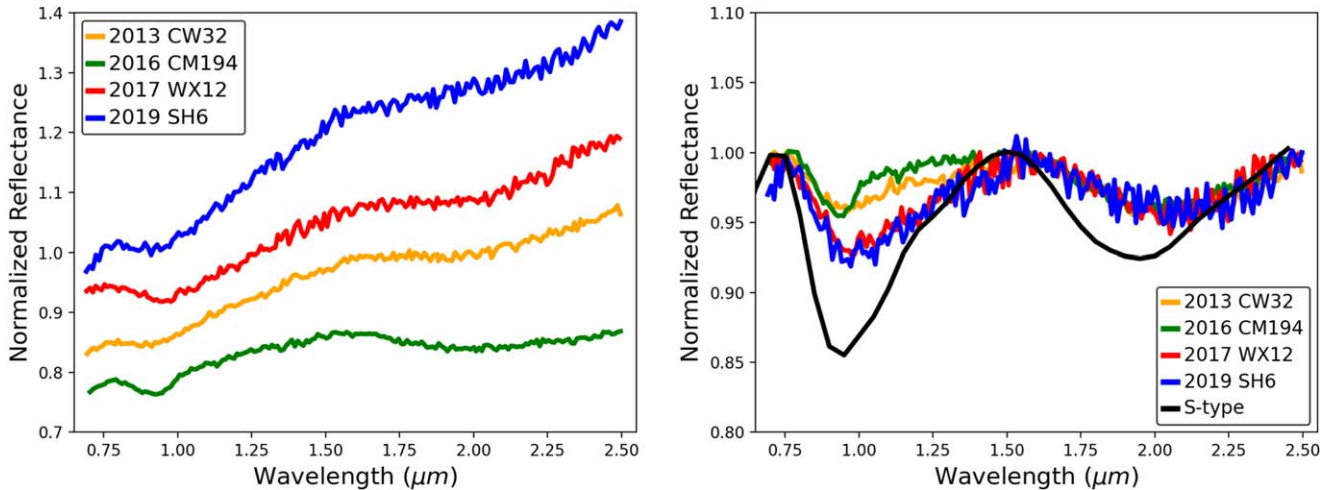
Figure 15. Left: spectra of NEOs 2013 CW32, 2016 CM194, 2017 WX12, and 2019 SH6. All the spectra show absorption bands centered at ~0.9 and 2.0 μm due to the minerals olivine and pyroxene. Spectra have been offset for clarity. Right: continuum-removed spectra of the same objects. The mean spectrum of an S-type from DeMeo et al. (2009) is also shown.

decrease in spectral slope suggests two possibilities: (1) the increase in grain size was small compared with the grains present before the impact, or (2) the increase in grain size was large enough to start to produce band saturation. This example also highlights the fact that an asteroid that is well inside the saturated region (S-type) is unlikely to reach the intermediate (Sq-type) or unweathered (Q-type) regions even if the grain size increases to the point where $\Delta\eta$ reaches its lowest value.

2.6. Possible Evidence of Metal or Shock Darkening

When the results obtained from the taxonomic classification and the compositional analysis are combined, it is possible to obtain further insights about particular characteristics of the NEOs. This is the case for the Sx-type objects, whose weak absorption bands could lead to an ambiguous classification in the C- or X-complex, even though their composition is similar to ordinary chondrites. In this section, we investigate the possible causes behind these results.

As a reminder, four NEOs were found to share these characteristics: 2013 CW32, 2016 CM194, 2017 WX12, and 2019 SH6. The spectra of these objects are shown together in

Figure 15 (left). At first glance, the spectral characteristics of these NEOs are typical of S-type asteroids showing absorption bands centered at ~0.9 and 2.0 μm due to the presence of olivine and pyroxene. However, compared to the mean spectrum of an S-type, their absorption bands are much weaker (Figure 15, right).

NEO 2013 CW32 was found to have an L-chondrite-like composition. Its NIR spectrum shows a red spectral slope with a Band I depth of $4.1\% \pm 0.1\%$ and a Band II depth of $3.1\% \pm 0.1\%$. For comparison, the mean spectrum of an S-type asteroid from DeMeo et al. (2009) has a Band I depth of $13.0\% \pm 0.2\%$ and a Band II depth of $5.5\% \pm 0.1\%$. The composition of 2016 CM194 was also found to be similar to L-chondrites, although an affinity with primitive achondrites is also possible. This object has the less steep spectral slope of the four NEOs. The Band I depth is $4.4\% \pm 0.1\%$, and the Band II depth is $2.6\% \pm 0.1\%$. 2017 WX12, on the other hand, has a composition consistent with LL-chondrites. The spectrum of this asteroid has a red spectral slope with a Band I depth of $7.6\% \pm 0.1\%$ and a Band II depth of $4.8\% \pm 0.6\%$. Similarly, the composition of 2019 SH6 is also consistent with LL-
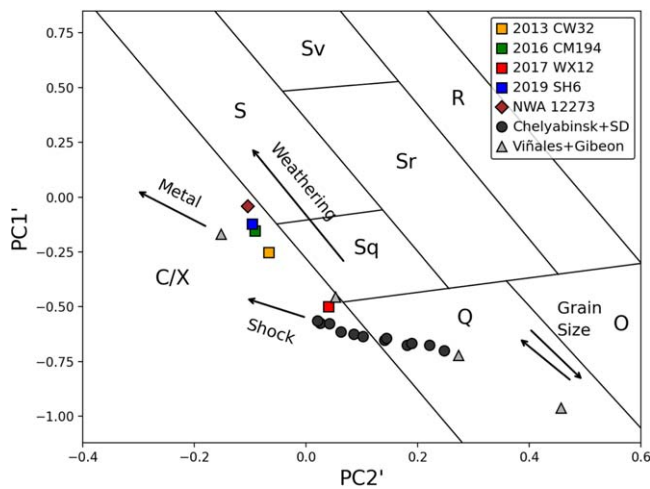
Figure 16. PC2′ vs. PC1′ diagram from DeMeo et al. (2009). PC values calculated for 2013 CW32, 2016 CM194, 2017 WX12, 2019 SH6, and the metal-rich chondrite NWA 12273 (Reddy et al. 2019) are depicted with different colors. PC values for intimate mixtures of the L-chondrite Viñales and the iron meteorite Gibeon and intimate mixtures of Chelyabinsk and shock-darkened (SD) material from (Reddy et al. 2014) are also shown. Arrows indicate the direction in which the grain size or the content of metal and shock darkening increases. The first data point for the mixture of Viñales and Gibeon (lower right corner) corresponds to a mixture of 40 wt% Gibeon and 60 wt% Viñales. The following data points represent increments of 20 wt% Gibeon. The space-weathering vector from Binzel et al. (2019) is also indicated.

chondrites. The spectral slope of this NEO is the steepest of the four objects discussed in this section. The spectrum has a Band I depth of $7.8\% \pm 0.2\%$, and the Band II depth is $3.8\% \pm 0.5\%$.

In the Bus–DeMeo taxonomy, the PC1′ and PC2′ values are sensitive to the presence and intensity of the absorption bands. As a result, as the absorption bands become shallower, PC2′ moves toward negative values and PC1′ toward positive values, eventually crossing the line α, which separates the C/X-complex, whose spectra are relatively featureless, from other taxonomic types such as those in the S-complex and V-types. The PC1′ and PC2′ values for the four NEOs are shown in Figure 16. Several factors are known to produce changes in the band depths; among them, the most relevant are space weathering, grain size, phase reddening, and the presence of metal and shock darkening.

As explained in the previous section, space weathering produces suppression of the absorption bands. As the degree of space weathering increases, an asteroid with an ordinary chondrite-like composition will move from the Q-type to the S-type taxonomy. In the PC2′ versus PC1′ diagram, this transition is represented by a space-weathering vector that moves parallel to the line α but does not cross it (Figure 16). This suggests that space weathering alone is not responsible for the weak absorption bands of these asteroids.

As we have already seen, grain-size variations can produce changes in the intensity of the absorption bands and the spectral slope. Bowen et al. (2023) studied the effects of grain size on spectral band parameters, composition, and taxonomic classification. For this, they analyzed the spectra of ordinary chondrites for five different grain-size groups (45–90, 90–150, 150–300, 300–500, and 500–1000 μm). In the PC2′ versus PC1′ diagram, most samples were found to move away from the line α for grain-size groups 45–90 to 150–300 μm, but then for the largest grain sizes, 300–500 and 500–1000 μm, the opposite behavior was observed, and the PC values ended up

close to where they started (Figure 16). This behavior is explained by the saturation in the large grains previously discussed. Considering this, it seems unlikely that grain size is primarily responsible for the attenuation of the absorption bands observed in the NEOs.

Phase reddening produces an increase of the spectral slope and variations in the band depths as the phase angle increases (Sanchez et al. 2012). This effect is particularly relevant for NEOs, since they are normally observed at high phase angles. Sanchez et al. (2012) analyzed NIR spectra of S-complex NEOs and ordinary chondrites obtained at different phase angles. They found that the increase in spectral slope starts to become evident at phase angles $>30°$, and absorptions bands become deeper, reaching a maximum depth at phase angles of $\sim60°$. Many of the NEOs in this study were observed at phase angles $>30°$ and thus are likely affected by phase reddening. However, we note that while phase reddening can explain, at least in part, the red spectral slopes of some of the NEOs, the increase in band depths produced by phase reddening is inconsistent with the attenuation of the absorption bands of the NEOs discussed in this section.

The presence of metal can also suppress absorption bands. Radar observations have identified metal on the surface of many asteroids (e.g., Ostro et al. 1991; Shepard et al. 2010, 2015). The NIR spectra of these objects typically show red slopes and, in some cases, weak absorption bands at ~0.9 and 1.9 μm (e.g., Ockert-Bell et al. 2010; Hardersen et al. 2011; Neeley et al. 2014; Sanchez et al. 2017, 2021; Reddy et al. 2019). Samples from these bodies are likely represented by several classes of meteorites found on Earth, including iron meteorites, stony-iron meteorites such as pallasites and mesosiderites, metal-rich carbonaceous chondrites, and anomalous metal-rich chondrites.

Evidence of metal-rich chondrites with affinity to ordinary chondrites has been recently found in meteorites NWA 12273 and NWA 12379 (e.g., Agee et al. 2019; Jansen et al. 2019). NWA 12273 is made up of $\sim64\%$ Fe–Ni metal and $\sim30\%$ chondrules (Agee et al. 2019). The olivine chemistry is consistent with L3/LL3-chondrites, whereas the low-Ca pyroxene is more consistent with H4-chondrites. An NIR spectrum of NWA 12273 obtained by Reddy et al. (2019) shows a red spectral slope and two weak absorption features at ~0.9 and 2 μm due to the minerals olivine and pyroxene. NWA 12379 shares similar characteristics; it is made up of ~70 vol.% Fe–Ni metal and ~25 vol.% porphyritic ferromagnesian chondrules (Jansen et al. 2019). The oxygen isotopic composition and mineralogical characteristics of this meteorite were found to be similar to those of L3.8 ordinary chondrites (Jansen et al. 2019). According to Jansen et al. (2019), NWA 12379 could have formed by a collision between an ordinary-chondrite-like body and a metal-rich body.

In order to investigate the effects of metal content on ordinary chondrites, we prepared intimate mixtures of the L-chondrite Viñales and the iron meteorite Gibeon. Viñales was crushed using an alumina mortar and pestle and sieved to a grain size of 45–90 μm. Metal shavings of Gibeon were sieved to a grain size of $<300\,\mu$m. Four mixtures were prepared starting with a metal content of 20 wt% and increasing in 20 wt% metal intervals. A sample of 100 wt% Gibeon was also prepared. The visible and NIR spectra (0.35–2.5 μm) of the samples were obtained relative to a Labsphere Spectralon disk using an ASD Labspec4 Pro spectrometer at an incident angle
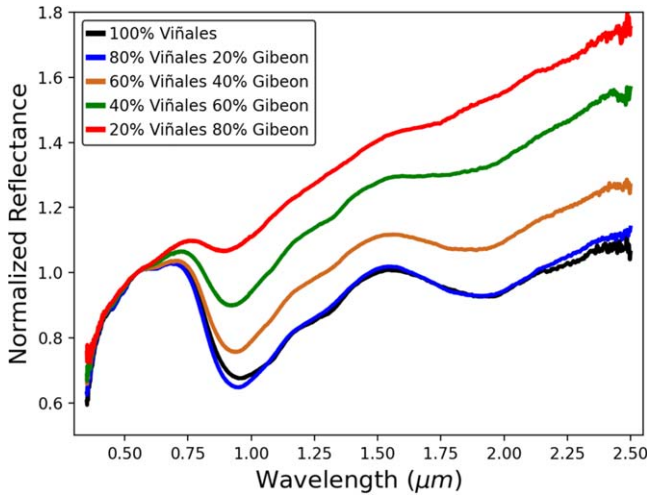
Figure 17. Spectra of intimate mixtures of the L-chondrite Viñales and the iron meteorite Gibeon. All spectra are normalized to unity at 0.55.

$i = 0°$ and emission angle $e = 30°$ (Figure 17). The Bus–DeMeo taxonomic classification was then applied to the spectra; the results are shown in Figure 16. The first data point, which falls in the Q-type region, corresponds to a mixture of 40 wt% Gibeon and 60 wt% Viñales; the last data point corresponds to the sample of 100 wt% Gibeon. We found that increasing the metal content would cause an object classified as Q-type to progressively move up and to the left in the PC2′ versus PC1′ diagram, reaching a point where it crosses the line α and falls in the C/X-complex region. We applied the taxonomic classification to the spectrum of the metal-rich chondrite NWA 12273 obtained by Reddy et al. (2019) and found that the PC1′ and PC2′ values also fall in the C/X-complex region. These results show that the presence of metal could explain the weak absorption bands of the NEOs.

The presence of shock-darkened or impact melt material can also have a significant effect on the spectral properties of asteroids and meteorite samples. Shock darkening occurs at pressures of ∼40–50 GPa, whereas impact melt requires pressures of over 90–150 Gpa (e.g., Kohout et al. 2020). Kohout et al. (2014) found that the effects of shock darkening and impact melt on the spectrum of an LL-chondrite are essentially the same; i.e., increasing the amount of these lithologies will produce a decrease in absolute reflectance and suppression of the absorption bands. Since the spectral effects of the two lithologies are indistinguishable, in the present work, we will refer to them as just shock darkening.

Reddy et al. (2014) suggested that shock darkening could be responsible for the low albedo and subdued absorption bands seen among asteroids of the Baptistina family. More recently, Battle et al. (2022) found compelling evidence for the presence of shock darkening in the NEO (52768) 1998 OR2 that could explain its weak absorption bands and its classification as an Xn-type.

Figure 16 (black circles) shows the results of applying the Bus–DeMeo taxonomic classification to the spectra of intimate mixtures of Chelyabinsk (light colored lithology) and the shock-darkened material from Reddy et al. (2014). The results show how shock darkening can effectively turn a Q-type asteroid into a C/X-type object when the amount of shock-darkened material is >50%.

To summarize, in this section, we have discussed the factors that could be responsible for the weak absorption bands of four NEOs whose compositions are similar to those of ordinary chondrites. These objects represent ∼5% of the entire sample and ∼7% of the objects with ordinary-chondrite-like composition studied in this work. We suggest that the presence of metal or shock darkening could be responsible for the unusual spectral characteristics of these objects. Other possible explanations, such as the presence of carbonaceous chondrite material or even a mixture of carbonaceous chondrite and metal, could have a similar effect. Although the spectral characteristics of these NEOs do not seem to be consistent with this scenario, we leave this possibility open for a future investigation.

Determining which asteroids have metal and which have shock-darkened material is a more complicated task, but in some cases it might be possible from the NIR spectrum. For example, the spectrum of 2016 CM194 has the less steep spectral slope of the four NEOs; if the presence of metal were responsible for the weak absorption bands of this object, we should also see a very steep spectral slope. This is evident in Figure 17, which shows the effects of adding meteoritic metal to an ordinary chondrite. Increasing the amount of metal will suppress the absorption bands and also increase the spectral slope. For the spectrum corresponding to the 100% Viñales sample, we measured Band I and II depths of 34% and 11%, respectively, but for the mixture corresponding to 80% Gibeon and 20% Viñales, the Band I depth decreased to 9% and the Band II depth to ∼3%. In the case of the spectral slope, which was measured as the slope of a linear fit performed from the reflectance maximum at ∼0.7 μm to the reflectance maximum at ∼1.48 μm, the value changed from $-0.02621\ \mu\mathrm{m}^{-1}$ (100% Viñales) to $0.4112\ \mu\mathrm{m}^{-1}$ (80% Gibeon and 20% Viñales). Thus, for 2016 CM194, we favor shock darkening, which can suppress the absorption bands but has little effect on the spectral slope (Reddy et al. 2014).

The spectra of NEOs 2013 CW32, 2017 WX12, and 2019 SH6 show red (steep) spectral slopes, which makes it more difficult to rule out metal just by looking at the spectra, as in the case of 2016 CM194. Apart from metal, both space weathering and phase reddening also increase the spectral slope, introducing further complications to the analysis. NEOs 2013 CW32 and 2017 WX12 were observed at phase angles of 10° and 21°, respectively, and are probably not very affected by phase reddening (Sanchez et al. 2012), but they might have experienced some degree of space weathering. 2019 SH6, on the other hand, was observed at a phase angle of 53°, and its spectral slope is likely affected by phase reddening. The surface of this object could also be affected by space weathering. In cases like these, radar data could be useful to rule out or confirm the presence of metal, since high radar albedos are typically associated with metal-rich asteroids.

For NEO 2013 CW32, Virkki et al. (2022) reported a radar albedo ($\hat{\sigma}_{OC}$) in the range of 0.23–0.31. This range is higher than the mean $\hat{\sigma}_{OC}$ found by these authors for S- and Q-type NEOs (0.19 ± 0.06), which could indicate the presence of some metal mixed with ordinary-chondrite-like material, perhaps similar to meteorites NWA 12273 and NWA 12379. Unfortunately, for 2017 WX12 and 2019 SH6, there are no radar data available, and the limited information that we have for these objects is insufficient to further constrain their composition.
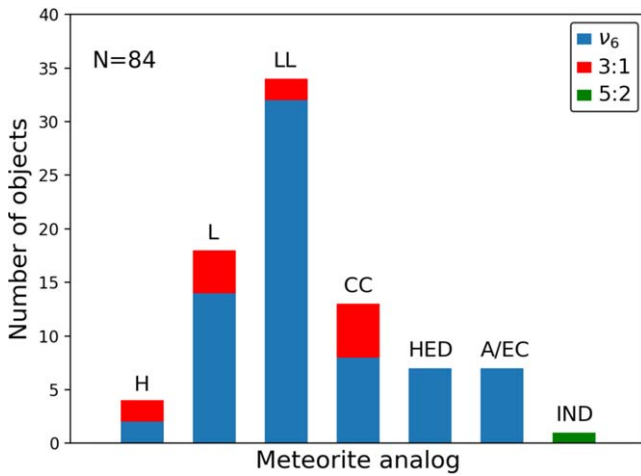
Figure 18. Distribution of meteorite analogs found in the present study. Meteorite abbreviations are H-, L-, and LL-ordinary chondrites; carbonaceous chondrites (CC); HEDs; aubrites and enstatite chondrites (A/EC); and indeterminate (IND). The source regions of the NEOs are indicated with different colors.

2.7. NEO Source Regions

An important part of the study of NEOs is to determine their source regions, as this allow us to establish which of those regions contribute the most to the influx of asteroids to the near-Earth space, as well as identifying the possible parent bodies of NEOs and meteorites that fall on Earth. In order to determine the likely source regions for the NEOs in our sample, we used the NEO model described by Granvik et al. (2017, 2018). This model yields the probability that an asteroid escaped out of one of seven different regions, including the ν_6 secular resonance; the 3:1, 5:2, and 2:1 mean-motion resonances (MMR) with Jupiter; and the Hungaria, Phocaea, and Jupiter-family comet regions.

The dynamical modeling showed that the ν_6, 3:1, and 5:2 resonances have the highest probabilities of escape for the studied NEOs. In particular, we found that 83% of the objects escaped from the ν_6, 16% from the 3:1, and just 1% from the 5:2. The number of objects from each region corresponding to each taxonomic type and meteorite analog are shown in Figures 3 and 18, respectively. In total, 50% of the NEOs with an H-chondrite-like composition escaped from the ν_6 resonance and 50% from the 3:1 resonance. For those objects with an L-chondrite-like composition, the major contribution was from the ν_6 (78%) followed by the 3:1 resonance (22%). In the case of the NEOs with an LL-chondrite-like composition, 94% escaped from the ν_6 resonance and only 6% from the 3:1 resonance. Approximately 62% of the objects with an affinity to carbonaceous chondrites escaped from the ν_6 and the rest from the 3:1 MMR. All the objects whose meteorite analogs were found to be HEDs, aubrites, or enstatite chondrites were delivered to the near-Earth space through the ν_6 resonance. The only asteroid whose taxonomic type was indeterminate was found to escape from the 5:2 MMR.

The results presented in this study are consistent with previous work that found that most NEOs originate in the innermost region of the main belt, with the ν_6 resonance being the major contributor (e.g., Dunn et al. 2013; Binzel et al. 2019). We notice that H-chondrites, the less common type of ordinary chondrites in our sample, also show the lowest contribution from the ν_6 resonance compared to the L- and LL-

chondrites. This result is similar to the findings of Binzel et al. (2019) that showed that the 3:1 resonance, the Phocaea region, and the 5:2 resonance contribute the most to the delivery of H-chondrites from the main belt. This could explain the relatively low number of H-chondrites in our sample, as only 14% of all NEOs with an ordinary-chondrite-like composition escaped from the 3:1 resonance and none from the Phocaea region or the 5:2 resonance. The lack of objects coming from the Phocaea region and the 5:2 resonance is to be expected, since the model of Granvik et al. (2018) shows a negligible contribution of small objects from these source regions.

3. Photometric Study

3.1. Observations and Analysis

As explained in Section 2.1, for those observations where the asteroids were faint, MORIS was used for guiding, and images were saved to simultaneously obtain the lightcurves. MORIS images were taken using an LPR600 filter, and exposure times were selected according to the object brightness and weather conditions to maximize the target's S/N. Typically, the exposure times were between 5 and 15 s for an error between 0.03 and 0.08 mag in the photometric data. Due to the small field of view of the MORIS imager and the fast sky motion of the observed NEOs, observations were carried out by tracking the targets, so there is no reference star in the field of view for the photometry. Therefore, we report only instrumental photometry (Thirouin 2013). Using the Lomb (1976) procedure, we searched for periodicity in the time-series photometry of each NEO to infer its lightcurve.

Since MORIS was not used for all the spectroscopic observations, the number of asteroids for which we obtained photometric data is smaller than the number of asteroids with spectroscopic data. For this reason, lightcurves are not available for all the NEOs presented in Section 2. It is also important to note that there were some cases where the S/N of the final spectrum of the asteroid was deemed too low to be published. As a result, not all the NEOs presented in this section have an NIR spectrum (see Table 1).

3.2. Lightcurves and Rotational Periods

The sample for the photometric study consists of 59 NEOs with H ranging from ∼20 to 27.4 mag (Figure 19). Our target sample is probing the Aten, Amor, and Apollo dynamical classes, but the sample is dominated by the Apollo class, with 59% of our targets in this group, while 27% are Amor NEOs and 14% Aten NEOs.

The amount of time dedicated to obtaining the photometric data was limited by the amount of time needed to obtain the asteroid spectra. Because of this, for most NEOs, the observing block was ∼2 hr. This, in general, is enough time for most of the objects with $H > 22$, since they typically have a rotational period of less than 2 hr (Warner et al. 2009; Thirouin et al. 2016). However, such an observing strategy created a bias against slow rotators, as we are not able to report full lightcurves with rotational periods longer than our observing block. For NEOs with $H < 22$, our observing strategy is an issue, as most of the NEOs in this size range have rotational periods longer than 2 hr (Figure 20).

Lightcurves obtained for this work are classified into four groups: (1) full lightcurves with a rotational period and lightcurve peak-to-peak amplitude estimates (tumblers are not
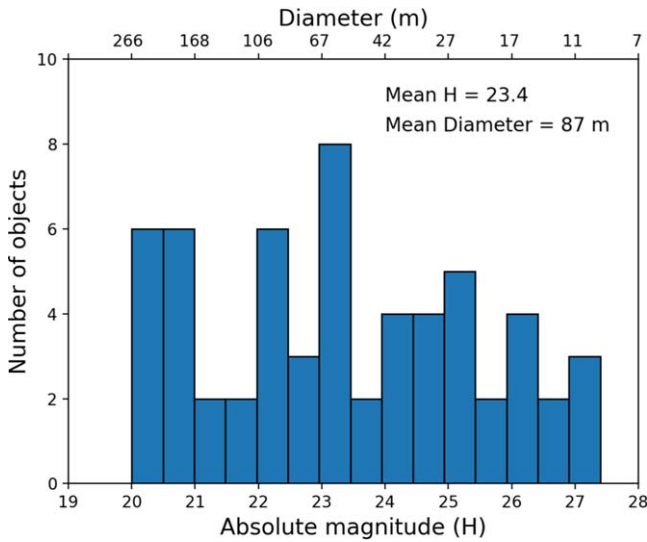
Figure 19. Distribution of absolute magnitudes (H) and diameters for the NEOs included in the photometric study. Diameters were calculated from the absolute magnitudes and the mean geometric albedo of the photometric sample ($P_V = 0.25$).
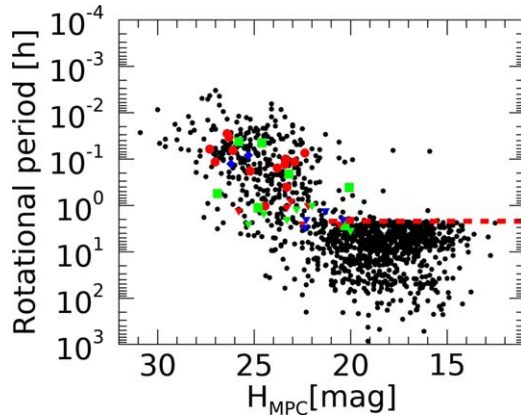
Figure 20. Rotational periods vs. absolute magnitudes for all NEOs with published lightcurves (black dots). NEOs with a full lightcurve presented in this study are depicted with red circles (Apollos), green squares (Amors), and blue diamonds (Atens). NEOs with partial lightcurves (i.e., a lower limit for their periods) are indicated with triangles and the same color code as mentioned before. The red dashed line is the spin barrier at 2.2 hr.

included), (2) partial lightcurves with an increase/decrease in brightness and only a lower limit for the rotational period and peak-to-peak amplitude, (3) flat lightcurves without any clear trend of brightness variability, and (4) lightcurves of NEOs with a non-principal-axis rotation, also known as tumblers. Table 5 summarizes our results.

Full lightcurves—We derived the full lightcurve of 17 NEOs, which corresponds to about 29% of our sample (Figures 28–33 in the Appendix). For each NEO, we plotted its Lomb periodogram and the lightcurve corresponding to the periodicity with the highest confidence level. For each lightcurve, a Fourier series is fitted to the photometric data, and the order of the fit depends on the lightcurve morphology.

Full lightcurves of 2014 EK24, 2014 UV210, 2005 TF, 2015 WF13, and 2020 SN are in agreement with already-published lightcurves (see references in Table 5). However, our lightcurve of 2013 XA22 is inconsistent with the literature. Warner & Stephens (2020) inferred a rotational period of about 2.3 hr, but

our photometric data are best fitted with a rotational period of 0.1149 hr for 2013 XA22. Our data are incompatible with a rotational period of 2.3 hr, so we cannot confirm the Warner & Stephens (2020) results. We note that both lightcurves present a high dispersion; therefore, higher data quality would be useful to secure the rotational period of this object. Similarly, the lightcurve of 1999 LP28 is incomplete, and the derived rotational period seems a bit too short for an object in this size range; therefore, more data are required to confirm our results.

All full lightcurves reported in this paper are asymmetric, with both peaks (maxima or minima) not reaching the same relative magnitude. Several lightcurves, such as the ones of 2020 SN, 2015 WF13, 2014 SF304, and 2014 QH33, require a high fit order to match the observations, as they display additional peaks/valleys inferring that these NEOs have a complex shape.

Partial lightcurves—All partial lightcurves are plotted as relative magnitude versus Julian Date (Figures 34–37 in the Appendix). For these lightcurves, lower limits for the rotational period and the lightcurve amplitude are inferred based on the duration of our observing blocks. Large objects tend to rotate in more than 2 hr; thus, our observing blocks are too short to cover the (nearly) full object's rotation. As an example, we observed 2005 NW44 for about 2 hr, but since its rotational period is ∼32 hr, our observing block was too short to cover a significant amount of the object's rotation to retrieve such a long rotational period (Warner 2018).

We highlight one NEO due to its very large lightcurve amplitude; 2002 LY1 presents an amplitude larger than 1.6 mag over about 2 hr of observations, which is in agreement with Warner (2016a). The lightcurve of 2016 JD18 is interesting due to its large amplitude and irregular morphology. Unfortunately, due to the limited observing block, we are not able to derive or constrain the rotational period of this asteroid. In fact, this object may present a combination of complex shape and tumbling rotation. To our knowledge, only one partial lightcurve of this object is available, in Thirouin et al. (2018), who suggested that 2016 JD18 has a complex shape.

Flat lightcurves—Fourteen NEOs display a flat lightcurve, so we cannot constrain their rotational properties (Figures 38–40 in the Appendix). Most lightcurves present a large dispersion due to low data quality and/or bad weather. One can appreciate that the dispersion for the lightcurve of 2020 RO6 is larger than the dispersion of the other lightcurves. But in some cases, the observing block was too short to see any sign of variability, which is the case for the lightcurve of 2015 CN13.

Tumblers—We classified nine NEOs as tumblers.[9] For five of them, we were able to retrieve the primary rotational period, and we plotted the corresponding lightcurve (Figures 41–43 in the Appendix), but for four of them, no rotational period was retrieved. 2015 XC and 2020 ST1 were already classified as tumblers by Warner (2016b) and Warner & Stephens (2021b), and our work confirmed their results. 2020 YQ3 is classified as a tumbler by Warner & Stephens (2021c), but our data are insufficient to confirm such a conclusion. For 2016 EV27, we report a lightcurve with a shorter period than the one reported in the literature, and we infer that this object is a tumbler.

The peak-to-peak lightcurve amplitudes in Table 5 are not corrected for phase angle (α) effects. Therefore, to correct these values and derive the axis ratio (a/b) of the observed NEOs,

---

[9] Due to the nature of the lightcurve of a tumbler and because we are not able to retrieve the secondary periodicity, we do not report the lightcurve amplitude.

Table 5
Rotational Periods and Lightcurve Amplitudes for the Observed NEOs

Number	Designation	Period (hr)	$\Delta m(\alpha)$ (mag)	Period$_{\rm lit}$ (hr)	$\Delta m_{\rm lit}$ (mag)	References
412995	1999 LP28	0.409	0.34 ± 0.07	⋯	⋯	⋯
459872	2014 EK24	0.0997	0.98 ± 0.03	0.0996 ± 0.0002	0.56 ± 0.02	Thirouin et al. (2016)
				0.0998 ± 0.0002	1.26 ± 0.01	Thirouin et al. (2016)
				0.0998 ± 0.0001	0.83 ± 0.15	Godunova et al. (2016)
				0.0999 ± 0.0001	0.76 ± 0.04	Tan et al. (2018)
				0.0998 ± 0.0005	0.45 ± 0.03	Monteiro et al. (2018)
469737	2005 NW44	>2	>0.15	31.5 ± 0.2	0.13 ± 0.02	Warner (2018)
496816	1989 UP	>2.5	>0.65	6.98 ± 0.02	1.16 ± 0.02	Wisniewski et al. (1997)
501647	2014 SD224	>3	>0.25	⋯	⋯	⋯
515742	2015 CU	⋯	⋯	⋯	⋯	⋯
515767	2015 JA2	⋯	⋯	0.9801 ± 0.0003	0.10 ± 0.02	Unpublished[b]
	2001 YV3	>2.5	>0.45	⋯	⋯	⋯
	2002 LY1	>2	>1.6	3.204 ± 0.005	1.24 ± 0.05	Warner (2016a)
	2005 NE21	>1.3	>0.25	⋯	⋯	⋯
	2005 TF	2.74	0.22 ± 0.05	2.724 ± 0.005	0.22 ± 0.04	Vaduvescu et al. (2017)
				2.57 ± 0.01	0.32 ± 0.03	Warner (2017)
				2.630 ± 0.014	0.20 ± 0.03	Carbognani et al. (2018)
				2.57 ± 0.05	0.18 ± 0.05	Hasegawa et al. (2018)
	2013 RS43[a]	0.1156	⋯	⋯	⋯	⋯
	2013 XA22	0.1149	0.40 ± 0.05	2.2912 ± 0.0008	0.26 ± 0.03	Warner & Stephens (2020)
	2014 QH33	1.03	0.47 ± 0.03	⋯	⋯	⋯
	2014 QL32	>1.2	>0.5	⋯	⋯	⋯
	2014 QZ265	0.0831	0.30 ± 0.05	⋯	⋯	⋯
	2014 SF304	0.0610	0.45 ± 0.07	⋯	⋯	⋯
	2014 UV210	0.5553	0.96 ± 0.05	0.5559 ± 0.0002	0.91 ± 0.04	Thirouin et al. (2016)
	2014 VH2[a]	⋯	⋯	38.9 ± 0.5	0.931 ± 0.04	Warner (2015)
	2014 WN4	>2	>0.3	⋯	⋯	⋯
	2014 WO4	⋯	⋯	⋯	⋯	⋯
	2014 WO7	⋯	⋯	⋯	⋯	⋯
	2014 WP4	⋯	⋯	⋯	⋯	⋯
	2014 WY119	0.0337	0.68 ± 0.09	⋯	⋯	⋯
	2014 XB6[a]	⋯	⋯	⋯	⋯	⋯
	2015 AP43	>3.5	>0.25	⋯	⋯	⋯
	2015 BK509	0.07406	0.51 ± 0.08	0.074114 ± 0.000007	0.39 ± 0.03	Unpublished[b]
	2015 CA40[a]	0.4440	⋯	⋯	⋯	⋯
	2015 CN13	⋯	⋯	22.7 ± 0.3	0.60 ± 0.05	Warner & Oey (2015)
	2015 GY	⋯	⋯	⋯	⋯	⋯
	2015 HE10	0.0652	0.59 ± 0.02	⋯	⋯	⋯
	2015 HW11	>1.1	>0.2	⋯	⋯	⋯
	2015 JW	0.0422	0.51 ± 0.03	⋯	⋯	⋯
	2015 KA[a]	0.1274	⋯	⋯	⋯	⋯
	2015 MC	⋯	⋯	⋯	⋯	⋯
	2015 SA[a]	⋯	⋯	⋯	⋯	⋯
	2015 SE	0.0283	1.08 ± 0.05	⋯	⋯	⋯
	2015 SZ[a]	⋯	⋯	>4	>0.03	Thirouin et al. (2016)
				41.0 ± 1.0	1.33 ± 0.10	Warner (2016b)
	2015 TB25[a]	>1.5	⋯	⋯	⋯	⋯
	2015 TE	>2.5	>0.5	1.68 ± 0.05	0.19 ± 0.03	Unpublished[c]
	2015 TF	>1	>0.1	⋯	⋯	⋯
	2015 WF13	0.2111	0.19 ± 0.05	0.21194 ± 0.00005	0.23 ± 0.05	Warner (2016b)
	2015 XC[a]	0.1814	⋯	0.181099 ± 0.000006	0.53 ± 0.05	Warner (2016b)
				0.2767 ± 0.0001	0.39 ± 0.04	Carbognani & Buzzi (2016)
	2016 CO247	⋯	⋯	⋯	⋯	⋯
	2016 EV27[a]	0.1296	⋯	61 ± 1	0.45 ± 0.05	Warner (2016c)
	2016 FV13	>1.3	>0.4	⋯	⋯	⋯
	2016 JD18	⋯	⋯	>0.5	>1.3	Thirouin et al. (2018)
	2016 LG	>2.5	>0.6	4.39 ± 0.01	0.58 ± 0.05	Warner (2016a)
	2017 BY93[a]	>0.8	>0.15	0.82255 ± 0.00008	0.14 ± 0.01	Unpublished[b]
				>1.75	>0.14	Erasmus et al. (2017)
	2017 FU64	0.1553	0.29 ± 0.04	⋯	⋯	⋯
	2017 RR15	⋯	⋯	⋯	⋯	⋯
	2018 XG5	⋯	⋯	2.6594 ± 0.0003	0.26 ± 0.03	Warner & Stephens (2019)
	2018 XS4[a]	⋯	⋯	⋯	⋯	⋯

<div align="center">

Table 5

(Continued)

</div>

Number	Designation	Period (hr)	$\Delta m(\alpha)$ (mag)	Period$_{lit}$ (hr)	Δm_{lit} (mag)	References
	2019 YM3	0.4027	0.27 ± 0.03	⋯	⋯	⋯
	2020 KC5	⋯	⋯	⋯	⋯	⋯
	2020 RO6	⋯	⋯	⋯	⋯	⋯
	2020 SN	1.117	0.25 ± 0.05	1.193 ± 0.003	0.19 ± 0.04	Warner & Stephens (2021a)
	2020 ST1[a]	>1	>1.3	2.879 ± 0.005	1.29 ± 0.08	Warner & Stephens (2021b)
	2020 YQ3[a]	>2	>0.3	14.752 ± 0.003	0.65 ± 0.04	Unpublished[b]
				11.148 ± 0.004	0.49 ± 0.03	Warner & Stephens (2021c)

Notes. Lightcurve amplitudes are not corrected for phase angle effects; thus, we report the lightcurve amplitude at a phase angle α. We also include rotational periods and lightcurve amplitudes found in the literature (Period$_{lit}$ and Δm_{lit}) and the corresponding references.
[a] Objects with non-principal-axis rotation (i.e., tumblers).
[b] Unpublished lightcurve, but results are available at https://www.asu.cas.cz/~ppravec/.
[c] Unpublished lightcurve, but results are available at https://obswww.unige.ch/~behrend/page_cou.html.
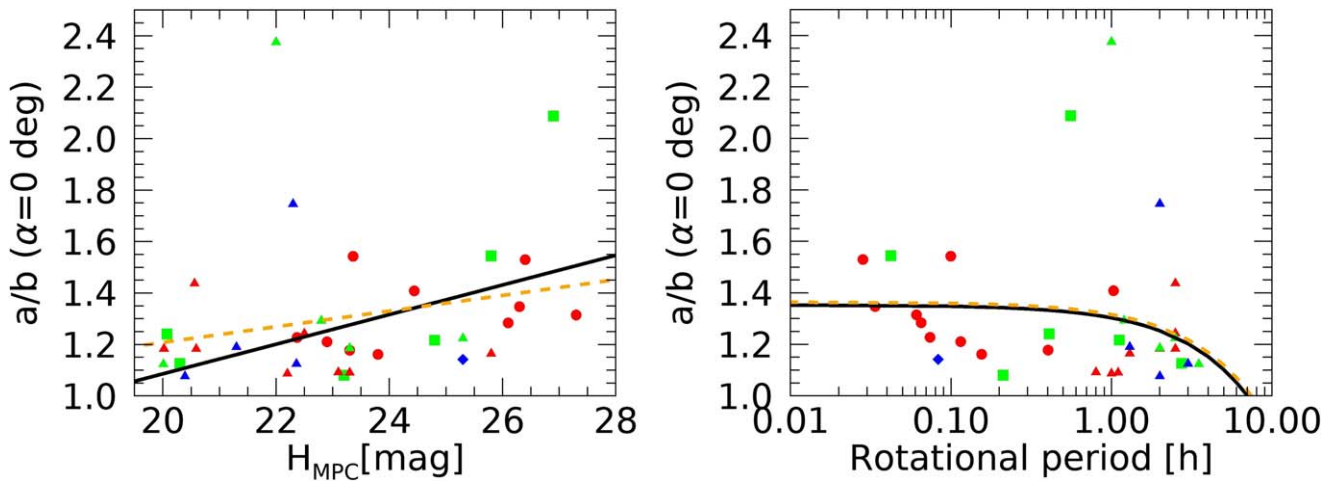
Figure 21. Axis ratio (a/b) vs. absolute magnitude (left) and rotational period (right). The same legend as Figure 20 has been used. Orange and black lines are linear fits to the entire sample (full and partial lightcurves) and to the full lightcurves only, respectively.

one has to take into account the phase angle correction as follows:

$$\Delta m(\alpha = 0^o) = \frac{\Delta m(\alpha)}{1 + s\alpha}, \qquad (5)$$

$$\frac{a}{b} \geqslant 10^{(0.4\Delta m(\alpha))/(1+s\alpha)}, \qquad (6)$$

where $\Delta m(\alpha = 0^o)$ is the lightcurve amplitude at zero phase angle and $s = 0.03$ mag deg^{-1} is the slope correlating the amplitude and the phase angle (Zappala et al. 1990; Gutiérrez et al. 2006; Thirouin et al. 2016). The average axis ratio for our sample using only the full lightcurves is 1.33, while it is 1.31 if we consider the full and partial lightcurves.

In Figure 21, we plotted the axis ratio corrected for phase angle versus absolute magnitude and rotational period; the different dynamical classes have been highlighted. Unfortunately, due to the limited sample size of NEOs with partial and/or full lightcurves, we can only report trends with a low confidence level. For the sample with only full lightcurves, we obtained $R^2 = 0.2575$, whereas for full+partial lightcurves, this value falls to $R^2 = 0.0541$. Similarly, an anticorrelation between axis ratio and rotational period is also highly

uncertain, with $R^2 = 0.0199$ for the sample with only full lightcurves and $R^2 = 0.0322$ for full+partial lightcurves.

Figure 22 shows the amplitude versus spin rate for the NEOs included in the photometric study. Most of the objects in this figure fall to the right side of the critical spin rate curves corresponding to bulk densities (ρ) of 1.0, 2.0, and 3.0 g cm^{-3}. This is consistent with the fact that the sample is dominated by small NEOs with $H > 22$ and diameters $\lesssim 150$ m. Objects in this part of the diagram cannot be held together only by self-gravitation and are often referred to as monoliths, while those falling to the left side of the critical spin rate curves are $\gtrsim 150$ m and likely rubble piles or shattered bodies (e.g., Pravec & Harris 2000). The different taxonomic types of the NEOs are indicated in the figure; however, no obvious trend can be seen. The analysis of a larger sample could help determine whether there is a link between taxonomic type and the rotational properties of the asteroids.

4. Summary

We carried out an NIR spectroscopic and photometric survey of small NEOs in order to constrain their surface mineralogy and rotation rates. The spectroscopic study included 84 objects with a mean diameter of 126 m, and the photometric study
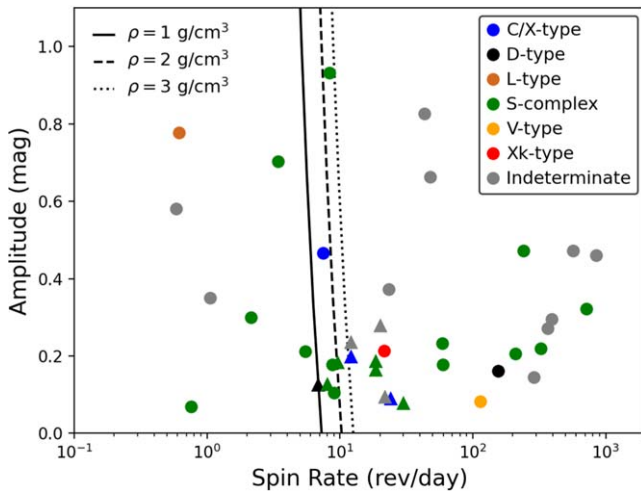
Figure 22. Amplitude vs. spin rate for the NEOs included in the photometric study. Taxonomic types are indicated with different colors. Objects whose amplitudes and spin rates were determined in this study (or previous work) are depicted with circles. Objects for which only a lower limit for the amplitude and spin rate was calculated are depicted with triangles. The curves represent the critical spin rate for bulk densities (ρ) of 1.0, 2.0, and 3.0 g cm^{-3}. Figure adapted from Pravec & Harris (2000).

included 59 objects with a mean diameter of 87 m. Thermal modeling was used to derive the albedo and diameter of those asteroids whose spectra showed a thermal excess at wavelengths $>2\,\mu$m. A compositional analysis was performed and possible meteorite analogs were identified for most of the NEOs in our sample. For the S-, Sq-, and Q-types, we estimated the degree of space weathering experienced by the objects and investigated the effect of grain size on the space-weathering parameter $\Delta\eta$.

Our research revealed the existence of NEOs with spectral characteristics and compositions consistent with ordinary chondrites but whose weak absorption bands could lead to an ambiguous classification in the C- or X-complex. For these objects, we defined a new subclass within the S-complex called Sx-types. The source regions of all the NEOs in our sample were also determined. Rotational periods and lightcurve amplitudes were obtained from the photometric data, and this information was used to derive the axis ratios of the observed NEOs. Overall, most of our results are consistent with previous studies and can be summarized as follows.

1. The observed NEOs are dominated by S-complex asteroids, which comprise ∼66% of the sample. Objects classified as C/X-complex represent ∼17% of the sample, and the other ∼17% is less common taxonomic types. The proportion of taxonomic types found in this study is similar to previous work that included kilometer-sized objects.
2. For asteroids in the S-complex, we found that 8% were classified as H-, 31% as L-, and 61% as LL-chondrites. These results agree with previous studies that showed that LL-chondrites are dominant among NEOs with ordinary-chondrite-like compositions.
3. We confirmed that Q-type asteroids could have weathered surfaces and their spectral characteristics could result from the presence of large grains on the surface. However, for this mechanism to be effective, those grains cannot exceed the size at which absorption band saturation occurs. For asteroids with an LL-chondrite-like composition, this size limit is ∼400 μm.
4. We found that some NEOs with ordinary-chondrite-like composition (the Sx-types) could be hidden within the C- or X-complex as the result of their weak absorption bands. Our analysis showed that the presence of metal or shock darkening could be responsible for the attenuation of the absorption bands.
5. The dynamical modeling showed that 83% of the NEOs escaped from the ν_6 resonance, 16% from the 3:1, and just 1% from the 5:2. The small fraction of NEOs coming from the 3:1 and 5:2 resonances and the lack of objects from the Phocaea region could explain the relatively low number of H-chondrites in our sample.
6. Full lightcurves were derived for 17 NEOs (∼29% of our sample) and partial lightcurves for 19 NEOs (∼32% of our sample). Flat lightcurves were obtained for 14 asteroids, which represents ∼24% of the sample, whereas nine NEOs were classified as tumblers (∼15%).
7. No clear trend between the axis ratio and the absolute magnitude or rotational period was found. Similarly, no correlation was observed between the taxonomic type and the rotational properties of the NEOs.

Appendix

NIR spectra obtained with the SpeX instrument on the IRTF are reported in Figures 23–27. Lightcurves discussed in Section 3.2 are shown in Figures 28–43.
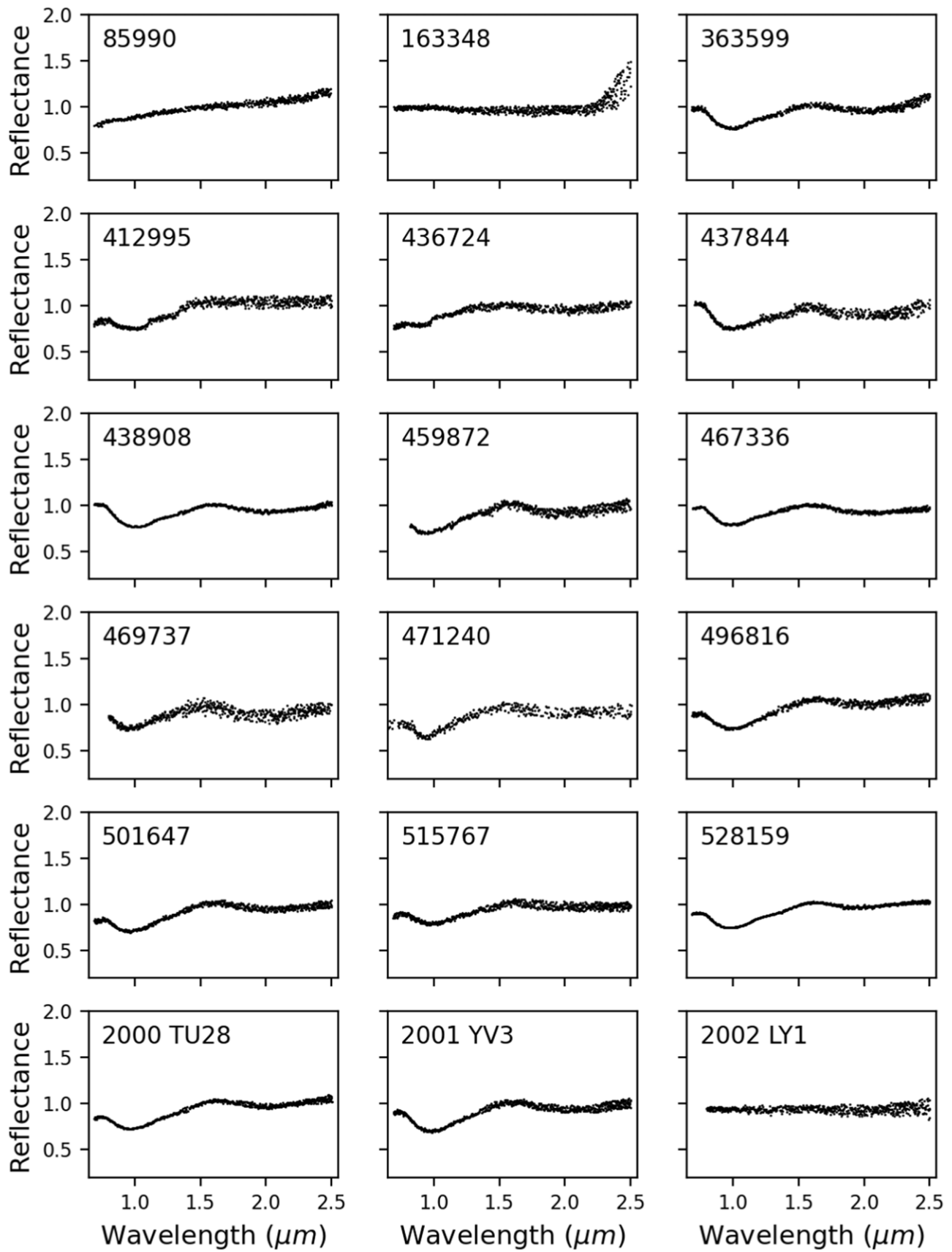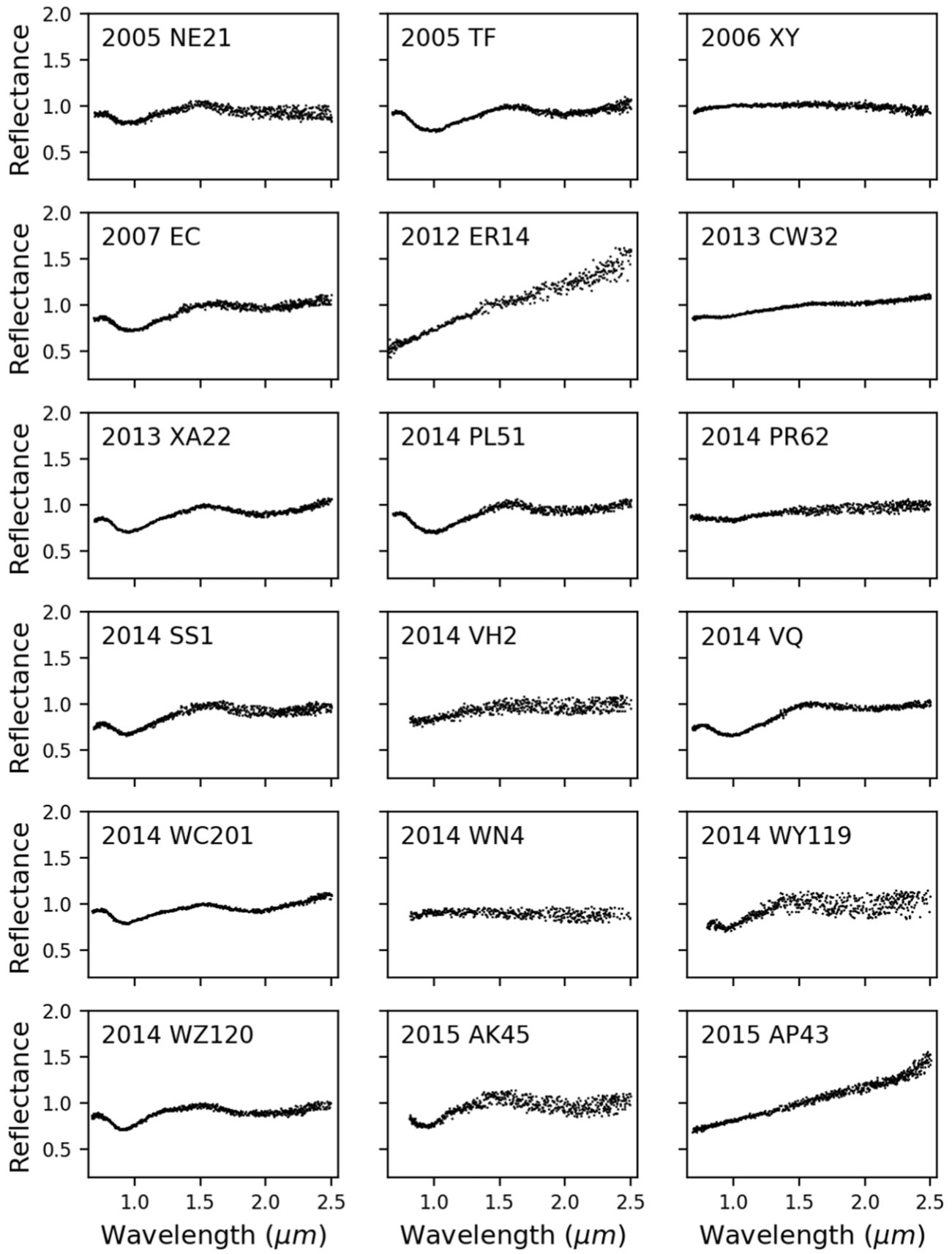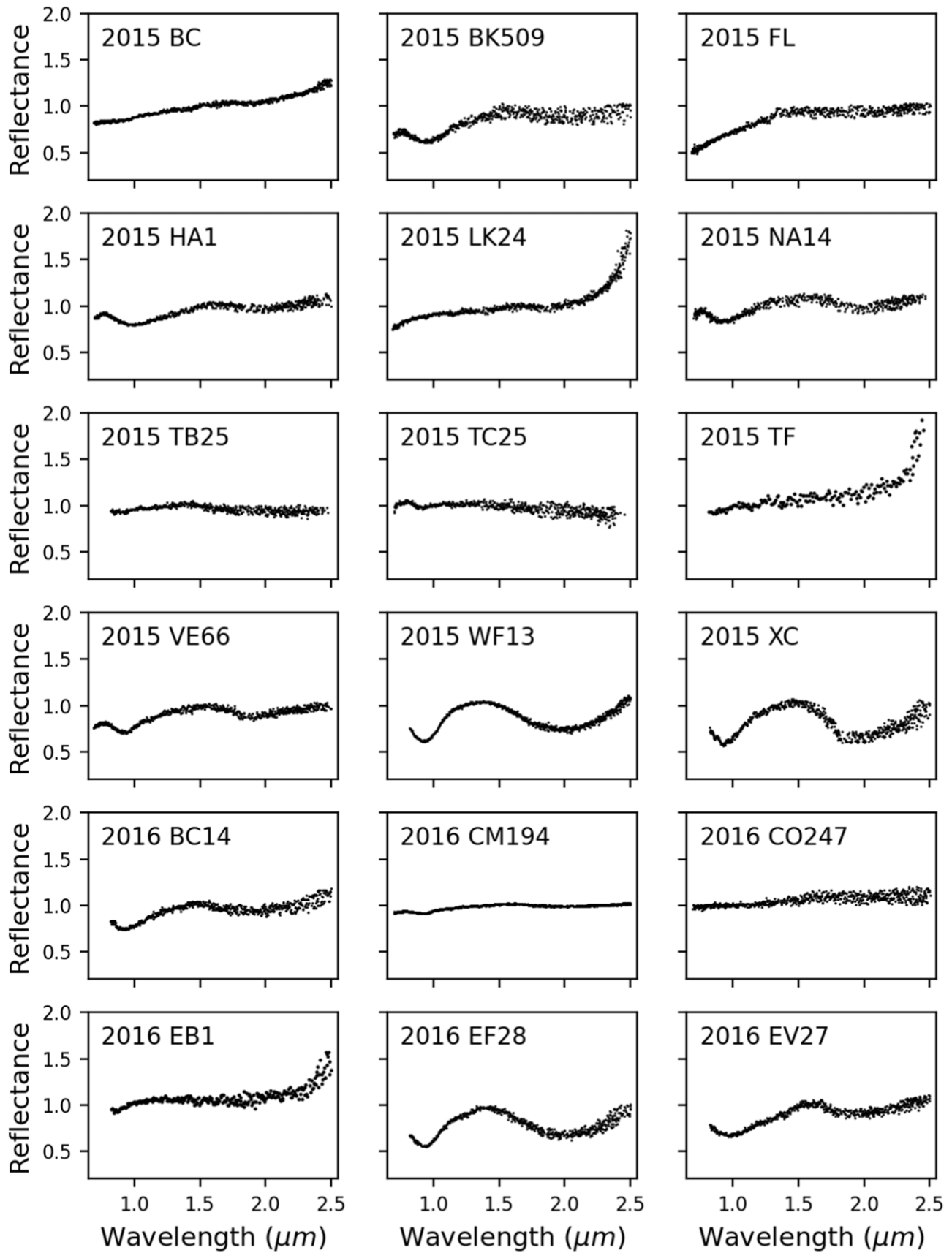
Figure 23. NIR spectra of NEOs included in the spectroscopic study.

Figure 24. NIR spectra of NEOs included in the spectroscopic study.

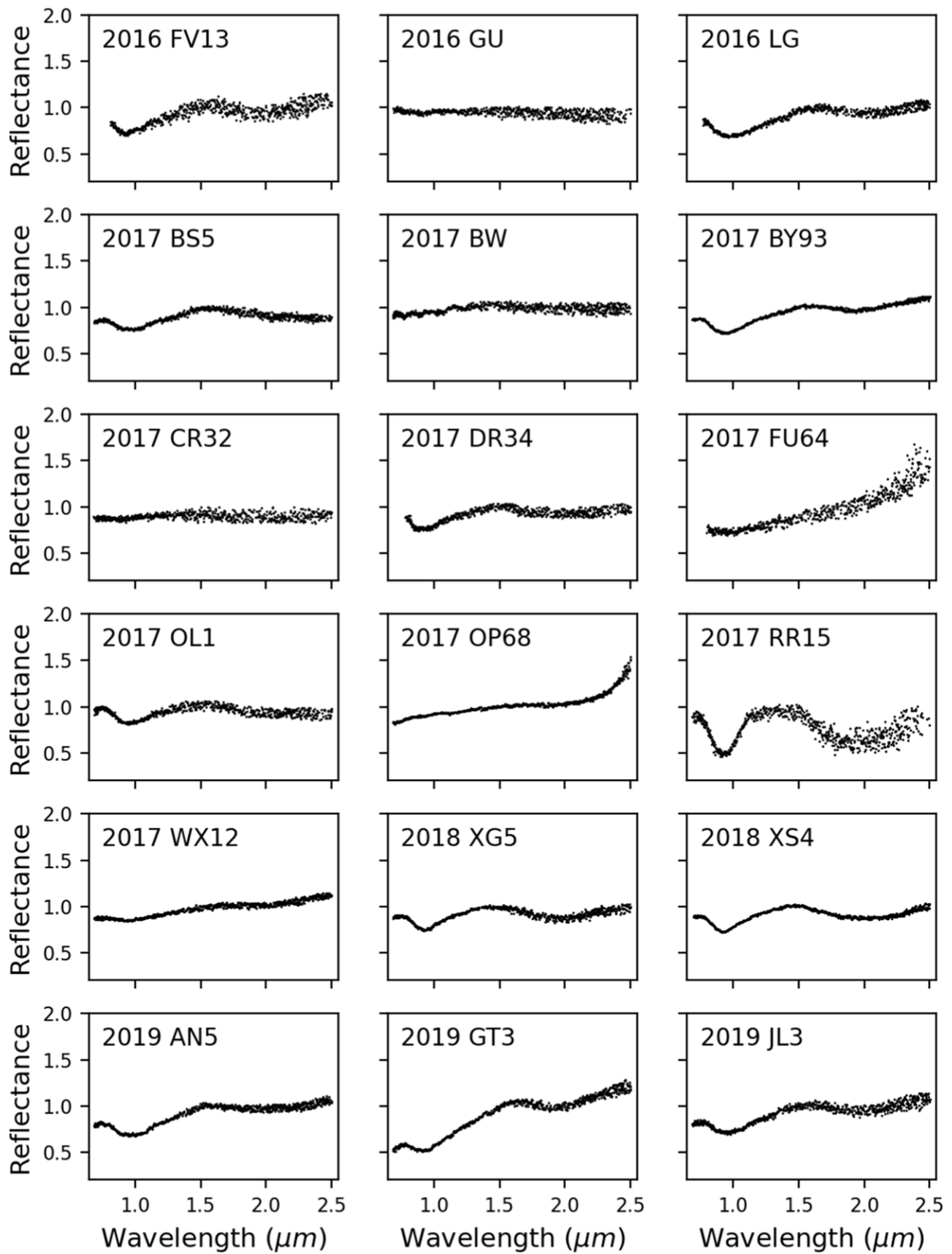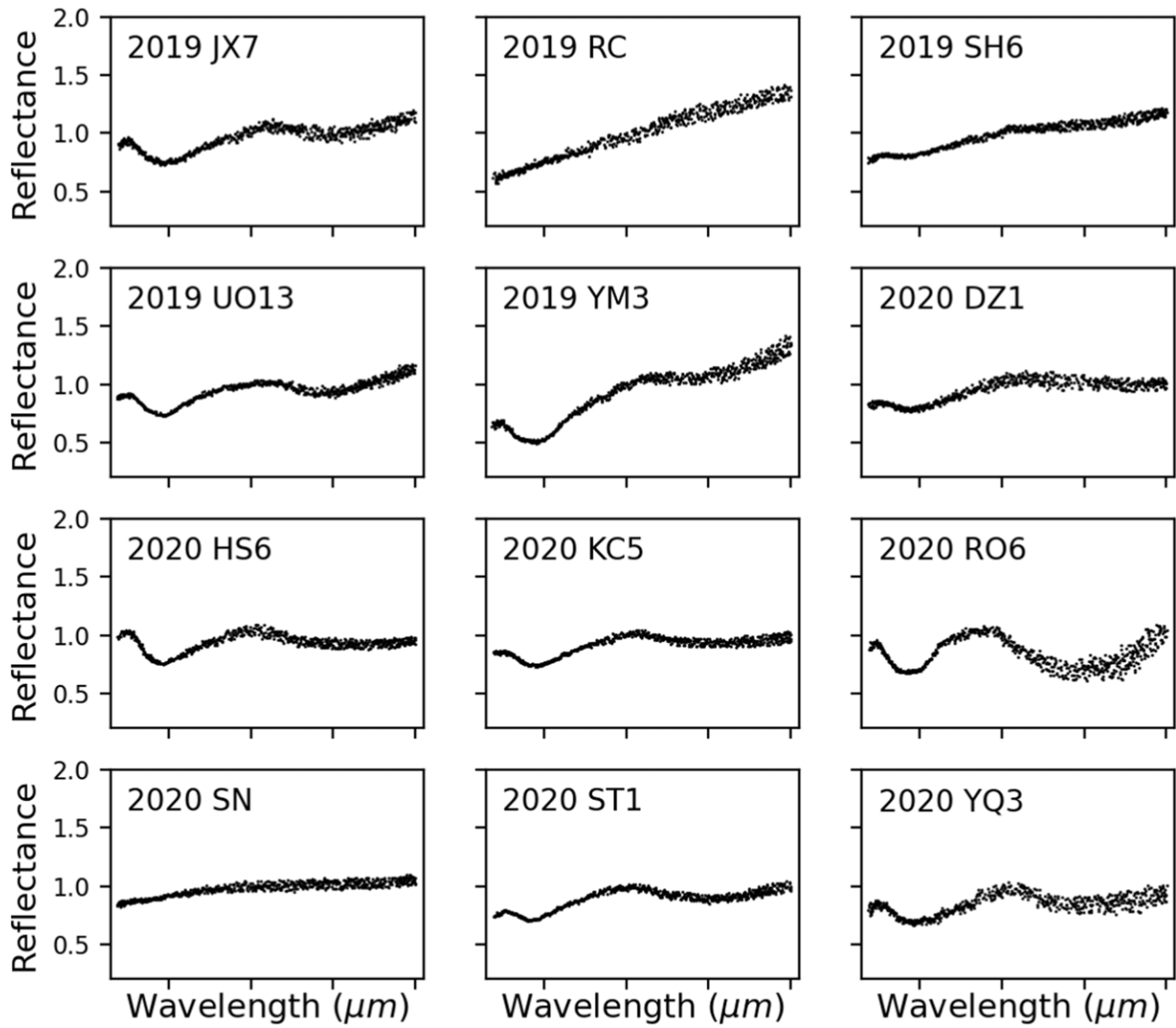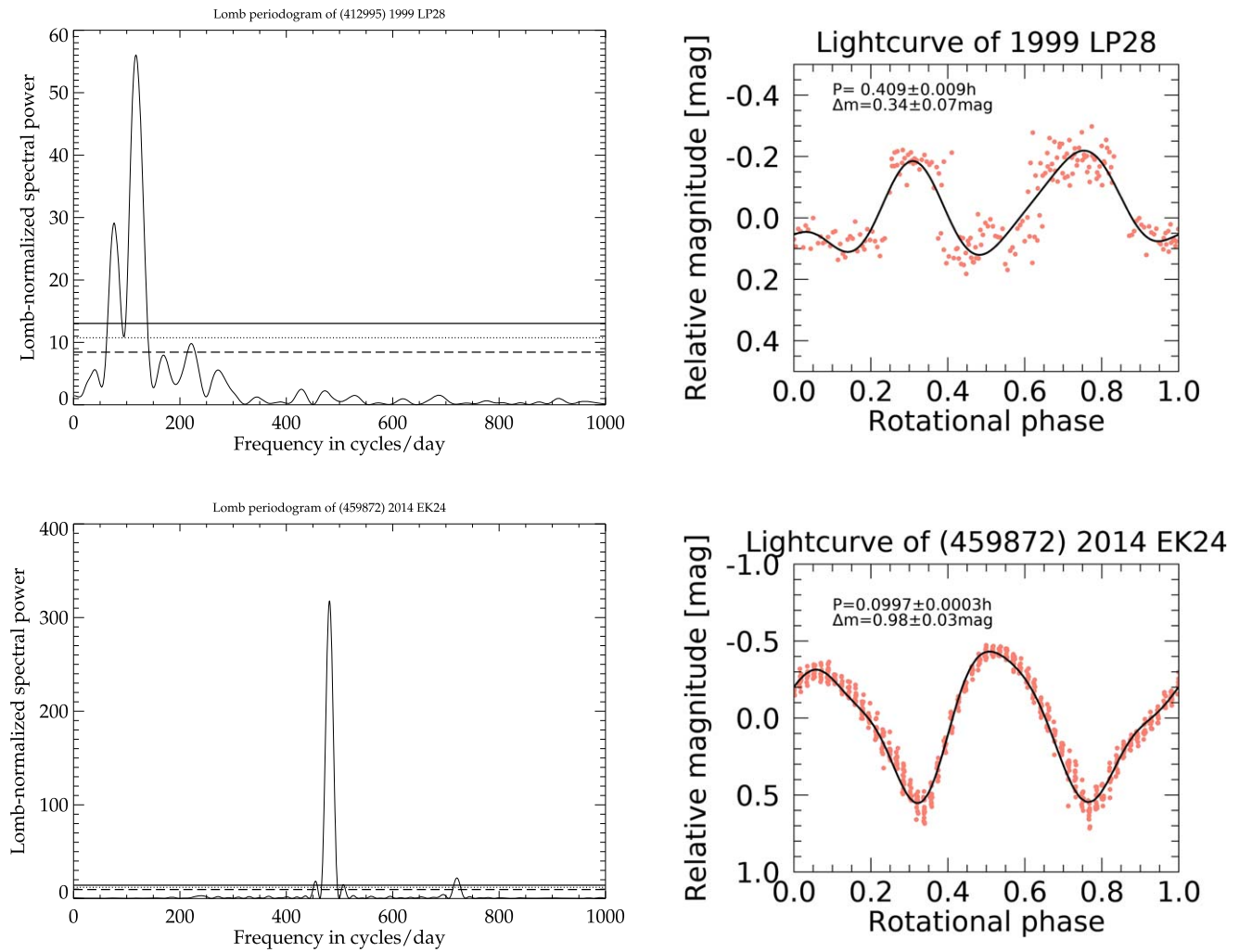**Figure 25.** NIR spectra of NEOs included in the spectroscopic study.

**Figure 26.** NIR spectra of NEOs included in the spectroscopic study.

Figure 27. NIR spectra of NEOs included in the spectroscopic study.

Figure 28. Full lightcurves of NEOs included in the photometric study. The highest peak of the Lomb periodogram is the single-peaked rotational period with the highest confidence level. The 99.9% confidence level is indicated with a solid line, while the confidence level at 99% is the dotted line, and the dashed line corresponds to a confidence level of 90%. On the right, the lightcurves corresponding to the highest confidence level peak are plotted. The lightcurves have been fitted with a Fourier series fit (black curves).
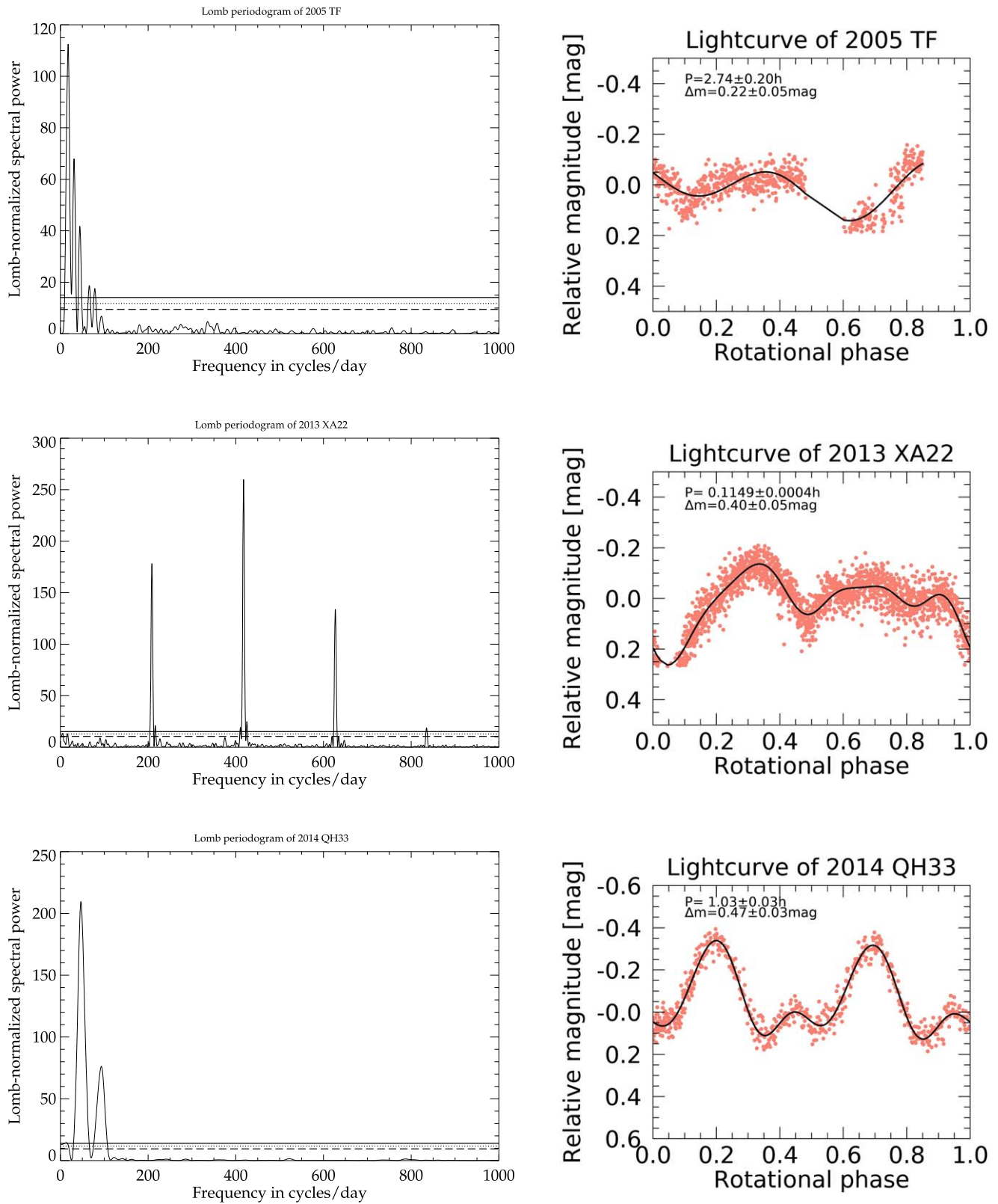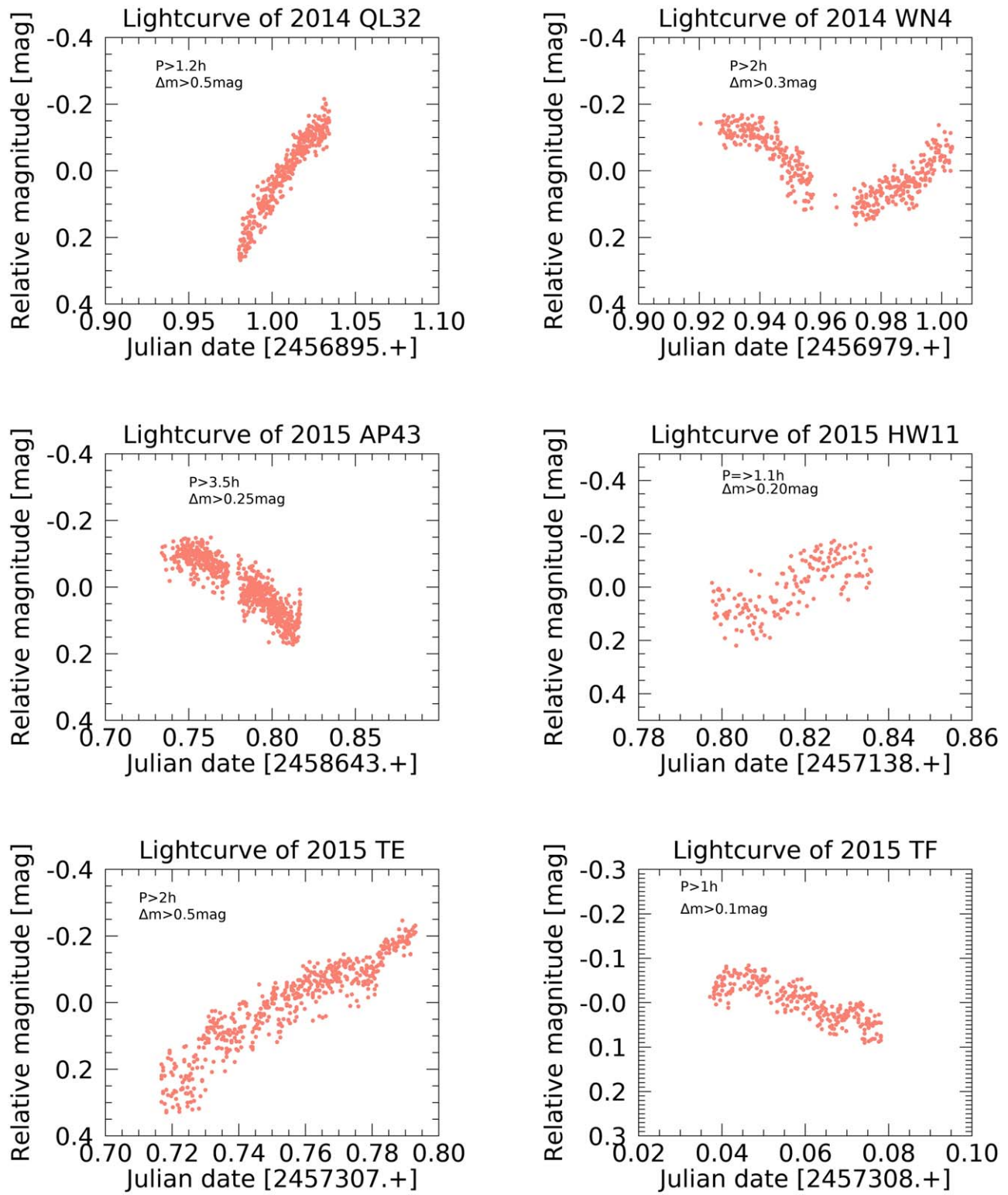
Figure 29. Full lightcurves of NEOs included in the photometric study. The highest peak of the Lomb periodogram is the single-peaked rotational period with the highest confidence level. The 99.9% confidence level is indicated with a solid line, while the confidence level at 99% is the dotted line, and the dashed line corresponds to a confidence level of 90%. On the right, the lightcurves corresponding to the highest confidence level peak are plotted. The lightcurves have been fitted with a Fourier series fit (black curves).
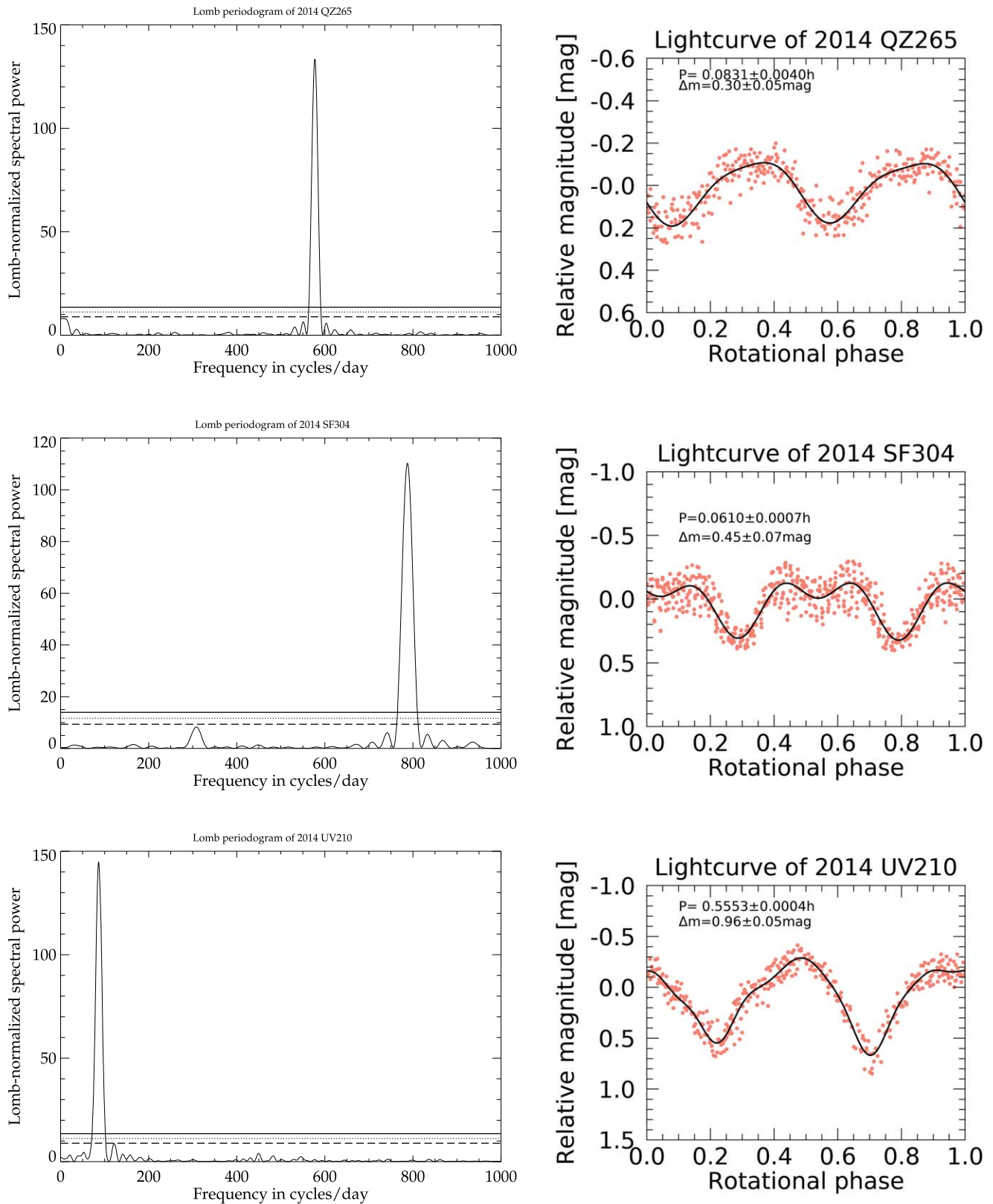
Figure 30. Full lightcurves of NEOs included in the photometric study. The highest peak of the Lomb periodogram is the single-peaked rotational period with the highest confidence level. The 99.9% confidence level is indicated with a solid line, while the confidence level at 99% is the dotted line, and the dashed line corresponds to a confidence level of 90%. On the right, the lightcurves corresponding to the highest confidence level peak are plotted. The lightcurves have been fitted with a Fourier series fit (black curves).
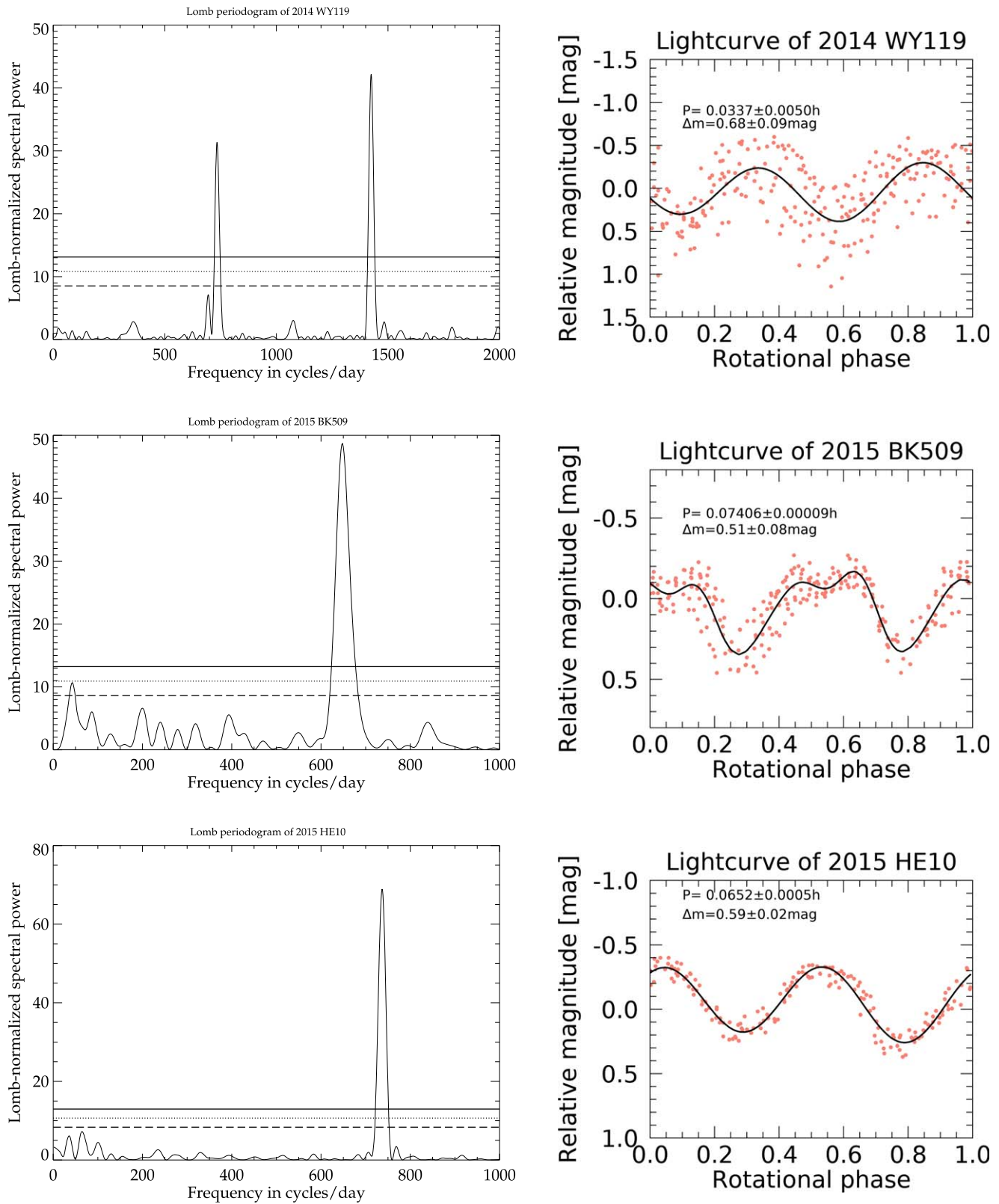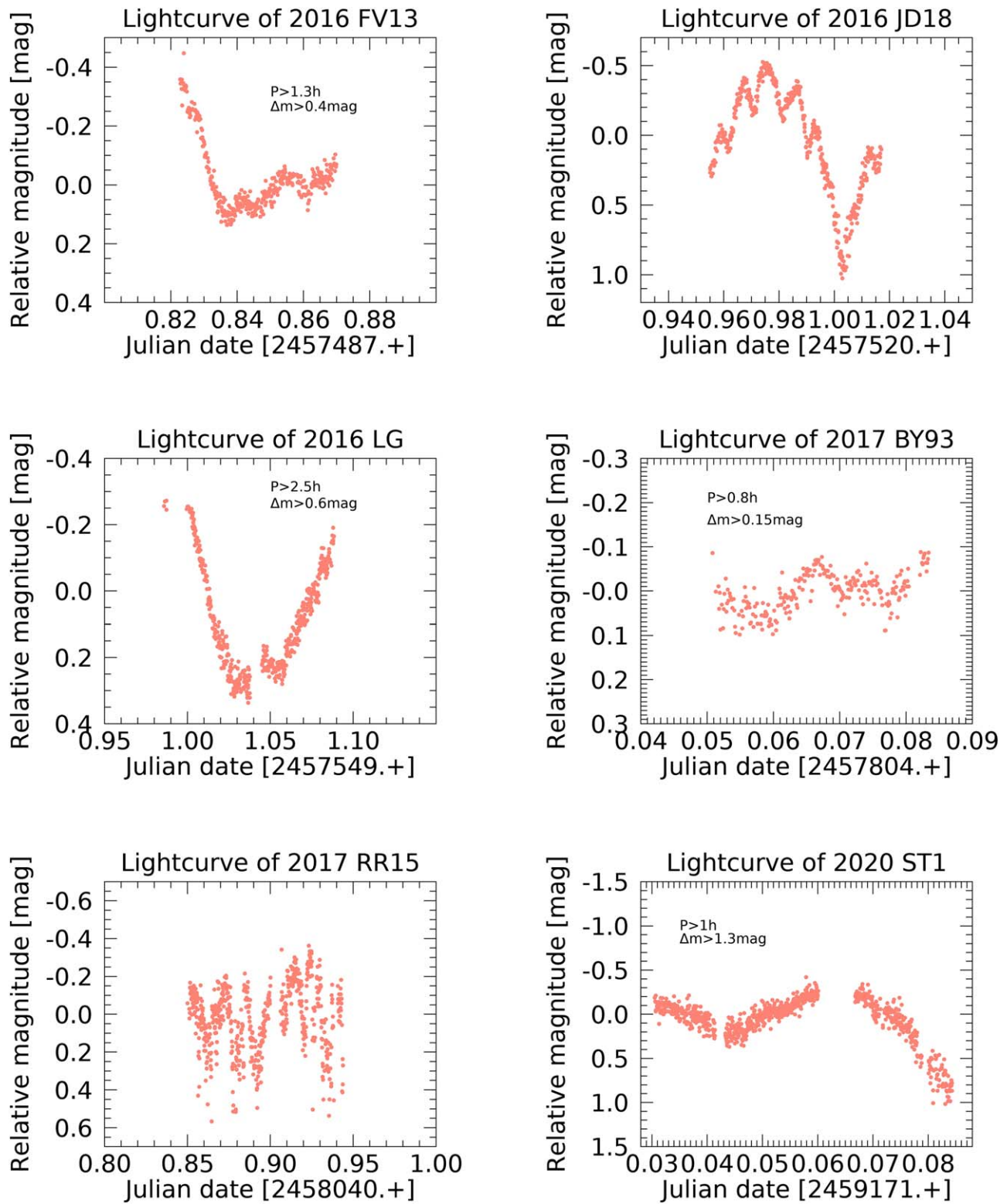
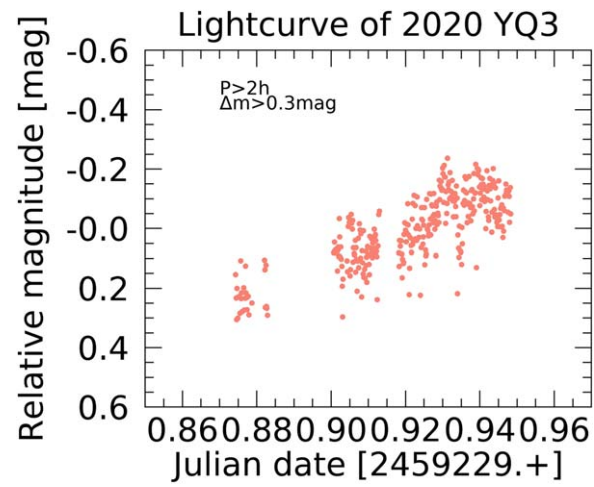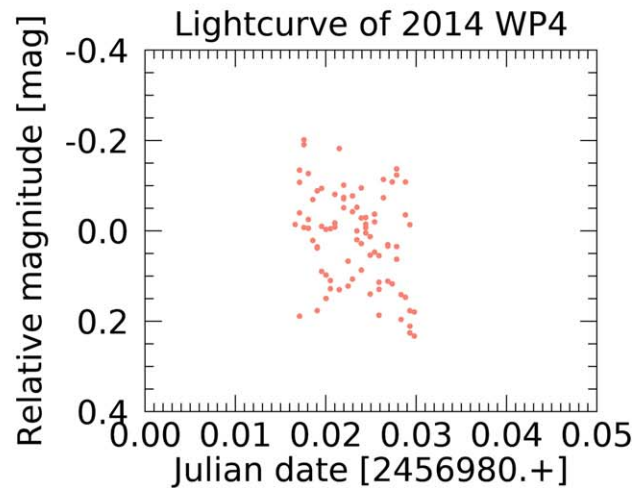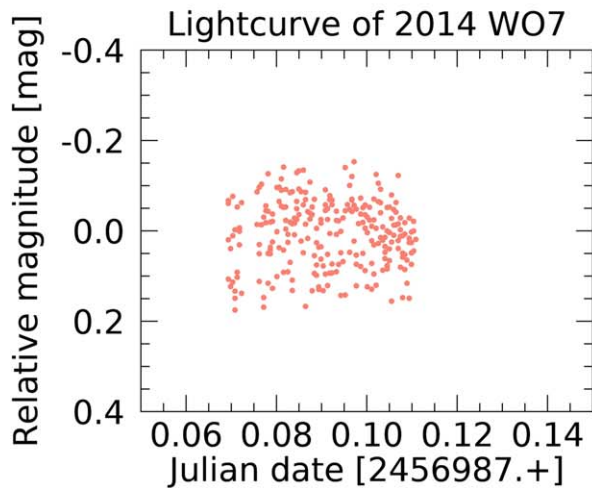**Figure 31.** Full lightcurves of NEOs included in the photometric study. The highest peak of the Lomb periodogram is the single-peaked rotational period with the highest confidence level. The 99.9% confidence level is indicated with a solid line, while the confidence level at 99% is the dotted line, and the dashed line corresponds to a confidence level of 90%. On the right, the lightcurves corresponding to the highest confidence level peak are plotted. The lightcurves have been fitted with a Fourier series fit (black curves).
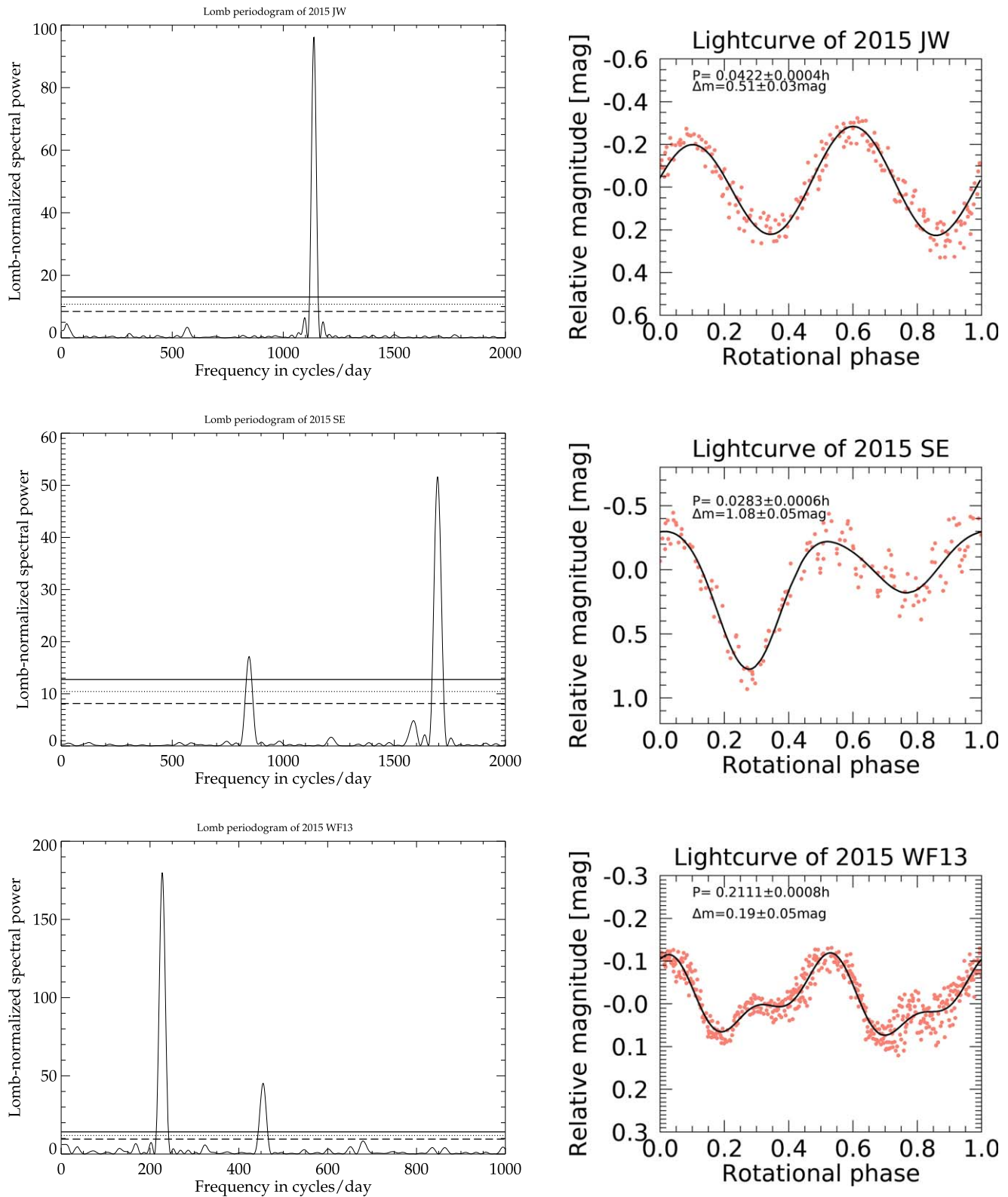
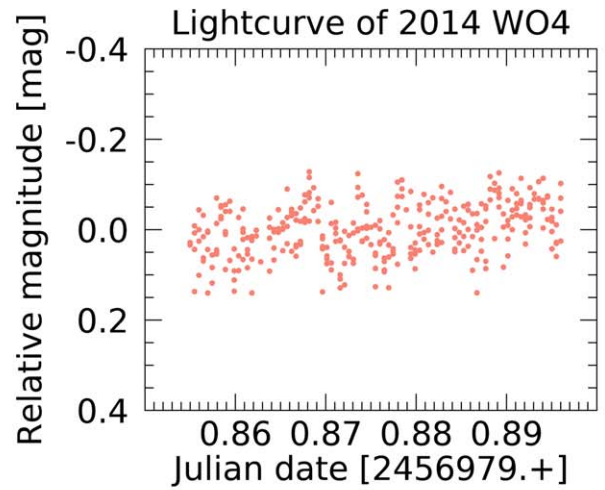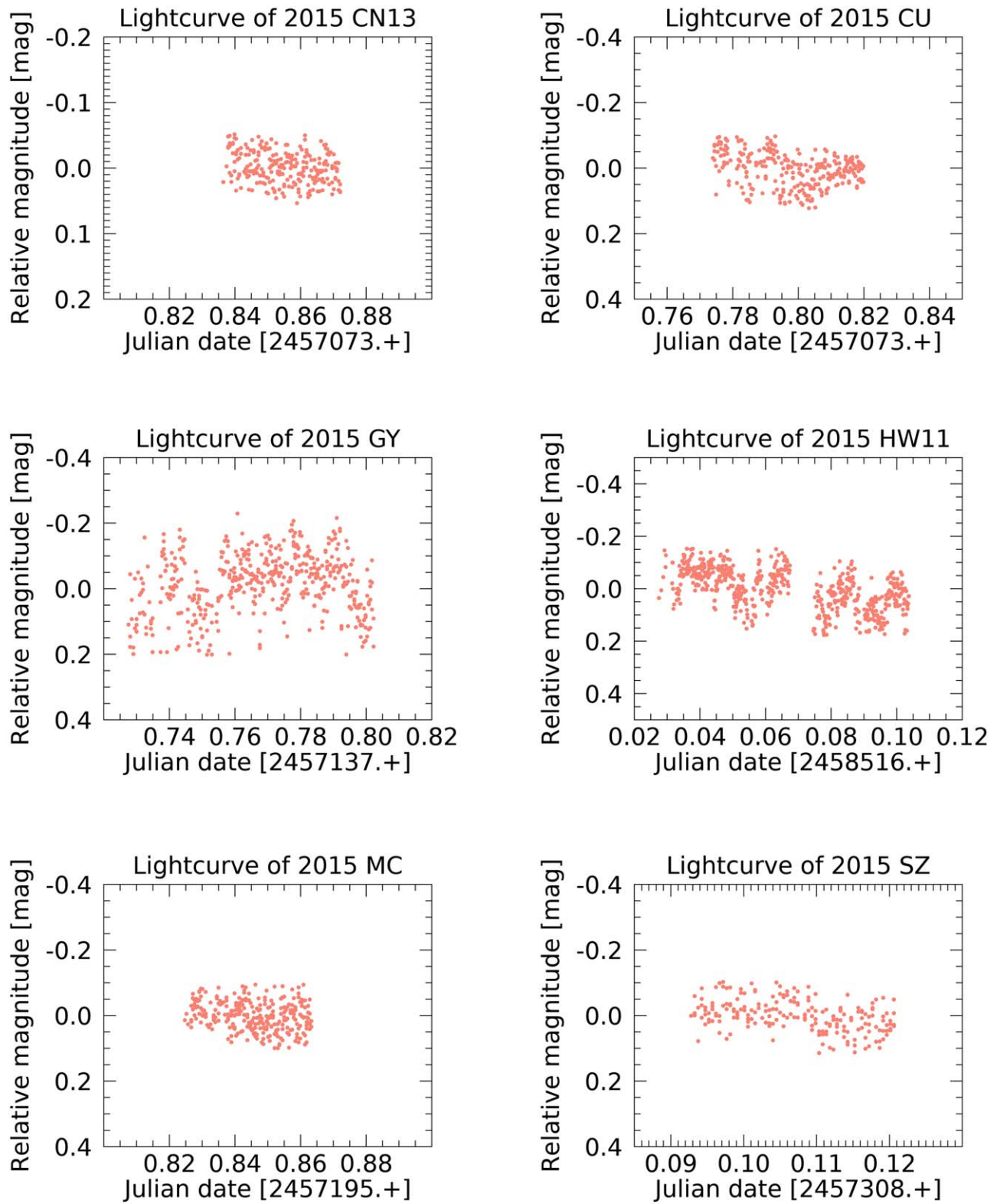**Figure 32.** Full lightcurves of NEOs included in the photometric study. The highest peak of the Lomb periodogram is the single-peaked rotational period with the highest confidence level. The 99.9% confidence level is indicated with a solid line, while the confidence level at 99% is the dotted line, and the dashed line corresponds to a confidence level of 90%. On the right, the lightcurves corresponding to the highest confidence level peak are plotted. The lightcurves have been fitted with a Fourier series fit (black curves).
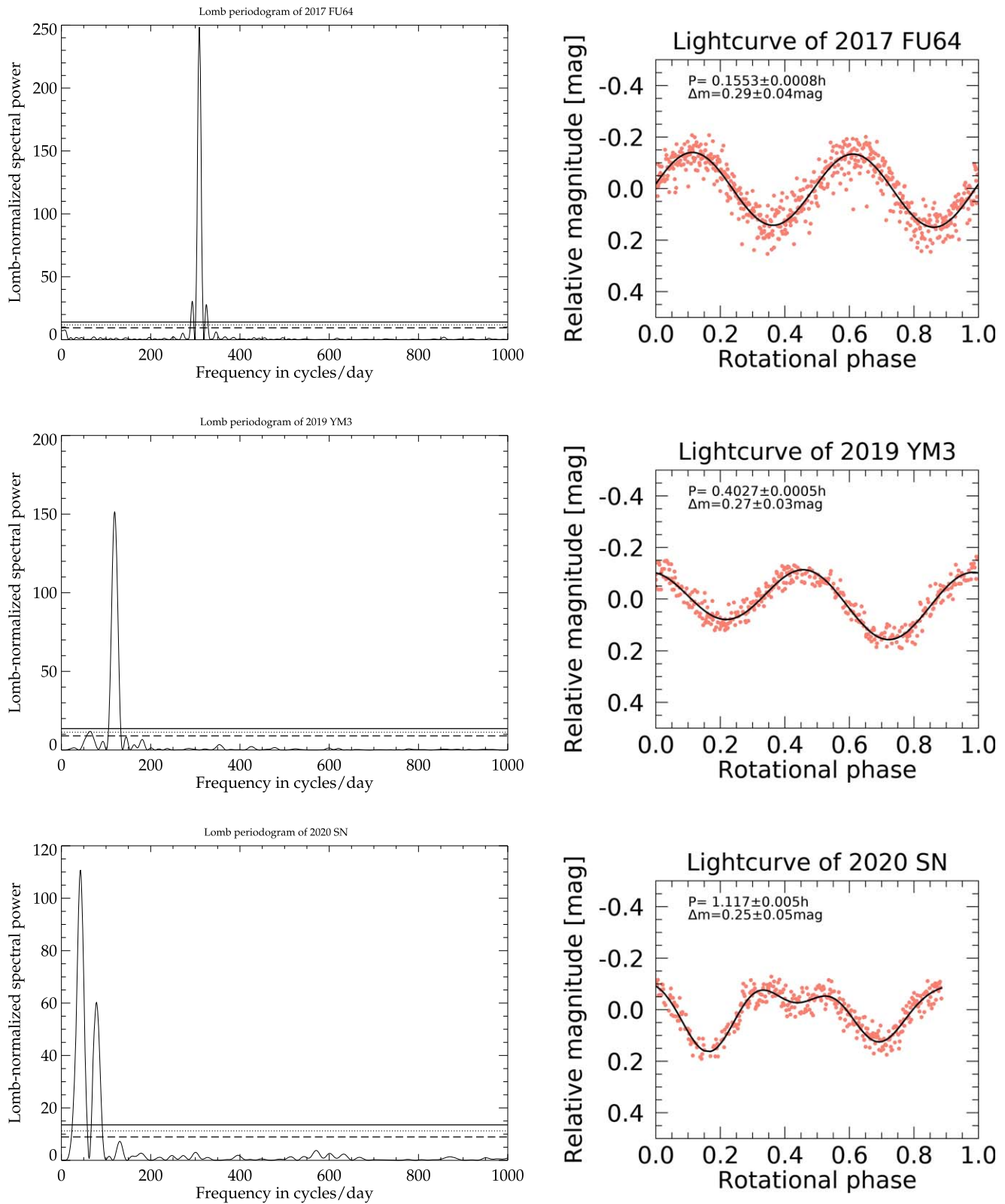
Figure 33. Full lightcurves of NEOs included in the photometric study. The highest peak of the Lomb periodogram is the single-peaked rotational period with the highest confidence level. The 99.9% confidence level is indicated with a solid line, while the confidence level at 99% is the dotted line, and the dashed line corresponds to a confidence level of 90%. On the right, the lightcurves corresponding to the highest confidence level peak are plotted. The lightcurves have been fitted with a Fourier series fit (black curves).
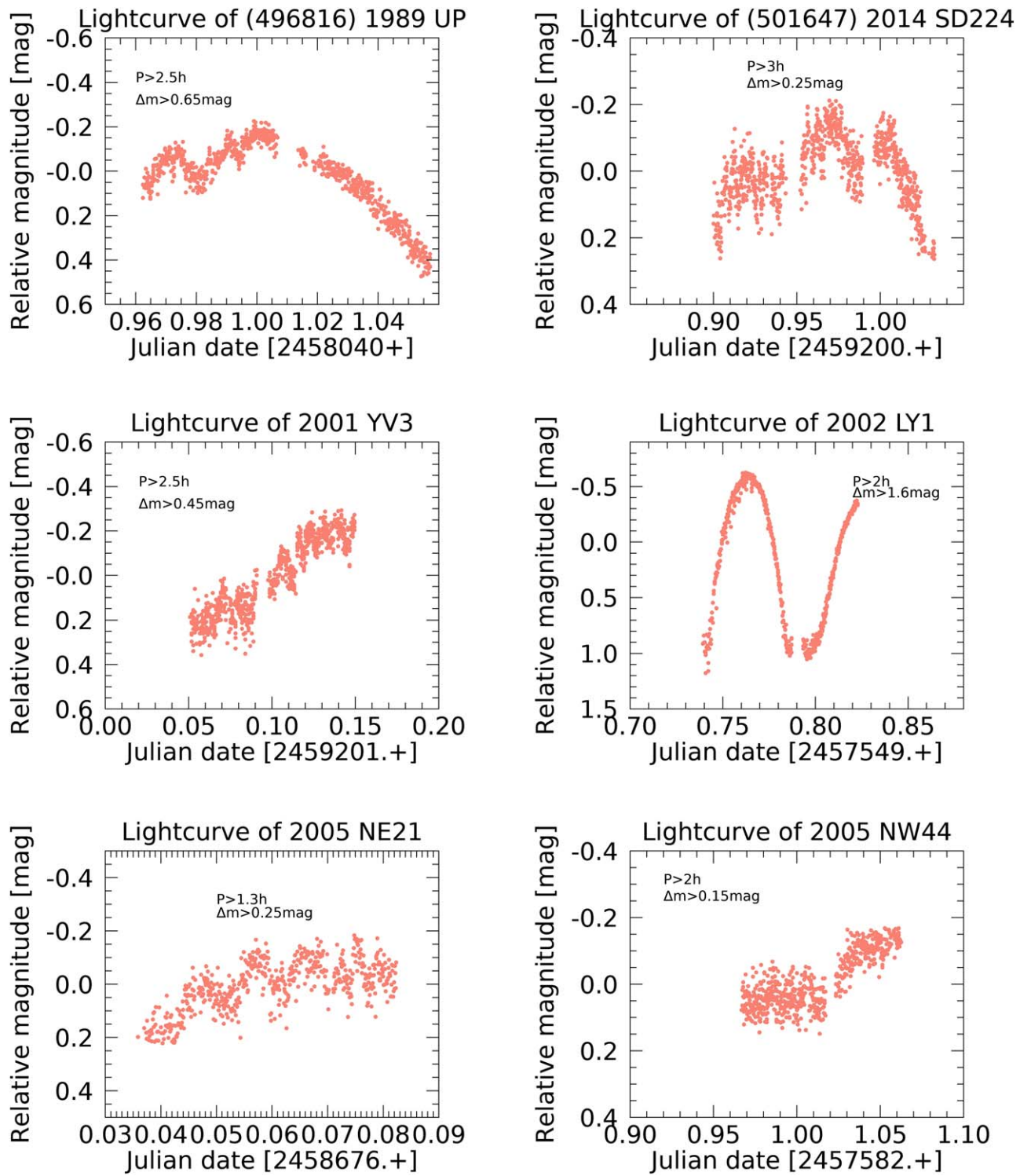
Figure 34. Partial lightcurves of NEOs included in the photometric study.

Figure 35. Partial lightcurves of NEOs included in the photometric study.

Figure 36. Partial lightcurves of NEOs included in the photometric study.

Figure 37. Partial lightcurves of NEOs included in the photometric study.
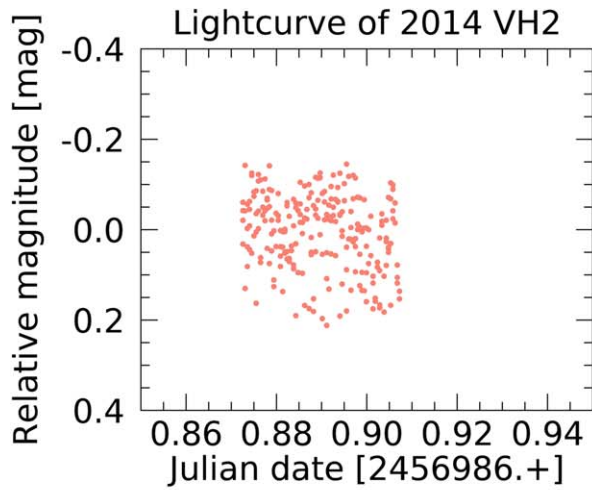
Figure 38. Flat lightcurves of NEOs included in the photometric study.
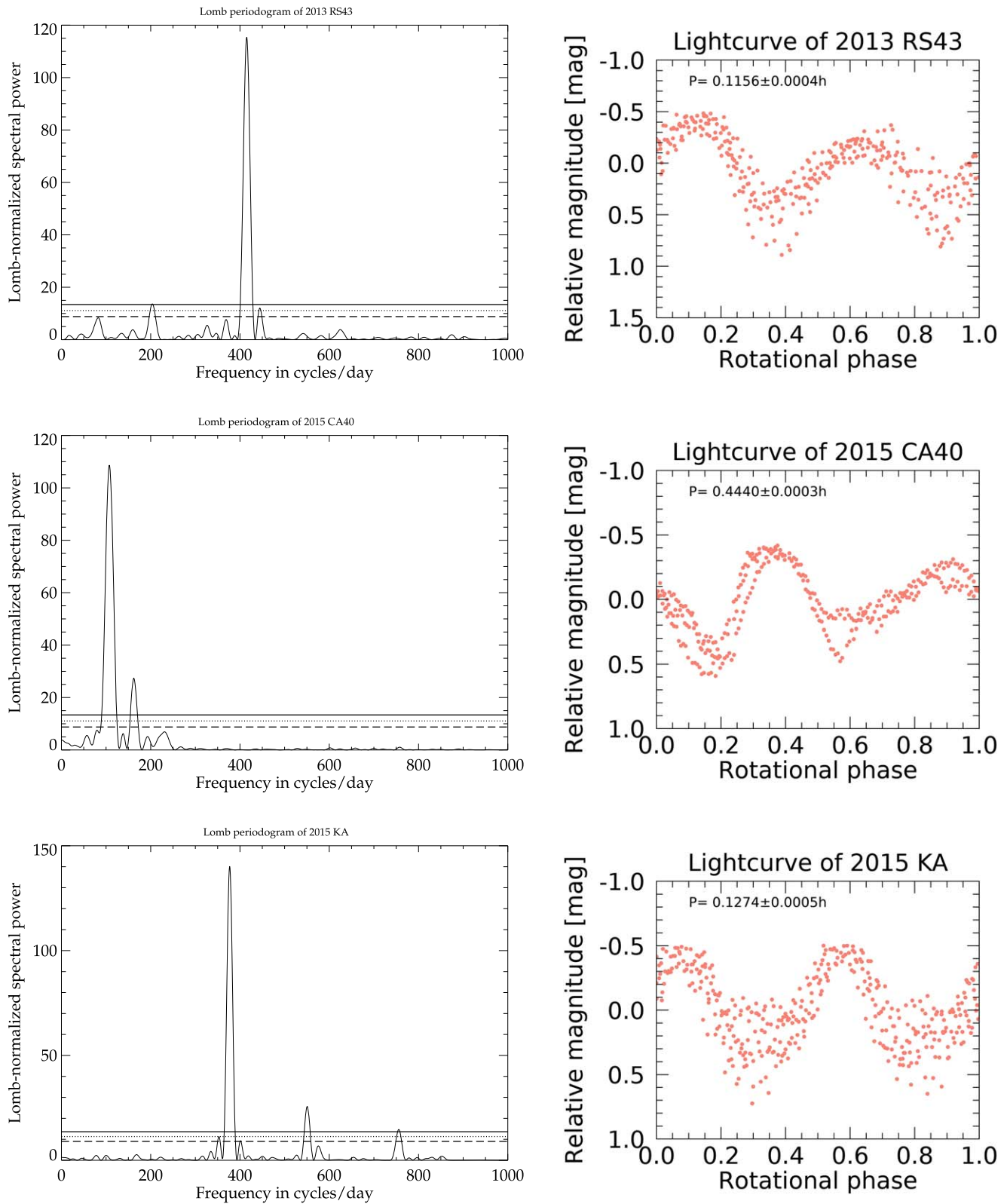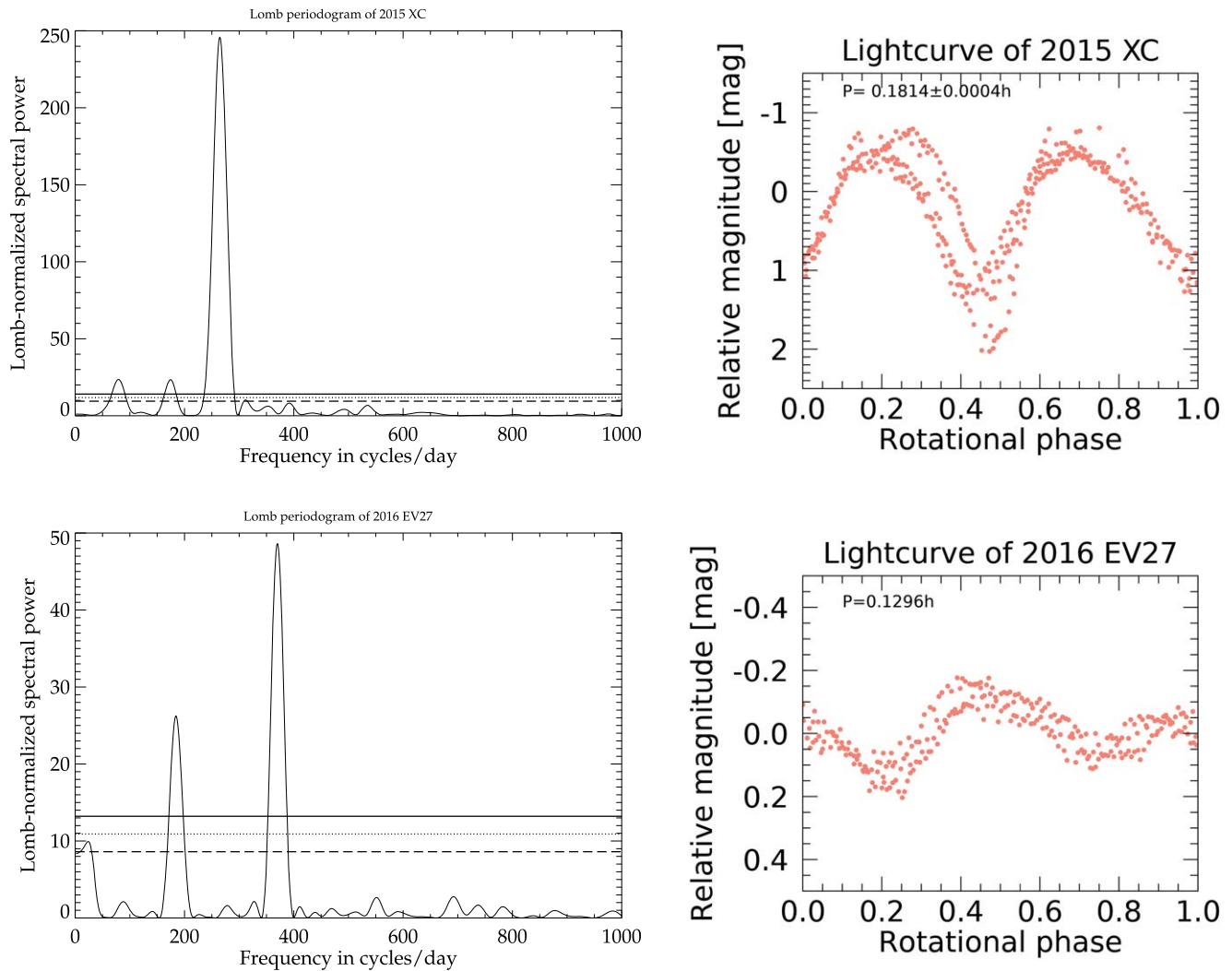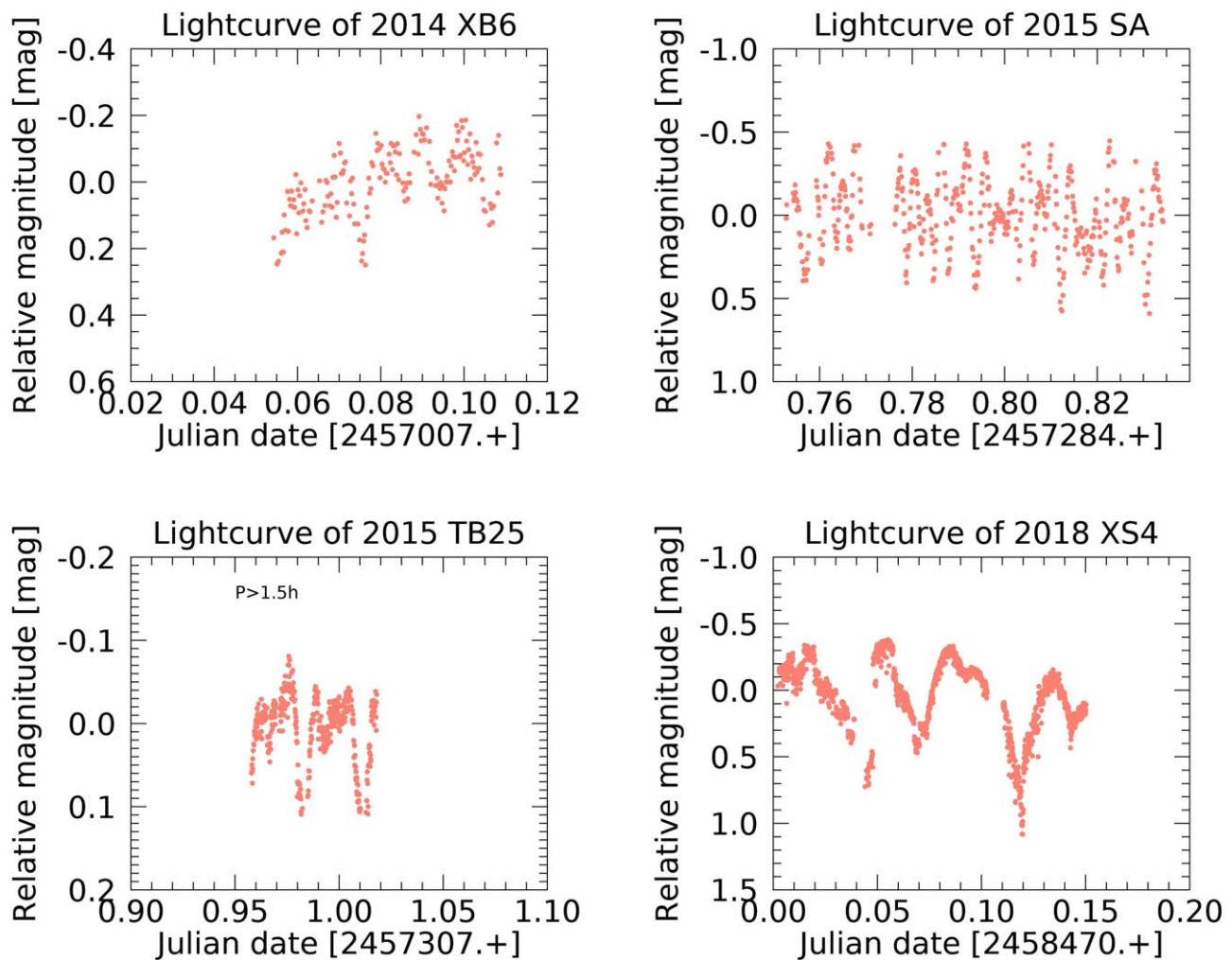
Figure 39. Flat lightcurves of NEOs included in the photometric study.
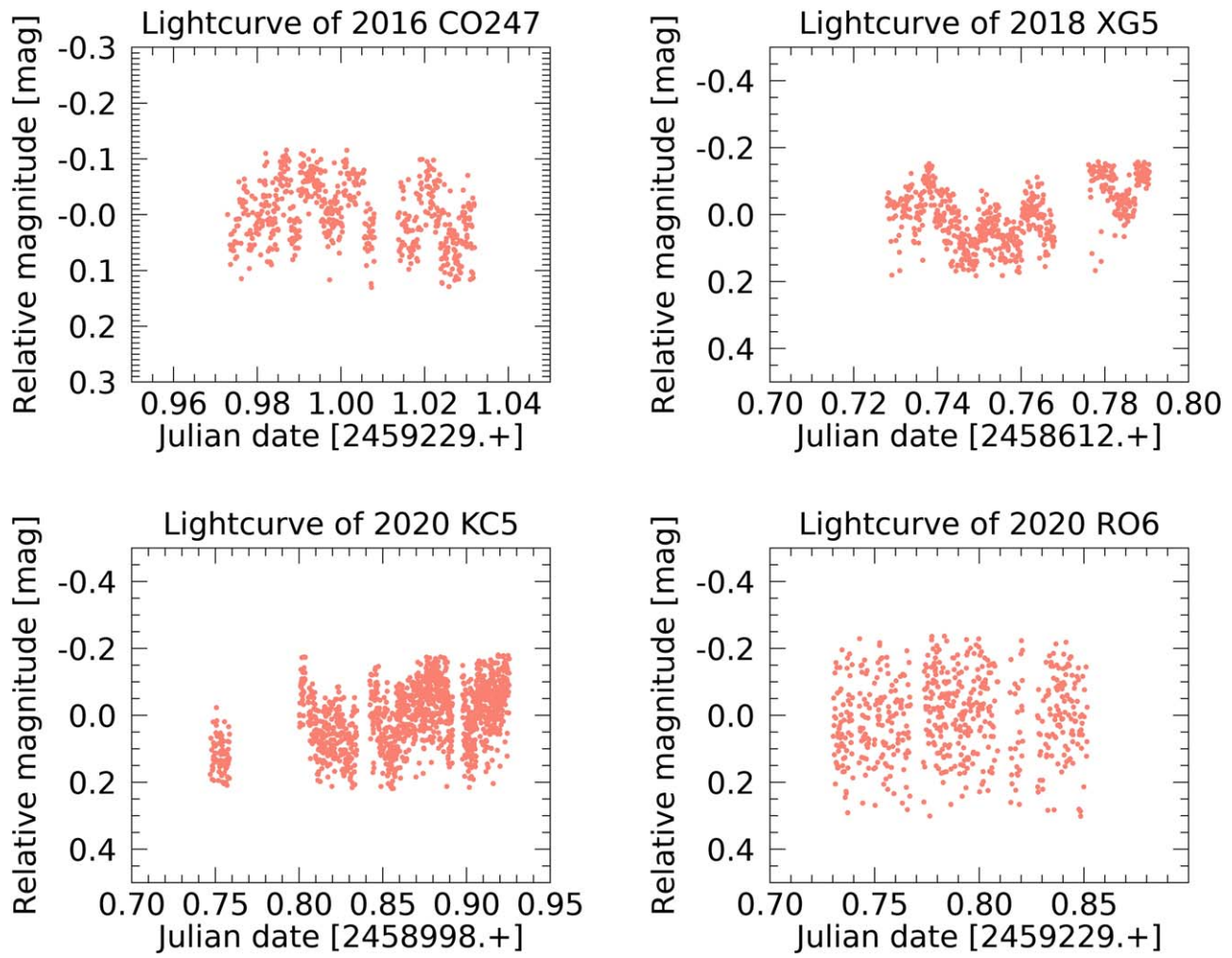
Figure 40. Flat lightcurves of NEOs included in the photometric study.

Figure 41. Tumbler lightcurves of NEOs included in the photometric study.

Figure 42. Tumbler lightcurves of NEOs included in the photometric study.

Figure 43. Tumbler lightcurves of NEOs included in the photometric study.

ORCID iDs

Juan A. Sanchez ⓘ https://orcid.org/0000-0002-0764-4672
Vishnu Reddy ⓘ https://orcid.org/0000-0002-7743-3491
Audrey Thirouin ⓘ https://orcid.org/0000-0002-1506-4248
William F. Bottke ⓘ https://orcid.org/0000-0002-1804-7814
Theodore Kareta ⓘ https://orcid.org/0000-0003-1008-7499
Mario De Florio ⓘ https://orcid.org/0000-0003-2285-3074
Benjamin N. L. Sharkey ⓘ https://orcid.org/0000-0003-1383-1578
Adam Battle ⓘ https://orcid.org/0000-0002-4412-5732
David C. Cantillo ⓘ https://orcid.org/0000-0001-6018-1729
Neil Pearson ⓘ https://orcid.org/0000-0002-0183-1581

References

Abe, M., Takagi, Y., Kitazato, K., et al. 2006, Sci, 312, 1334
Adams, J. B. 1974, JGR, 79, 4829
Agee, C. B., Vaci, Z., Ziegler, K., et al. 2019, LPSC, 50, 1176
Alvarez, L. W., Alvarez, W., Asaro, F., et al. 1980, Sci, 208, 1095
Barucci, M. A., Perna, D., Popescu, M., et al. 2018, MNRAS, 476, 4481
Battle, A., Reddy, V., Sanchez, J. A., et al. 2022, PSJ, 3, 226
Binzel, R. P., DeMeo, F. E., Turtelboom, E. V., et al. 2019, Icar, 324, 41
Binzel, R. P., Morbidelli, A., Merouane, S., et al. 2010, Natur, 463, 331
Binzel, R. P., Rivkin, A. S., Bus, S. J., et al. 2001, M&APS, 36, 1167
Bishop, C. M. 2006, Pattern Recognition and Machine Learning (New York: Springer), 209
Bowen, B., Reddy, V., De Florio, M., et al. 2023, PSJ, 4, 52

Burbine, T. H., Binzel, R. P., Bus, S. J., et al. 2001, M&APS, 36, 245
Burbine, T. H., Buchanan, P. C., Dolkar, T., & Binzel, R. P. 2009, M&PS, 44, 1331
Burbine, T. H., Gaffey, M. J., & Bell, J. F. 1992, Metic, 27, 424
Burns, R. G. 1993, in Mineralogical Applications of Crystal Field Theory, ed. R. G. Burns (Cambridge: Cambridge Univ. Press)
Cantillo, D. C., Reddy, V., Battle, A., et al. 2023, PSJ, 4, 177
Carbognani, A., Bacci, P., & Buzzi, L. 2018, MPBu, 45, 6
Carbognani, A., & Buzzi, L. 2016, MPBu, 43, 160
Chyba, C. F., Thomas, P. J., & Zahnle, K. J. 1993, Natur, 361, 40
Clark, B. E., Hapke, B., Pieters, C., et al. 2002, in Asteroids III, ed. W. F. Bottke, Jr. et al. (Tucson, AZ: Univ. Arizona Press), 585
Cloutis, E. A., Gaffey, M. J., Jackowski, T. L., & Reed, K. L. 1986, JGR, 91, 11641
Cloutis, E. A., Hudon, P., Hiroi, T., et al. 2011, Icar, 216, 309
Cloutis, E. A., Hudon, P., Hiroi, T., et al. 2012, Icar, 220, 586
Consolmagno, G. J., & Drake, M. J. 1977, GeCoA, 41, 1271
Cushing, M. C., Vacca, W. D., & Rayner, J. T. 2004, PASP, 116, 362
de León, J., Licandro, J., Serra-Ricart, M., et al. 2010, A&A, 517, A23
de León, J., Pinilla-Alonso, N., Campins, H., et al. 2012, Icar, 218, 196
Delbo, M., Libourel, G., Wilkerson, J., et al. 2014, Natur, 508, 233
DeMeo, F. E., Binzel, R. P., Slivan, S. M., et al. 2009, Icar, 202, 160
DeMeo, F. E., Burt, B. J., Marsset, M., et al. 2022, Icar, 380, 114971
Devogèle, M., Moskovitz, N., Thirouin, A., et al. 2019, AJ, 158, 196
Devogèle, M., Tanga, P., Cellino, A., et al. 2018, Icar, 304, 31
Doressoundiram, A., Barucci, M. A., Fulchignoni, M., et al. 1998, Icar, 131, 15
Dressler, B. O., Grieve, R. A. F., & Sharpton, V. L. 1994, Large Meteorite Impacts and Planetary Evolution (Boulder, CO: GSA), 1994
Dunn, T. L., Burbine, T. H., Bottke, W. F., et al. 2013, Icar, 222, 273
Dunn, T. L., McCoy, T. J., Sunshine, J. M., et al. 2010, Icar, 208, 789
Erasmus, N., Mommert, M., Trilling, D. E., et al. 2017, AJ, 154, 162

Fowler, J. W., & Chillemi, J. R. 1992, The IRAS Minor Planet Survey PL-TR-92-2049, Phillips Laboratory, Hanscom Air Force Base, MA
Gaffey, M. J. 2010, Icar, 209, 564
Gaffey, M. J., Burbine, T. H., Piatek, J. L., et al. 1993, Icar, 106, 573
Gartrelle, G. M., Hardersen, P. S., Izawa, M. R. M., et al. 2021, Icar, 361, 114349
Godunova, V., Reshetnyk, V., & Andreev, M. 2016, MPBu, 43, 156
Granvik, M., Morbidelli, A., Jedicke, R., et al. 2018, Icar, 312, 181
Granvik, M., Morbidelli, A., Vokrouhlický, D., et al. 2017, A&A, 598, A52
Graves, K. J., Minton, D. A., Hirabayashi, M., et al. 2018, Icar, 304, 162
Gutiérrez, P. J., Davidsson, B. J. R., Ortiz, J. L., et al. 2006, A&A, 454, 367
Hapke, B. 2001, JGR, 106, 10039
Hardersen, P. S., Cloutis, E. A., Reddy, V., et al. 2011, M&PS, 46, 1910
Hasegawa, S., Hiroi, T., Ohtsuka, K., et al. 2019, PASJ, 71, 103
Hasegawa, S., Kuroda, D., Kitazato, K., et al. 2018, PASJ, 70, 114
Hildebrand, A. R., Penfield, G. T., Kring, D. A., et al. 1991, Geo, 19, 867
Hiroi, T., Zolensky, M. E., & Pieters, C. M. 2001, Sci, 293, 2234
Hromakina, T., Birlan, M., Barucci, M. A., et al. 2023, MNRAS, 520, 3143
Jansen, C. A., Brenker, F. E., Zipfel, J., et al. 2019, ChEG, 79, 125537
Jenniskens, P., Popova, O. P., Glazachev, D. O., et al. 2019, Icar, 327, 4
Kareta, T., Reddy, V., Sanchez, J. A., et al. 2022, PSJ, 3, 105
Kohout, T., Gritsevich, M., Grokhovsky, V. I., et al. 2014, Icar, 228, 78
Kohout, T., Petrova, E. V., Yakovlev, G. A., et al. 2020, A&A, 639, A146
Le Corre, L., Sanchez, J. A., Reddy, V., et al. 2023, PSJ, 4, 91
Lebofsky, L. A., & Spencer, J. R. 1989, Asteroids II (Tucson, AZ: Univ. Arizona Press), 128
Lomb, N. R. 1976, Ap&SS, 39, 447
Lucas, M. P., Emery, J. P., Hiroi, T., et al. 2019, M&PS, 54, 157
Marsset, M., DeMeo, F. E., Burt, B., et al. 2022, AJ, 163, 165
McCord, T. B., Adams, J. B., & Johnson, T. V. 1970, Sci, 168, 1445
Mittlefehldt, D. W. 2015, ChEG, 75, 155
Mittlefehldt, D. W., McCoy, T. J., Goodrich, C. A., et al. 1998, in Planetary Materials, Vol. 36, ed. J. J. Papike (Chantilly, VA: Mineralogical Society of America) 4–001
Monteiro, F., Silva, J. S., Lazzaro, D., et al. 2018, P&SS, 164, 54
Moskovitz, N. A., Willman, M., Burbine, T. H., et al. 2010, Icar, 208, 773
Mothé-Diniz, T., Carvano, J. M., Bus, S. J., et al. 2008, Icar, 195, 277
Nakamura, T., Noguchi, T., Tanaka, M., et al. 2011, Sci, 333, 1113
Neeley, J. R., Clark, B. E., Ockert-Bell, M. E., et al. 2014, Icar, 238, 37
Nesvorný, D., Bottke, W. F., Vokrouhlický, D., et al. 2010, Icar, 209, 510
Ockert-Bell, M. E., Clark, B. E., Shepard, M. K., et al. 2010, Icar, 210, 674
Ostro, S. J., Campbell, D. B., Chandler, J. F., et al. 1991, NASA, Washington, Reports of Planetary Astronomy, 1991 SEE N92-12792 03-89, 174
Pieters, C. M. 1983, JGR, 88, 9534
Pieters, C. M., Taylor, L. A., Noble, S. K., et al. 2000, M&APS, 35, 1101
Polishook, D., DeMeo, F. E., Burt, B. J., et al. 2023, PSJ, 4, 229
Popescu, M., Birlan, M., & Nedelcu, D. A. 2012, A&A, 544, A130

Pravec, P., & Harris, A. W. 2000, Icar, 148, 12
Pravec, P., & Harris, A. W. 2007, Icar, 190, 250
Rayner, J. T., Toomey, D. W., Onaka, P. M., et al. 2003, PASP, 115, 362
Reddy, V., Emery, J. P., Gaffey, M. J., et al. 2009, M&APS, 44, 1917
Reddy, V., Gaffey, M. J., Abell, P. A., et al. 2012a, Icar, 219, 382
Reddy, V., Pearson, N., Agee, C. B., et al. 2019, LPSC, 50, 2212
Reddy, V., Sanchez, J. A., Bottke, W. F., et al. 2014, Icar, 237, 116
Reddy, V., Sanchez, J. A., Bottke, W. F., et al. 2016, AJ, 152, 162
Reddy, V., Sanchez, J. A., Nathues, A., et al. 2012b, Icar, 217, 153
Sanchez, J. A., Michelsen, R., Reddy, V., & Nathues, A. 2013, Icar, 225, 131
Sanchez, J. A., Reddy, V., Bottke, W. F., et al. 2021, PSJ, 2, 205
Sanchez, J. A., Reddy, V., Nathues, A., et al. 2012, Icar, 220, 36
Sanchez, J. A., Reddy, V., Shepard, M. K., et al. 2017, AJ, 153, 29
Sanchez, J. A., Thomas, C., Reddy, V., et al. 2020, AJ, 159, 146
Shepard, M. K., Clark, B. E., Ockert-Bell, M., et al. 2010, Icar, 208, 221
Shepard, M. K., Taylor, P. A., Nolan, M. C., et al. 2015, Icar, 245, 38
Steuber, T., Mitchell, S. F., Buhl, D., et al. 2002, Geo, 30, 999
Sunshine, J. M., Connolly, H. C., McCoy, T. J., et al. 2008, Sci, 320, 514
Tan, H., Yeh, T., Li, B., et al. 2018, MPBu, 45, 57
Thirouin, A. 2013, PhD thesis, Univ. Granada
Thirouin, A., Moskovitz, N., Binzel, R. P., et al. 2016, AJ, 152, 163
Thirouin, A., Moskovitz, N. A., Binzel, R. P., et al. 2018, ApJS, 239, 4
Thomas, C. A., Emery, J. P., Trilling, D. E., et al. 2014, Icar, 228, 217
Thomas, C. A., Trilling, D. E., Emery, J. P., et al. 2011, AJ, 142, 85
Vaduvescu, O., Macias, A. A., Tudor, V., et al. 2017, EM&P, 120, 41
Vernazza, P., Binzel, R. P., Thomas, C. A., et al. 2008, Natur, 454, 858
Vernazza, P., Brunetto, R., Binzel, R. P., et al. 2009, Icar, 202, 477
Virkki, A. K., Marshall, S. E., Venditti, F. C. F., et al. 2022, PSJ, 3, 222
Warner, B. D. 2015, MPBu, 42, 115
Warner, B. D. 2016a, MPBu, 43, 311
Warner, B. D. 2016b, MPBu, 43, 143
Warner, B. D. 2016c, MPBu, 43, 240
Warner, B. D. 2017, MPBu, 44, 22
Warner, B. D. 2018, MPBu, 45, 366
Warner, B. D., Harris, A. W., & Pravec, P. 2009, Icar, 202, 134
Warner, B. D., & Oey, J. 2015, MPBu, 42, 196
Warner, B. D., & Stephens, R. D. 2019, MPBu, 46, 423
Warner, B. D., & Stephens, R. D. 2020, MPBu, 47, 290
Warner, B. D., & Stephens, R. D. 2021a, MPBu, 48, 30
Warner, B. D., & Stephens, R. D. 2021b, MPBu, 48, 170
Warner, B. D., & Stephens, R. D. 2021c, MPBu, 48, 294
Weisberg, M. K., McCoy, T. J., & Krot, A. N. 2006, in Meteorites and the Early Solar System II, ed. D. S. Lauretta & H. Y. McSween, Jr. (Tucson, AZ: Univ. Arizona Press), 19
Wisniewski, W. Z., Michałowski, T. M., Harris, A. W., et al. 1997, Icar, 126, 395
Zappala, V., Cellino, A., Barucci, A. M., et al. 1990, A&A, 231, 548